



저작자표시-비영리-변경금지 2.0 대한민국

이용자는 아래의 조건을 따르는 경우에 한하여 자유롭게

- 이 저작물을 복제, 배포, 전송, 전시, 공연 및 방송할 수 있습니다.

다음과 같은 조건을 따라야 합니다:



저작자표시. 귀하는 원저작자를 표시하여야 합니다.



비영리. 귀하는 이 저작물을 영리 목적으로 이용할 수 없습니다.



변경금지. 귀하는 이 저작물을 개작, 변형 또는 가공할 수 없습니다.

- 귀하는, 이 저작물의 재이용이나 배포의 경우, 이 저작물에 적용된 이용허락조건을 명확하게 나타내어야 합니다.
- 저작권자로부터 별도의 허가를 받으면 이러한 조건들은 적용되지 않습니다.

저작권법에 따른 이용자의 권리는 위의 내용에 의하여 영향을 받지 않습니다.

이것은 [이용허락규약\(Legal Code\)](#)을 이해하기 쉽게 요약한 것입니다.

[Disclaimer](#)

工學博士學位論文

**Performance Enhancement of
Zeolitic Imidazolate Framework Derivatives/
Carbon Structures-Based Supercapacitors**

제올라이트형 이미다졸레이트 골격 유도체/
탄소 구조체 기반 슈퍼커패시터의 성능 향상

2019年 8月

서울대학교 大學院

化學生物工學部

李京燮

**Performance Enhancement of
Zeolitic Imidazolate Framework Derivatives/
Carbon Structures-Based Supercapacitors**

by

Gyeongseop Lee

Submitted to the Graduate School of Seoul National
University in Partial Fulfillment of the Requirements for
the Degree of Doctor of Philosophy

August, 2019

Thesis Adviser: Jyongsik Jang

Abstract

Supercapacitors (SCs) are one of the most promising energy systems in the modern industry together with fuel cells and batteries. Owing to their attractive properties such as high power density and long lifespan, SCs have been utilized in many fields that require fast storage and retrieval of energy. However, the relatively low energy density of SCs compared to other energy systems limits their comprehensive use across a range of industrial fields. Thus, for manufacturing SCs with enhanced energy density while maintaining their beneficial properties, recent research interests on SCs have focused on developing novel electrode materials that are all superior in terms of charge storage ability, rate capability, and cycle stability. To achieve above purpose, the applied material should be selected and combined appropriately, considering the pros and cons of each type of SC electrode material (*i.e.*, electric double layer capacitor, pseudocapacitor, battery-type material). In addition to the intrinsic characteristics of the electrode materials, rational design of their structure to facilitate interaction between them and the surrounding electrolyte is another important consideration for obtaining high-performance SC electrode materials.

Zeolitic imidazolate frameworks (ZIFs), the sub-family of metal-

organic frameworks (MOFs), are the crystalline porous materials with large surface area, which are constructed by the arrangement of certain metal ions and imidazolate ligands. Interestingly, in recent years, there have been increasing attempts to employ ZIF as the precursor material for synthesizing high-performance SC electrode materials. By applying suitable heat treatment or chemical reaction, ZIFs can be transformed into various electroactive materials including carbons, metal oxides, and metal hydroxides. Besides, the electroactive materials with unique architectures such as the porous/hollow structures can be easily acquired by using the ZIF precursors. Therefore, the diversity in the structure and chemical composition of the ZIF derivatives can be useful in the design of next-generation SC electrode materials.

This dissertation describes the preparation method of diverse ZIF derivatives/carbon structures and their application for SC electrode materials. The effective strategies for designing beneficial structures for charge storage using ZIF derivatives and carbon architectures have been discussed. Firstly, a hybrid structure composed of ZnO quantum dots (QDs) in porous carbon (ZnO QDs@carbon) and carbon nanofiber (CNF) was fabricated *via* carbonization of electrospun ZIF-8/PVA

nanofibers. This architecture possessed the one-dimensional conductive path on the main axis and the hierarchical porous structure/pseudocapacitive ZnO QDs on the surface. Secondly, a hybrid structure of homogeneously distributed Co_3O_4 nanograins on the $\text{Co}(\text{OH})_2$ plate was produced by the hydrothermal reaction of ZIF-67. In this architecture, the $\text{Co}(\text{OH})_2$ sheet served as the effective supporting backbone for numerous Co_3O_4 nanograins, resulting in alleviation of agglomeration between the active materials. Finally, the composite of ZIF-67s and hollow carbon sphere (HCS) is utilized as the precursor to synthesize a hybrid structure of hollow Ni-Co LDH and HCS. This architecture showed the distinctive hollow-in-hollow structure. Due to their rationally designed structures, the prepared ZIF derivatives/carbon architectures demonstrated decent electrochemical performances. Accordingly, this study provides the synthetic approach to high-performance SC electrode materials, especially the structural design.

Keywords: Supercapacitor, Metal-organic framework, Zeolitic imidazolate framework, Carbon material, Hybrid structure.

Student Number: 2014-22597

List of Abbreviations

1D: one-dimensional

AC: activated carbon

AFM: atomic force microscopy

Ar: argon

At%: atomic percent

Au: gold

BET: Brunauer–Emmett–Teller

BJH: Barrett–Joyner–Halenda

ca.: circa

cm: centimeter

CNF: carbon nanofiber

CNG/Co(OH)₂: cobalt oxide nanograins-decorated cobalt hydroxide
sheet

CNT: carbon nanotube

Co₃O₄: cobalt oxide

Co(NO₃)₂·6H₂O: cobalt nitrate hexahydrate

Co(OH)₂: cobalt hydroxide

C_{sc}: specific capacity

C_{sp} : specific capacitance

CTAB: hexadecyltrimethylammonium bromide

CV: cyclic voltammetry

DA: dopamine

DI: deionized

DMF: dimethylformamide

E : energy density

EDLC: electric double layer capacitor

EDX: energy dispersive X-ray spectroscopy

e.g.: *exempli gratia*

EIS: electrochemical impedance spectroscopy

F: faraday

g: gram

GCD: galvanostatic charge/discharge

GO: graphene oxide

h: hour

HCS: hollow carbon sphere

HCS@ZIF-67: hybrid structure of homogeneously distributed ZIF-67s
on HCS shell

HIH-LDH: hybrid structure of homogeneously distributed ZIF-67-

derived hollow Ni-Co LDHs on HCS shell

H-LDH: ZIF-67-derived hollow Ni-Co LDH

Hmim: 2-methylimidazole

HR-TEM: high-resolution transmission electron microscopy

HSC: hybrid supercapacitor

i.e.: id est

K: kelvin

kHz: kilohertz

km: kilometer

KOH: potassium hydroxide

kV: kilovolt

LDH: layered double hydroxide

M: mole

mAh: milliampere-hour

mg: milligram

mHz: millihertz

min: minute

ml: milliliter

MOF: metal-organic framework

MPRGO: mesoporous plasma-reduced graphene oxide

mV: millivolt

MW: molecular weight

N₂: nitrogen

Na₂SO₄: sodium sulfate

NaOH: sodium hydroxide

Ni(NO₃)₂·6H₂O: nickel nitrate hexahydrate

NMP: N-methyl-2-pyrrolidone

P: power density

PAN: polyacrylonitrile

PCNF: PVA-based carbon nanofiber

PDA: polydopamine

PEN: polyethylene naphthalate

pH: potential of hydrogen

Pt: platinum

PVA: poly(vinyl alcohol)

PVDF: polyvinylidene fluoride

QD: quantum dot

*R*_{ct}: charge transfer resistance

*R*_s: equivalent series resistance

s: second

SAED: selected-area electron diffraction

SC: supercapacitor

sccm: standard cubic centimeter per minute

SEM: scanning electron microscopy

SiO₂: silicon dioxide

STEM: scanning transmission electron microscopy

TEM: transmission electron microscopy

TEOS: tetraethyl orthosilicate

TGA: thermogravimetric analysis

V: volt

W: watt

Wh: watt-hour

wt%: weight percent

XPS: X-ray photoelectron spectroscopy

ZIF: zeolitic imidazolate framework

ZIF-8-C: carbonized ZIF-8 nanocrystal

ZIF-8/PAN-C: carbonized ZIF-8/PAN nanofiber

Zn(NO₃)₂·6H₂O: zinc nitrate hexahydrate

ZnO: zinc oxide

ZnO QDs@carbon: ZnO QDs embedded in porous carbon

ZPCNF: ZnO QDs-decorated carbon nanofiber

θ : theta

μg : microgram

μm : micrometer

List of Figures

- Figure 1.** (a, b) Trolley bus and Electric tramcar which use the SC as a power source. (c) Ragone plot showing the power density vs. energy density of various energy systems.
- Figure 2.** Classification of SC electrode materials according to charge storage mechanisms (EDLC, pseudocapacitor, and battery-type materials).
- Figure 3.** (a) Schematic illustration of the synthesis of HCS using SiO_2 sphere as the hard template and PDA as the carbon source. (b) Microscopy images of HCSs obtained using various TEM techniques.
- Figure 4.** Schematic illustration of the basic setup for electrospinning process. The inset shows a typical SEM image of electrospun poly(vinyl pyrrolidone) (PVP) nanofibers.
- Figure 5.** Schematic diagram of typical HSC device structure.
- Figure 6.** (a) Schematic diagram illustrating the formation of MOF. (b) Various application fields of MOFs.
- Figure 7.** An overview of the transformation strategies from MOF-based templates to MOF derivatives.

Figure 8. Co_3O_4 dodecahedron and (b) hollow Mg-Co LDH architectures synthesized using MOF templates.

Figure 9. Synthesis procedure and crystal structure of ZIF-8 and ZIF-67.

Figure 10. Schematic illustration of the ZPCNF preparation process.

Figure 11. (a) SEM image, (b) TEM image, and (c) XRD pattern of the synthesized ZIF-8 nanocrystals.

Figure 12. (a, b) SEM images, (c, d) TEM images, (e) HR-TEM image, and (f) STEM image with the corresponding elemental mapping of ZPCNF-4. The inset in (c) is the SAED pattern of ZPCNF-4.

Figure 13. (a) SEM image and (b) TEM image of PCNF.

Figure 14. (a) SEM image and (b, c) TEM images of ZPCNF-2.

Figure 15. XPS results of ZPCNF-4: (a) survey scan and high-resolution patterns of (b) Zn 2p and (c) C 1s.

Figure 16. (a) XRD spectra of PCNF, ZIF-8/PVA fiber, ZPCNF-4. (b) XRD spectra of ZIF-8/PAN fiber and ZIF-8/PAN-C. (c) XRD spectra of ZIF-8-C.

Figure 17. SEM images of (a) ZIF-8/PAN-C and (b) ZIF-8-C; (c, d) TEM images of ZIF-8/PAN-C.

- Figure 18.** Raman spectrum of ZPCNF-4.
- Figure 19.** TGA thermogram of ZPCNF-4 at air atmosphere.
- Figure 20.** (a) Nitrogen adsorption/desorption plots and (b) pore-size distribution curves of PCNF, ZIF-8-C, and ZPCNF-4.
- Figure 21.** Electrical conductivities of ZIF-8-C, PCNF, and ZPCNF-4.
- Figure 22.** (a) CV curves of PCNF, ZPCNF-2, and ZPCNF-4 at the scan rate of 10 mV s^{-1} . (b) CV curves of ZPCNF-4 with different scan rates.
- Figure 23.** GCD curves of (a) PCNF, (b) ZPCNF-2, and (c) ZPCNF-4 with different current densities.
- Figure 24.** Specific capacitance of PCNF, ZPCNF-2, and ZPCNF-4 as a function of current density.
- Figure 25.** Nyquist plots of PCNF, ZPCNF-2, and ZPCNF-4. The inset shows the equivalent circuit diagram.
- Figure 26.** Cycling performance of ZPCNF-4 measured at 1 A g^{-1} for 5000 cycles.
- Figure 27.** Shear viscosity as a function of the shear rate for electrospinning solutions containing different amounts of ZIF-8. The inset shows the magnified data in the high shear rate range.

Figure 28. Schematic illustration of the synthesis procedure for size-controllable CNG/Co(OH)₂ using various-sized ZIF-67 as the precursor material.

Figure 29. XRD patterns before and after the hydrothermal reaction of (a) S_ZIF-67, (b) M_ZIF-67, and (c) L_ZIF-67.

Figure 30. SEM images of (a) S_ZIF-67, (b) S_CNG/Co(OH)₂, (c) M_ZIF-67, (d) M_CNG/Co(OH)₂, (e) L_ZIF-67, and (f) L_CNG/Co(OH)₂.

Figure 31. SEM images of (a) pure Co₃O₄ and (b) pure Co(OH)₂.

Figure 32. TEM image of CNG/Co(OH)₂ architecture obtained using 200 nm-sized ZIF-67 as the precursor material.

Figure 33. (a, b) TEM images, (c) AFM image (inset: height profile result), (d) HR-TEM image, (e) SAED pattern, and (f) STEM image with the corresponding elemental mapping (C, Co, and O) of L_CNG/Co(OH)₂.

Figure 34. EDX spectra of (a) S_ZIF-67, (b) M_ZIF-67, and (c) L_ZIF-67.

Figure 35. EDX spectra of (a) S_CNG/Co(OH)₂, (b) M_CNG/Co(OH)₂, and (c) L_CNG/Co(OH)₂.

Figure 36. Co 2p XPS spectra of (a) S_CNG/Co(OH)₂, (b)

M_CNG/Co(OH)₂, and (c) L_CNG/Co(OH)₂.

Figure 37. TGA curves of S_, M_, and L_CNG/Co(OH)₂ structures.

Figure 38. Nitrogen adsorption/desorption plots and (b) pore-size distribution curves of various-sized CNG/Co(OH)₂ architectures.

Figure 39. CV curves of (a) S_CNG/Co(OH)₂, (b) M_CNG/Co(OH)₂, and (c) L_CNG/Co(OH)₂ with different scan rates.

Figure 40. CV curves of S_, M_, and L_CNG/Co(OH)₂ at the scan rate of 10 mV s⁻¹.

Figure 41. GCD curves of (a) S_CNG/Co(OH)₂, (b) M_CNG/Co(OH)₂, and (c) L_CNG/Co(OH)₂ with different current densities.

Figure 42. Specific capacity of S_, M_, and L_CNG/Co(OH)₂ as a function of current density.

Figure 43. GCD curves of (a) pure Co₃O₄ and (b) pure Co(OH)₂; (c) specific capacity of pure Co₃O₄ and Co(OH)₂ as a function of current density.

Figure 44. Nyquist plots of S_, M_, and L_CNG/Co(OH)₂ in the frequency range from 10 mHz to 100 kHz. The inset shows the high-frequency region of the plots.

Figure 45. Cycling performances of S_, M_, and L_CNG/Co(OH)₂

measured at 4 A g^{-1} for 5000 cycles.

Figure 46. (a, b) SEM images and (c) TEM image of MPRGO.

Figure 47. (a) Nitrogen adsorption/desorption plot and (b) pore-size distribution curve of MPRGO.

Figure 48. Electrochemical results of MPRGO: (a) CV curves with different scan rates. (b) GCD curves at different current densities. (c) Specific capacitance as a function of current density.

Figure 49. Schematic illustration of CNG/Co(OH)₂-based HSC devices.

Figure 50. CV curves of as-prepared HSCs under various voltage windows, which were measured at 50 mV s^{-1} : (a) S_CNG/Co(OH)₂//MPRGO. (b) M_CNG/Co(OH)₂//MPRGO. (c) L_CNG/Co(OH)₂//MPRGO.

Figure 51. CV curves of (a) S_CNG/Co(OH)₂//MPRGO, (b) M_CNG/Co(OH)₂//MPRGO, and (c) L_CNG/Co(OH)₂//MPRGO with different scan rates.

Figure 52. GCD curves of (a) S_CNG/Co(OH)₂//MPRGO, (b) M_CNG/Co(OH)₂//MPRGO, and (c) L_CNG/Co(OH)₂//MPRGO with different current densities.

Figure 53. Specific capacity of S₋, M₋, and L_CNG/Co(OH)₂-based HSC as a function of current density.

Figure 54. Cycling performances of S₋, M₋, and L_CNG/Co(OH)₂-based HSCs measured at 16 A g⁻¹ for 5000 cycles.

Figure 55. Ragone plots of S₋, M₋, and L_CNG/Co(OH)₂-based HSCs.

Figure 56. Schematic illustration for the fabrication process of HIH-LDH.

Figure 57. TEM image of HCS@ZIF-67s synthesized without introduction of carboxylic groups to HCS surfaces.

Figure 58. TEM images of (a) SiO₂ microsphere and (b, c) micro-sized HCS.

Figure 59. TEM images of (a) HCS@ZIF-67-1, (b) HCS@ZIF-67-2, (c, d) HIH-LDH-1, and (e, f) HIH-LDH-2.

Figure 60. SEM images of (a) HCS, (b) HCS@ZIF-67-2, (c) HIH-LDH-2, and (d) HIH-LDH-1.

Figure 61. TEM images of (a) pristine ZIF-67 and (b) H-LDH.

Figure 62. (a) HR-TEM image and (b) SAED pattern of HIH-LDH-2.

Figure 63. (a) STEM image, (b) STEM elemental mapping images (C, O, Ni, and Co), and (c) STEM-EDX line analysis result of HIH-LDH-2.

- Figure 64.** EDX spectrum of HIIH-LDH-2.
- Figure 65.** (a) XRD spectra of HCS, HCS@ZIF-67-2, and HIIH-LDH-2.
(b) XRD spectra of H-LDH, HIIH-LDH-1, and HIIH-LDH-2.
- Figure 66.** TGA curves of H-LDH, HIIH-LDH-1, and HIIH-LDH-2.
- Figure 67.** The high-resolution XPS patterns of H-LDH and HIIH-LDH-2: (a) C 1s. (b) Ni 2p. (c) Co 2p.
- Figure 68.** (a) Nitrogen adsorption/desorption plots and (b) pore-size distribution curves of H-LDH, HIIH-LDH-1, and HIIH-LDH-2.
- Figure 69.** CV curves of H-LDH, HIIH-LDH-1, and HIIH-LDH-2 at the scan rate of 20 mV s^{-1} .
- Figure 70.** CV curves of (a) H-LDH, (b) HIIH-LDH-1, and (c) HIIH-LDH-2 with different scan rates.
- Figure 71.** GCD curves of (a) H-LDH, (b) HIIH-LDH-1, and (c) HIIH-LDH-2 with different current densities.
- Figure 72.** Specific capacity of H-LDH, HIIH-LDH-1, and HIIH-LDH-2 as a function of current density.
- Figure 73.** Nyquist plots of H-LDH, HIIH-LDH-1, and HIIH-LDH-2 in the frequency range from 10 mHz to 100 kHz. The inset shows the high-frequency region of the plots.

- Figure 74.** Cycling performances of H-LDH, HII-LDH-1, and HII-LDH-2 measured at 10 A g^{-1} for 10000 cycles.
- Figure 75.** Electrochemical results of MPRGO: (a) GCD curves with different current densities. (b) Specific capacitance as a function of current density. (c) Nyquist plot (inset: high-frequency region of the plot).
- Figure 76.** Schematic diagram of the assembled HSC device (HII-LDH-2//MPRGO).
- Figure 77.** CV curves of HII-LDH-2-based HSC under various voltage windows, which were measured at 50 mV s^{-1} .
- Figure 78.** Electrochemical results of HII-LDH-2//MPRGO: (a) CV curves with different scan rates. (b) GCD curves under various current densities. (c) Specific capacity as a function of current density.
- Figure 79.** Ragone plot of HII-LDH-2-based HSC.
- Figure 80.** Cycling performances of HII-LDH-2-based HSC measured at 10 A g^{-1} for 10000 cycles.

List of Tables

- Table 1.** Elemental composition data of various-sized ZIF-67 crystals obtained by EDX measurements.
- Table 2.** Elemental composition data of various-sized CNG/Co(OH)₂ obtained by EDX measurements.
- Table 3.** Rate capabilities (5–80 A g⁻¹) and cycle stabilities (10 A g⁻¹, 10000 cycles) of H-LDH, HIH-LDH-1, and HIH-LDH-2.

Table of Contents

Abstract	i
List of Abbreviations	v
List of Figures	xi
List of Tables.....	xx
Table of Contents	xxi
1. Introduction	1
1.1. Background	1
1.1.1. Supercapacitors (SCs)	1
1.1.1.1. Classification of SC electrode materials.....	4
1.1.1.2. Structural design of SC electrode materials.....	8
1.1.1.3. Device configuration	13
1.1.2. Metal-organic framework (MOF)	16
1.1.2.1. MOF derivatives as SC electrode materials.....	19
1.1.2.2. Zeolitic imidazolate framework (ZIF).....	24
1.2. Objectives and Outlines	26
1.2.1. Objectives	26
1.2.2. Outlines.....	26

2. Experimental Details	30
2.1. ZIF-8-derived ZnO@carbon/CNF for SC electrodes	30
2.1.1. Materials	30
2.1.2. Fabrication of ZIF-8 nanocrystals	30
2.1.3. Fabrication of ZPCNF	31
2.1.4. Fabrication of ZIF-8/PAN-C	32
2.1.5. Characterization	32
2.1.6. Electrochemical measurements.....	34
2.2. ZIF-67-derived Co₃O₄/Co(OH)₂ for HSC electrodes	35
2.2.1. Materials	35
2.2.2. Fabrication of various-sized ZIF-67 crystals	35
2.2.3. Fabrication of various-sized CNG/Co(OH) ₂	36
2.2.4. Fabrication of pure Co ₃ O ₄ and Co(OH) ₂	37
2.2.5. Fabrication of MPRGO	37
2.2.6. Characterization	38
2.2.7. Electrochemical measurements.....	39
2.2.8. Fabrication of all-solid-state hybrid supercapacitor (HSC).....	41
2.3. ZIF-67-derived Ni-Co LDH/HCS for HSC electrodes	42
2.3.1. Materials	42
2.3.2. Fabrication of micro-sized HCSs	42
2.3.3. Fabrication of HCS@ZIF-67s.....	43
2.3.4. Fabrication of HIH-LDHs.....	44
2.3.5. Characterization	45

2.3.6. Electrochemical measurements.....	46
2.3.7. Fabrication of all-solid-state hybrid supercapacitor (HSC).....	47
3. Results and Discussion	48
3.1. ZIF-8-derived ZnO@carbon/CNF for SC electrodes	48
3.1.1. Fabrication process of ZPCNF.....	48
3.1.2. Physicochemical properties of the samples	51
3.1.3. Electrochemical properties of the samples	67
3.2. ZIF-67-derived Co₃O₄/Co(OH)₂ for HSC electrodes	76
3.2.1. Fabrication process of CNG/Co(OH) ₂	76
3.2.2. Physicochemical properties of the samples	78
3.2.3. Electrochemical properties of the samples	97
3.2.4. Characterization and electrochemical properties of negative electrode material (MPRGO)	108
3.2.5. Studies of the hybrid supercapacitor (HSC).....	114
3.3. ZIF-67-derived Ni-Co LDH/HCS for HSC electrodes	125
3.3.1. Fabrication process of HIH-LDH.....	125
3.3.2. Physicochemical properties of the samples	129
3.3.3. Electrochemical properties of the samples	148
3.3.4. Characterization and electrochemical properties of negative electrode material (MPRGO)	160
3.3.5. Studies of the hybrid supercapacitor (HSC).....	162

4. Conclusion	170
Reference	173
국문초록.....	180

1. Introduction

1.1 Background

1.1.1. Supercapacitors (SCs)

Supercapacitors (SCs) are one of the most promising energy systems in the modern industry together with fuel cells and batteries. Owing to their high power density and long cycle life, SCs have been applied across a range of industrial fields requiring fast storage and retrieval of energy, including motor starter system, regenerative braking, and turbine pitch control [1–10]. Recently, the application of SCs has been extended to the power source of electric vehicles (EVs). For example, the trolley bus and electric tramcar in **Figure 1a** and **1b** use SC as the power source, fully charged within very short time (30–90 seconds) and able to travel more than 5 km at a time [11]. However, the above case is the experimental attempt, and the application of SC as primary energy supplying system for transportation is limited because the energy density is insufficient at the current level. The Ragone plot in **Figure 1c** shows power density vs. energy density of various energy systems, demonstrating that SCs bridge the gap of power density and energy density between batteries and conventional electrolytic

capacitors [12]. Generally, SCs deliver the high power density above 10 kW kg^{-1} , but relatively low energy density ($<20 \text{ Wh kg}^{-1}$) compared with that of batteries. Thus, for more comprehensive application of SCs, it is imperative to develop SCs with improved energy density which is closed to that of batteries, while maintaining their inherent characteristics (*i.e.*, high power density, long lifespan). It is well known that the energy density of SC depends on the specific capacitance and operating voltage window according to the formula $E = 1/2CV^2$, where C is the capacitance and V is the voltage window [13–16]. To increase these values, several factors should be considered in preparing SC, which are the type of electrode material applied, the rational design of its structure, and the device configuration.

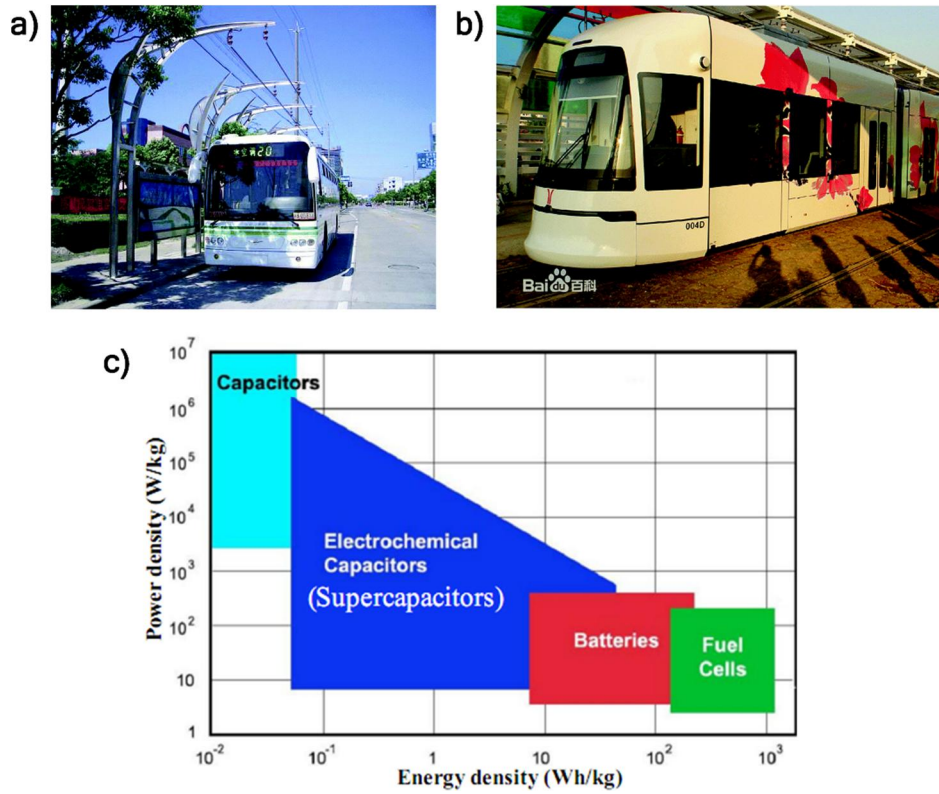


Figure 1. (a, b) Trolley bus and Electric tramcar which use the SC as a power source [11]. (c) Ragone plot showing the power density vs. energy density of various energy systems [12].

1.1.1.1. Classification of SC electrode materials

According to the charge storage mechanism, SC electrode materials can be classified into three types: electric double layer capacitor (EDLC), pseudocapacitor, and battery-type materials (**Figure 2**) [17].

The EDLC materials electrostatically store charge by forming an electric double layer at the interface between their conductive surface and the electrolyte. The representative EDLC materials are carbon-based materials such as activated carbon (AC), carbon nanotube (CNT), carbon nanofiber (CNF), and graphene [18–21]. Among them, graphene has been attracting extensive attention due to its high electrical conductivity and large theoretical surface area ($2630 \text{ m}^2 \text{ g}^{-1}$) derived from honeycomb sp^2 hybridized carbon structure [22–25].

On the other hand, pseudocapacitor uses not only electrochemical adsorption/desorption of ions at the electrode/electrolyte interface but also their rapid surface faradaic redox reaction for charge storage. Since the first discovery of the pseudocapacitive behaviors of RuO_2 in 1975, it has been reported that some metal oxides (*e.g.*, RuO_2 , MnO_2 , V_2O_5 , ZnO) exhibit this unique charge storage mechanism [26–29]. Because pseudocapacitance has more than 10 times better charge storage ability than simple electrostatic capacitance, pseudocapacitor

materials have attracted widespread attention from researchers [17]. In particular, since capacitive materials (*i.e.*, EDLC and pseudocapacitor materials) store charge by only surface confined reaction, the charge storage of them is not limited by ion diffusion within their crystalline framework [11,12]. Therefore, the charge storage of capacitive materials is proceeded in a rapid and reversible manner, which leads to high rate performance. Additionally, capacitive materials commonly display good cycle stability because no phase transition occurs during the charge storage process of these materials [17].

Meanwhile, battery-like materials (*e.g.*, Ni(OH)₂, NiO, Co(OH)₂, Co₃O₄, Ni-Co layered double hydroxide (LDH)) have also been applied to SC electrode materials as the positive electrode of hybrid supercapacitor (HSC) [30–35]. In the charge storage process, battery-like materials are similar to pseudocapacitor materials in that they involve faradaic redox reactions, but differ in that the bulk phase of them participates in the process. Owing to above characteristic, battery-type materials typically have superior charge storage ability than capacitive materials, but their charge storage is limited by ion diffusion within the bulk structure and accompanies phase transition, resulting in inferior rate and cycle performances [11,12].

Notably, capacitive materials and battery-like materials can also be distinguished by their different electrochemical profile [36]. For capacitive materials, the amount of charge stored is linearly proportional to the applied potential within the window of interest. Accordingly, these materials provide rectangular-shaped cyclic voltammetry (CV) curve and linear, triangular-shaped galvanostatic charge/discharge (GCD) plot. On the contrary, the charge storage of battery-type materials occurs in the specific potential, and thus demonstrate CV curve with obvious redox peaks and flat charge/discharge plateau in their GCD plot. When describing the electrochemical performance of battery-type materials, the unit of capacity (mAh g^{-1}) should be utilized because their electrochemical profile is not matched with the definition of capacitance (F g^{-1}) [37].

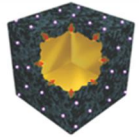
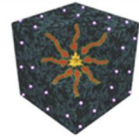
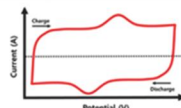
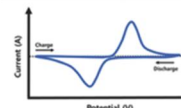
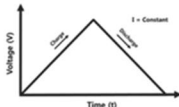
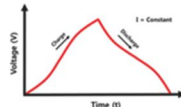
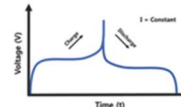
Types of energy storage device	Non-faradaic	Faradaic		
	Electrical double layer capacitor (EDLC)	Surface redox	Intercalation	Battery (based on intercalation)
Mechanism	Reversible ion adsorption/desorption without phase transition	Continuous change in oxidation state without phase transition	Intercalation and change in oxidation state without phase transition	Intercalation and change in oxidation state with phase transition
Kinetics		$i \sim v$ (surface confined)		$i \sim v^{0.5}$ (diffusion controlled)
Capacity	0.17 ~ 0.2 e ⁻ per atom of accessible surface	ca. 2.5 e ⁻ per atom of accessible surface, depending on oxidation state		1-3 e ⁻ per atom of bulk phase, depending on oxidation state
Electrochemical features				
				
				

Figure 2. Classification of SC electrode materials according to charge storage mechanisms (EDLC, pseudocapacitor, and battery-type materials) [17].

1.1.1.2. Structural design of SC electrode materials

In addition to the intrinsic properties of the applied electrode material, rational design of its structure is another important consideration to improve electrochemical performance. Particularly, the surface area of SC electrode material is highly related to its electrochemical performance. By increasing the surface area, capacitive materials can enhance their capacitance based on the enlarged electrochemical interface, and battery materials can show a faster charge/discharge rate due to the shortened ion diffusion length [11].

To produce SC electrodes with large surface area, many researchers have proposed diverse materials with porous structures [38–40]. Among the various pore systems, it has been reported that narrow distribution of mesopores (2–50 nm) is advantageous for obtaining decent electrochemical performance rather than wide pore size distribution, which includes pores with too small size [39]. The mesopores provide not only a large surface area but also a suitable pathway for electrolyte ions facilitating effective charge storage, while micropores having a pore size of less than 0.5 nm are hardly accessible to electrolyte ions [40].

Hollow structure is also one of the favorable structures as SC

electrode material. The merits of hollow structure as the electrode material come from its well-defined interior void, which can enhance charge storage ability by enlarging the electrochemical interface [41,42]. Moreover, this internal void space can act as the ‘ion reservoir’ for electrolyte ions, which supports a stable supply of electrolyte throughout the architecture during the rapid charge/discharge reaction [43]. As such, SC electrode materials with the hollow structure can be fully exploited even under severe rate condition, resulting in drastically increased rate capability. In general, especially in the case of hollow carbon sphere (HCS), a hard template method is applied to prepare hollow architectures [44–46]. As shown in **Figure 3**, hard template method consists of two successive step, which is the coating of precursor (*e.g.*, polydopamine (PDA)) on hard template (*e.g.*, SiO₂ sphere) and template removal after carbonization process [46].

Meanwhile, the electrical conductivity is another crucial factor in determining the electrochemical performance of SC electrode materials [47]. When the conductivity is insufficient, the high internal resistance causes poor electrochemical performance of the electrode material. In this regard, one-dimensional (1D) structures in the form of

tubes or fibers have received much attention as beneficial architectures of SC electrode materials; 1D materials are known for their excellent electron mobility owing to their directional structure that can act as the ‘conductive highway’ of electrons [48–50]. Amongst various techniques for fabricating 1D materials, electrospinning has been widely used as the facile and versatile method [51–55]. As illustrated in **Figure 4**, electrospinning uses the electric force between the polymer solution charged with high voltage and the collector to produce polymer fibers, whose diameter can be controlled by several parameters (*e.g.*, polymer solution concentration, distance/applied voltage between syringe needle and collector) [55]. These electrospun polymer fibers, especially composed of polyacrylonitrile (PAN) or poly(vinyl alcohol) (PVA), can be converted to CNFs through well-controlled heat treatment process, including stabilization and carbonization.

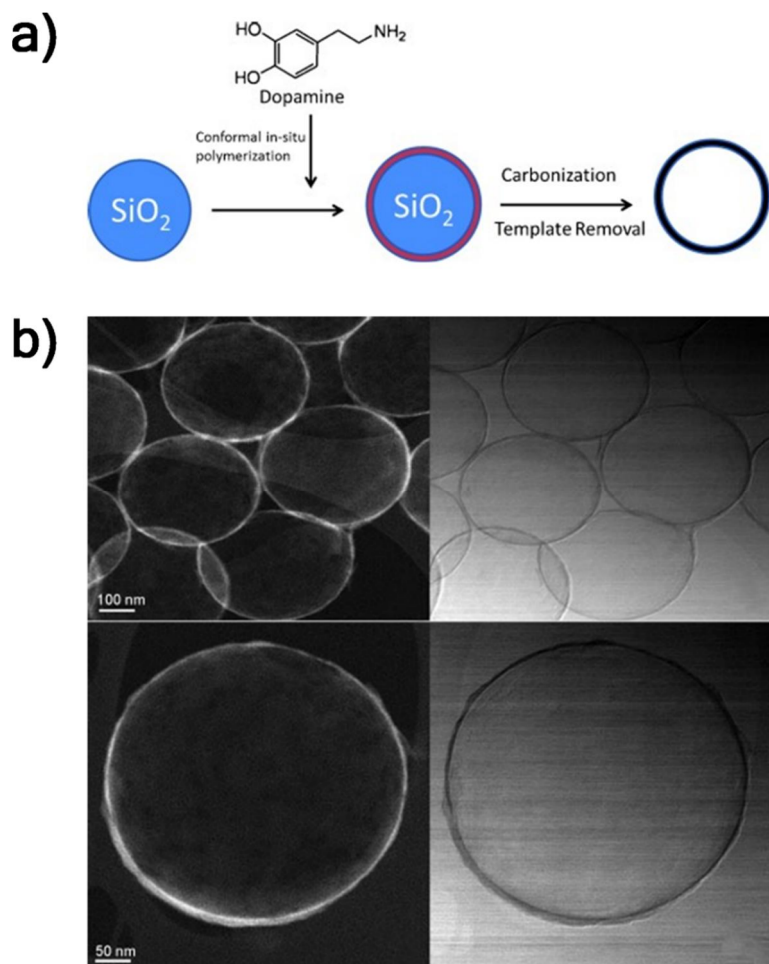


Figure 3. (a) Schematic illustration of the synthesis of HCS using SiO_2 sphere as the hard template and PDA as the carbon source. (b) Microscopy images of HCSs obtained using various TEM techniques [46].

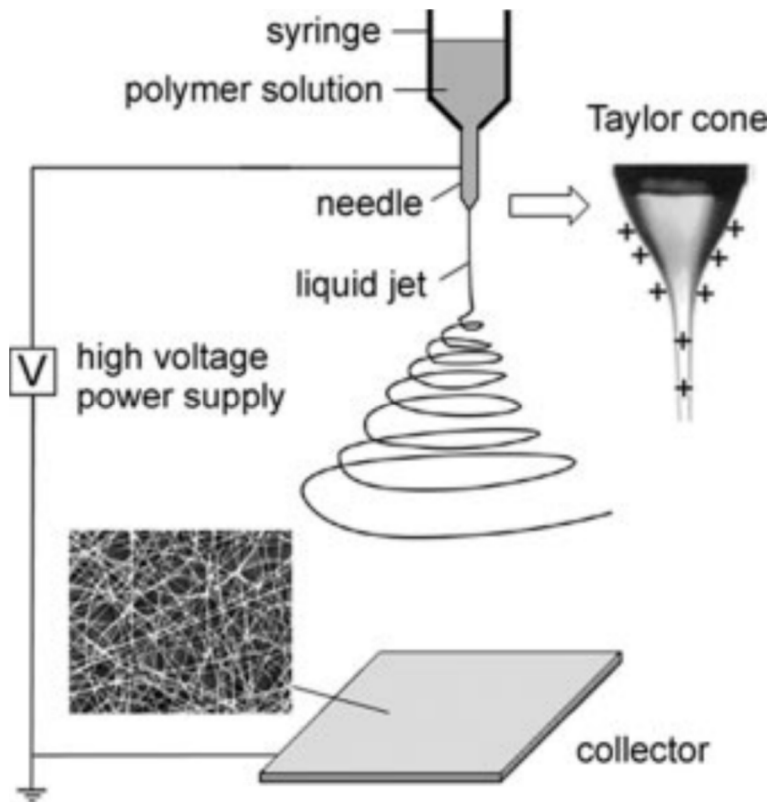


Figure 4. Schematic illustration of the basic setup for electrospinning process. The inset shows a typical SEM image of electrospun poly(vinyl pyrrolidone) (PVP) nanofibers [55].

1.1.1.3. Device configuration

For manufacturing SC cells with wide voltage windows, it is necessary to utilize organic electrolytes or to alter the device configuration. In the case of symmetric SCs using aqueous electrolytes, it is difficult to possess an operating voltage window exceeding 1 V due to the water decomposition [11]. Interestingly, the voltage window of the cell can be greatly expanded by applying an organic electrolyte, which is prepared by dissolving conductive salt (*e.g.*, tetraethylammonium tetrafluoroborate (TEABF₄)) in organic solvent (*e.g.*, propylene carbonate (PC)) [56]. However, there are critical drawbacks associated with organic electrolytes, including high cost, flammability, volatility, toxicity, and low electrochemical performance derived from inferior ion conductivity.

Meanwhile, another strategy for increasing the voltage window of the SC cell has been suggested, which is engineering the device configuration. Particularly, the hybrid supercapacitor (HSC) configuration has attracted great attention from researchers in that it not only enhances the voltage window of the cell but also the charge storage capacity (**Figure 5**) [57–62]. Unlike symmetric SC that uses the same capacitive material for both electrodes, HSC uses two

different active materials for each electrode. In specific, the battery-like material is employed for the positive electrode and the capacitive material is exploited for the negative electrode. By adopting the above configuration, the capacitance of the capacitive electrode can be maximally utilized and thus the overall voltage window of HSC cell is enlarged, while that of symmetric SC can not exceed the maximum working potential range of electrodes used [63]. Besides, since the battery electrode shows many times higher capacity than the capacitive electrode, the HSC device can have improved charge storage capability compared to the symmetric SC [57]. Hence, the HSC configuration has been able to successfully integrate the high energy of the battery with the high power and long lifespan of the SC.

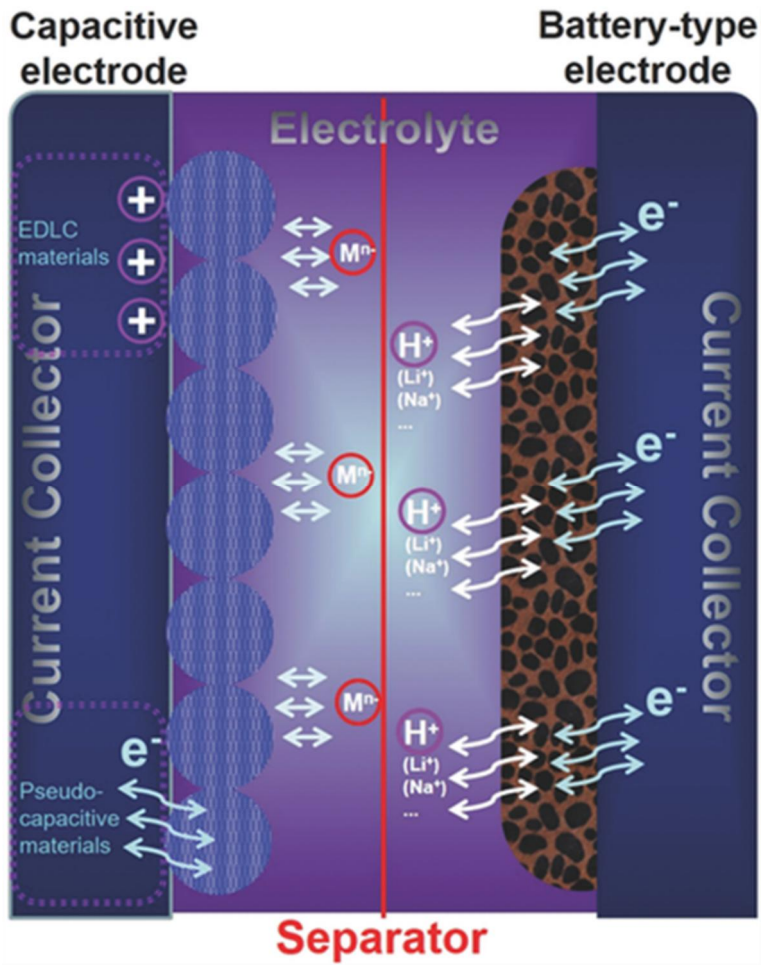


Figure 5. Schematic diagram of typical HSC device structure [57].

1.1.2. Metal-organic framework (MOF)

Since the term MOF was first introduced by Yaghi and his co-workers in 1995, MOFs have received much interest from the research community as the promising porous material with extremely large surface area [64,65]. Typically, MOFs possess their own crystalline structure constructed by the coordination of certain metal clusters/ions and proper organic ligands (**Figure 6a**) [66]. Specifically, the commonly used metal ions are transition metals (*e.g.*, Zn, Co, Ni, Fe, Cu) and the organic ligands act as the bridge between them to form unique arrangement, which generates numerous micropores. In other words, the MOFs with different physicochemical properties can be synthesized by applying various combinations of primary building blocks (metal ions and organic ligands). Moreover, it is also available to enhance the functionality of MOF by utilizing functionalized organic ligands in the synthesis process. Owing to a variety of primary building blocks, 20000 different MOFs with controlled crystal sizes, shapes, pore sizes, and chemical compositions have been demonstrated so far [67]. Based on such tunable structures, MOFs have been intensively applied in diverse fields, including gas storage, separation, catalysis, sensing, and drug delivery (**Figure 6b**) [68–71]. Until now,

multifarious synthetic strategies such as solvothermal, electrochemical, mechanochemical method, microwave-assisted heating, and chemical vapor deposition have been developed for rapid and large-scale production of MOFs with high quality [67,72].

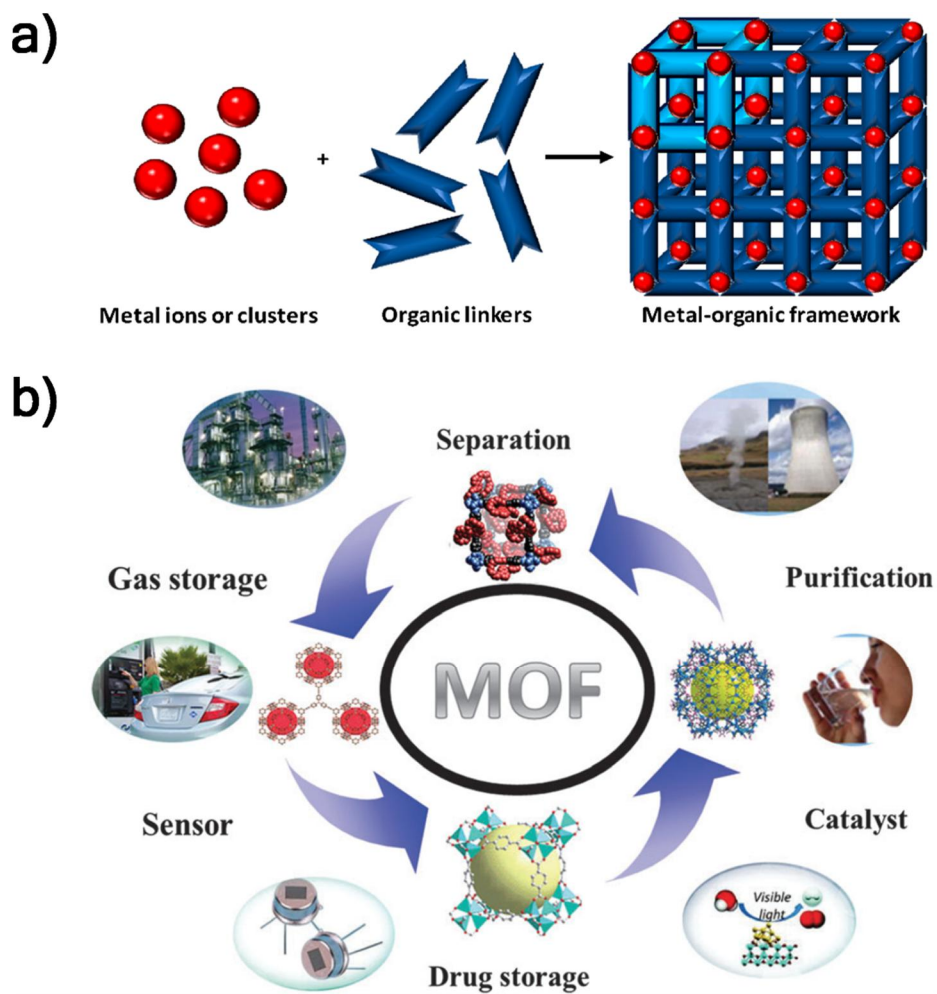


Figure 6. (a) Schematic diagram illustrating the formation of MOF [66]. (b) Various application fields of MOFs [71].

1.1.2.1. MOF derivatives as SC electrode materials

In recent years, there have been increasing attempts to utilize MOF as the precursor and sacrificial template for manufacturing SC electrode materials [73–77]. Because MOFs involve both organic and inorganic species within their chemical structures, these intriguing organic-inorganic hybrid materials can be converted into the architecture comprised of carbon, metal oxides, metal hydroxides, *etc.* through appropriate procedures. MOF derivatives offer many advantages in application as SC electrode materials. First, the chemical composition of MOF derivatives can be easily adjusted by applying specific heat or chemical treatments to diverse MOFs. Second, since MOF is the porous structure where organic/inorganic precursors are orderly arranged at the atomic level, it maintains porosity even after being transformed into MOF derivatives and provides the huge surface area. Accordingly, the large electrochemical interface and the short ion diffusion length can be attained, which improve charge storage capability and rate performance of MOF derivatives. Finally, the fabrication of MOF derivatives can be carried out in a low-cost and facile manner, which makes large-scale production available [67].

The transformation strategies from MOF-based templates to MOF

derivatives are briefly classified into three types: carbonization under inert atmosphere, calcination with reactive gases, and chemical reaction in the presence of metal salts (**Figure 7**) [78]. As a result of the carbonization of MOF templates at the high temperature (>900 °C) and the removal of metal ions therein, the orderly distributed organic linkers in MOFs can be converted to highly porous carbon networks [79,80]. On the other hand, when MOF templates are calcined in air over the certain temperature range, the metal precursors in MOFs are converted to metal oxides, while the organic ligands are decomposed [81–84]. Particularly, the ordered arrangement of the metal precursors in MOFs and the gas release from the ligand decomposition allow the MOF-derived metal oxide architectures to possess a unique morphology (**Figure 8a**) [83]. Meanwhile, hollow particles consisting of metal hydroxide shells can also be prepared *via* a well-controlled ion-exchange reaction between MOF templates and metal salts in the solution (**Figure 8b**) [85–88]. Owing to the distinctive structural features, MOF derivatives prepared by various methods have delivered better electrochemical performances compared with those of conventional materials.

Nevertheless, the low electrical conductivity of MOF derivatives is

still a challenging issue, which is attributed to the lack of connection between the particles [89,90]; MOF derivatives are usually in the form of particles. Moreover, in the case of Ni- or Co-based MOF derivatives, rate and cycle performances are insufficient because they are composed solely of battery-type materials. Hence, a variety of hybrid forms with carbon materials such as CNT, CNF, and HCS have gained considerable attention to address the ingrained issues of MOF derivatives [91–94].

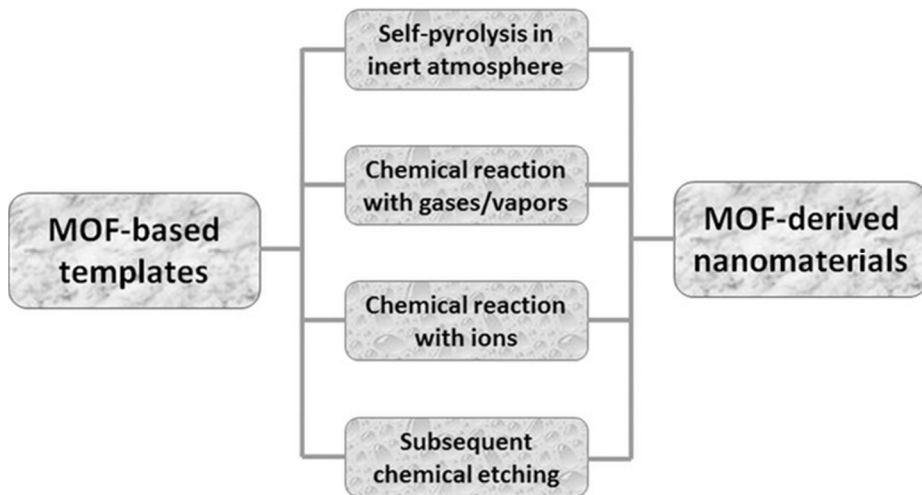


Figure 7. An overview of the transformation strategies from MOF-based templates to MOF derivatives [78].

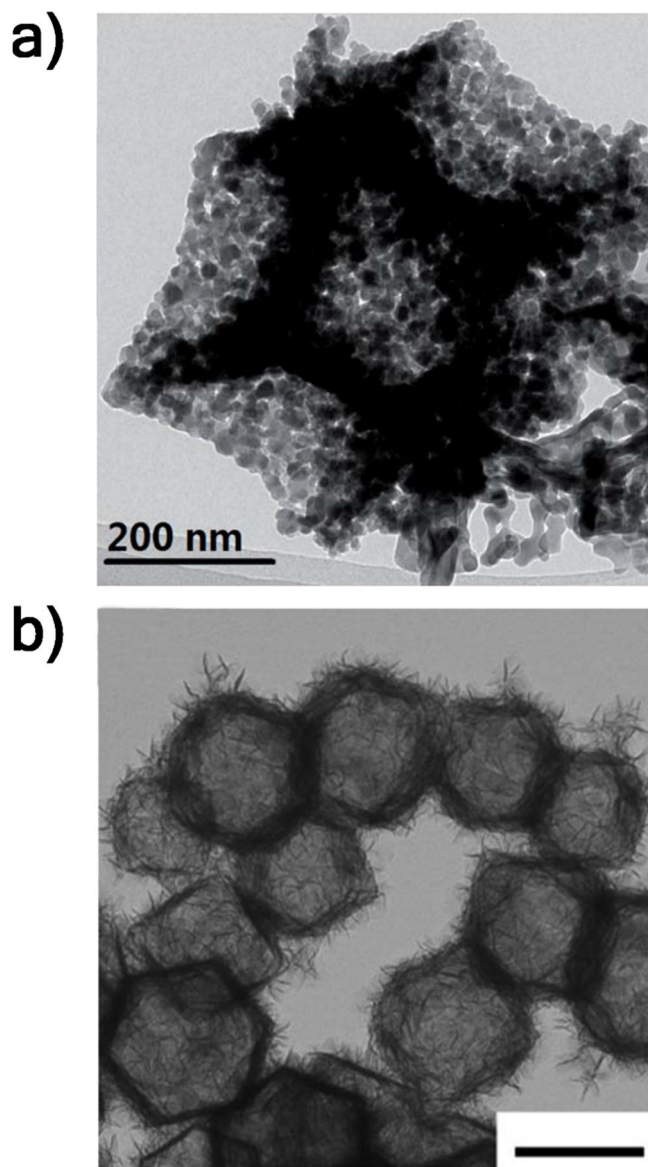


Figure 8. (a) Co_3O_4 dodecahedron and (b) hollow Mg-Co LDH architectures synthesized using MOF templates [83,87].

1.1.2.2. Zeolitic imidazolate framework (ZIF)

ZIFs are the sub-family of MOFs, which are made up of the coordination between transition metal ions (especially Zn or Co cations) and imidazolate linkers [95]. In particular, the unique metal–imidazolate–metal angle of ZIFs, which is analogous to the Si–O–Si angle (145°) of aluminosilicate zeolites, allows them to have a zeolite-like topology. Because of this topological feature, ZIFs possess higher thermal and chemical stability compared with those of other MOFs, enabling them to operate over wider temperature range and harsh chemical condition. Furthermore, ZIFs generally exhibit hydrophobicity due to the absence of oxygen in their chemical structure, and thus can be manipulated more efficiently in humid environments. Notably, ZIFs can be used effectively as the precursor to SC electrode material since the high thermal/chemical stability of ZIF is advantageous in controlling the conversion process to its derivatives. ZIFs are usually synthesized through simple solvothermal method of solution containing solvents (*e.g.*, methanol, water), hydrated metal salts, and imidazole species (*e.g.*, 2-methylimidazole (Hmim)) (**Figure 9**) [96–98].

1.2. Objectives and Outlines

1.2.1. Objectives

The aim of this dissertation is to describe the methods for fabricating high-performance SC electrodes by using ZIF derivatives/carbon materials with beneficial structures for charge storage. In detail, ZIF-8/ZIF-67 derivatives, various carbon materials with 1D/hollow structure, and their hybrids are applied to achieve improved charge storage ability, rate capability, and cycle performance. The physicochemical and electrochemical properties of the prepared SC electrode materials are investigated systematically and thoroughly. Additionally, in the case of battery-type materials, the hybrid supercapacitor (HSC) device is also constructed and examined for practical applicability.

1.2.2. Outlines

This dissertation focused on the synthesis of diverse ZIF derivatives/carbon structures and evaluation of their electrochemical performances as the SC electrode materials. This dissertation involves the following subtopics:

- I. ZIF-8-derived ZnO@carbon/CNF for SC electrodes
- II. ZIF-67-derived Co₃O₄/Co(OH)₂ for HSC electrodes
- III. ZIF-67-derived Ni-Co LDH/HCS for HSC electrodes

A detailed outline of the study is as follows:

1. A hybrid structure composed of well-dispersed ZnO quantum dots (QDs) in porous carbon (ZnO QDs@carbon) and CNF (ZPCNF-4) is synthesized by single carbonization of electrospun ZIF-8/PVA nanofibers. During the carbonization process, PVA in the main axis of the architecture serves as not only the CNF precursor but also the oxygen source for the surrounding ZIF-8s to form ZnO QDs@carbons. By combining the hierarchical porous structure and 1D morphology, ZPCNF-4 exhibits the high surface area and enhanced conductivity, which are crucial factors for the SC electrode material. Accordingly, ZPCNF-4 shows outstanding electrochemical performance with high capacitance (346 F g⁻¹ at 0.5 A g⁻¹), reliable rate capability (79% capacitance retention at 8 A g⁻¹), and long cycle life (85% capacitance retention after 5000 cycles).

2. A novel hybrid structure of homogeneously distributed Co_3O_4 nanograins on the hexagonal $\text{Co}(\text{OH})_2$ plate ($\text{CNG}/\text{Co}(\text{OH})_2$) is fabricated using the one-pot hydrothermal reaction of ZIF-67. Particularly, because Co-containing ZIF-67 serves as the self-template during the hydrothermal conversion process, various-sized $\text{CNG}/\text{Co}(\text{OH})_2$ can be synthesized using different sizes of ZIF-67 as the precursor material. Owing to their unique structural features, the $\text{CNG}/\text{Co}(\text{OH})_2$ architectures effectively boost the electrochemical activation of Co_3O_4 and $\text{Co}(\text{OH})_2$ within them by alleviating aggregation issues. Among the various-sized structures, large-sized one ($\text{L_CNG}/\text{Co}(\text{OH})_2$) displays the highest capacity of 184.9 mAh g^{-1} (at 1 A g^{-1}), indicating that the electrochemical performance is improved as the size of hybrid increases. Furthermore, multifarious all-solid-state HSCs are assembled with various-sized $\text{CNG}/\text{Co}(\text{OH})_2$ as the positive electrode and mesoporous plasma-reduced graphene oxide (MPRGO) as the negative electrode. Notably, the as-prepared HSCs deliver the maximum energy density of 37.6 Wh kg^{-1} and peak power density of 47 kW kg^{-1} .

3. A unique hybrid structure consisting of ZIF-67-derived hollow Ni-Co LDH (H-LDH) and HCS (HIH-LDH) is produced using the composite of ZIF-67s and HCS (HCS@ZIF-67) as the precursor. Particularly, when the ZIF-67 content in the precursor is optimized, the distinctive hollow-in-hollow structure (HIH-LDH-2) can be obtained by successfully distributing H-LDHs on the HCS carbon shell. Due to their structural characteristics, HIH-LDH-2 delivers the high specific capacity (156.4 mAh g^{-1} at 5 A g^{-1}) and excellent cycle stability (74% capacity retention after 10000 cycles). Notably, during the charge storage process, the hollow-in-hollow structure of HIH-LDH-2 effectively decreases the ion diffusion path, resulting in drastically enhanced rate performance (70% retention of its highest capacity at 80 A g^{-1}). Moreover, the all-solid-state HSC is fabricated using HIH-LDH-2 as the positive electrode and MPRGO as the negative electrode, which demonstrates the maximum energy density of 34.5 Wh kg^{-1} and peak power density of 55 kW kg^{-1} .

2. Experimental Details

2.1. ZIF-8-derived ZnO@carbon/CNF for SC electrodes

2.1.1. Materials

Zinc nitrate hexahydrate ($\text{Zn}(\text{NO}_3)_2 \cdot 6\text{H}_2\text{O}$, 98%), 2-methylimidazole (Hmim, 99%), poly(vinyl alcohol) (PVA, MW=85000–124000), and polyacrylonitrile (PAN, MW=150000) were purchased from Sigma-Aldrich. N,N-Dimethylformamide (DMF, 99.5%) was supplied from Junsei Chemical. All of chemicals were used as received without further purification. Deionized (DI) water was used in all experiment.

2.1.2. Fabrication of ZIF-8 nanocrystals

ZIF-8 nanocrystals were synthesized in aqueous system according to the previous report with minor modification [97]. In the typical synthesis, Hmim (22.7 g) was dissolved in DI water (80 ml) with constant stirring. Subsequently, $\text{Zn}(\text{NO}_3)_2 \cdot 6\text{H}_2\text{O}$ (1.17 g) in DI water (8 ml) was rapidly poured into the above solution with stirring for another 5 min. Finally, the white powders were collected by centrifugation and washed with DI water several times. As-prepared

ZIF-8 nanocrystals were dried at 60 °C under vacuum before the characterization.

2.1.3. Fabrication of ZPCNF

The hybrid structure of ZnO QDs@carbon and CNF (ZPCNF) is fabricated by carbonization of electrospun ZIF-8/PVA nanofibers. The precursor solutions were prepared by dispersing a given amount of ZIF-8 (2 or 4 wt% of total solution) in the 8 wt% PVA aqueous solution. The electrospinning process was carried out by feeding the above solution through the metallic needle at the rate of 0.36 ml h⁻¹. The needle was placed at distance of 12 cm from the collector and the high voltage (10 kV) was applied. Subsequently, the resulting ZIF-8/PVA nanofiber mat was carefully peeled off from the collector and transferred to the tube furnace. They were first stabilized in air at 170 °C for 24 h and then carbonized in N₂ atmosphere at 650 °C for 3 h. The carbonized samples were named ZPCNF-2 and ZPCNF-4, respectively, depending on the amount of ZIF-8 used (2 or 4 wt% in precursor solution). Pristine ZIF-8 nanocrystals and PVA nanofibers were carbonized by the same method above to prepare carbonized

ZIF-8 nanocrystals (ZIF-8-Cs) and PVA-based carbon nanofibers (PCNFs), respectively, as control samples for comparison.

2.1.4. Fabrication of ZIF-8/PAN-C

ZIF-8/PAN-C was prepared by carbonization of electrospun ZIF-8/PAN nanofibers. Electrospinning solution was prepared by dispersing a given amount of ZIF-8 (5 wt% of total solution) in the 10 wt% PAN solution in DMF. The electrospinning process was performed by feeding the precursor solution with injection speed of 0.6 ml h^{-1} . The distance and applied voltage between the needle and the collector were fixed at 12 cm and 10 kV, respectively. Subsequently, the collected fiber mat was stabilized in air at $270 \text{ }^{\circ}\text{C}$ for 1 h and carbonized in N_2 atmosphere at $650 \text{ }^{\circ}\text{C}$ for 3 h. ZIF-8/PAN-C was fabricated as the control sample to compare the structural properties with ZPCNF.

2.1.5. Characterization

Scanning electron microscopy (SEM) and transmission electron microscopy (TEM) images were obtained with JSM-6701F (JEOL) and JEM-2100 (JEOL), respectively. High-resolution TEM (HR-TEM)

images were acquired with JEM-3010 (JEOL). Elemental mapping of ZPCNF was conducted by scanning TEM (STEM) mode of Tecnai F20 (FEI). X-ray photoelectron spectroscopy (XPS) was performed with Sigma probe (VG Scientific). Raman spectra were recorded with LabRAM HV Evolution spectrometer (HORIBA) using the laser of wavelength 532 nm. X-ray diffraction (XRD) spectra were obtained with New D8 Advance (Bruker) at 40 kV and 30 mA (Cu-K α radiation, $\lambda=0.15418$ nm). Thermogravimetric analysis (TGA) was carried out using Pyris 6 thermogravimetric analyzer (PerkinElmer) under ambient condition with the heating rate of 10 °C min⁻¹. N₂ adsorption/desorption isotherms were measured using ASAP 2000 surface area measurement analyzer (Micromeritics) at liquid nitrogen temperature. The specific surface area and pore distribution of the samples were acquired by applying the Brunauer-Emmett-Teller (BET) and Barrett-Joyner-Halenda (BJH) method, respectively. The electrical conductivities of the samples were investigated by four-probe method using KEITHLY 2400 (KEITHLY). The shear viscosities of sample solutions were examined as a function of the shear rate ranging from 0.01 to 400 s⁻¹ using AR2000 Advanced Rheometer (TA Instruments).

2.1.6. Electrochemical measurements

All the electrochemical measurements were conducted on the three electrode system using platinum wire as the counter electrode and Ag/AgCl as the reference electrode in 1 M Na₂SO₄ electrolyte solution. To prepare the working electrode, as-prepared active materials (1.0 mg) were mixed with polyvinylidene fluoride (PVDF) binder (0.1 mg) in N-methyl-2-pyrrolidone (NMP) solvent, resulting in homogeneous paste. The resulting paste was subsequently coated onto the Ni mesh, followed by drying in oven at 80 °C before the measurements. The cyclic voltammetry (CV) and galvanostatic charge/discharge (GCD) tests were examined with WBCS 3000 (Wonatech) at various scan rates and current densities between -1.0 and 0 V. The electrochemical impedance spectroscopy (EIS) measurements were conducted using ZIVE SP2 (Wonatech) with the AC voltage of 10 mV amplitude in the frequency range from 100 kHz to 10 mHz. ZMAN software was used to obtain significant parameters from the Nyquist plots. The specific capacitances (C_{sp} , F g⁻¹) of the active materials were calculated from the corresponding GCD curves according to the following equation:

$$C_{sp} = \frac{I\Delta t}{m\Delta V}$$

I: discharge current

Δt : discharge time

m : amount of active material

ΔV : potential change during discharging

2.2. ZIF-67-derived $\text{Co}_3\text{O}_4/\text{Co}(\text{OH})_2$ for HSC electrodes

2.2.1. Materials

Cobalt nitrate hexahydrate ($\text{Co}(\text{NO}_3)_2 \cdot 6\text{H}_2\text{O}$, 98%), 2-methylimidazole (Hmim, 99%), and oleylamine (70%) were purchased from Sigma-Aldrich. Sodium hydroxide (NaOH, 98%) and ethanol ($\text{C}_2\text{H}_5\text{OH}$, 95%) were supplied from Samchun Chemical. All of chemicals were used without further purification. Deionized (DI) water was used in all experiment.

2.2.2. Fabrication of various-sized ZIF-67 crystals

The various-sized ZIF-67 crystals were synthesized in aqueous systems at room temperature according to the previous report with minor modification [98]. Over the synthesis process, the concentration of reagents played an important role in controlling crystal size. For the fabrication of small-sized ZIF-67 crystals (S_ZIF-67), Hmim (22.0 g) was dissolved in DI water (172 ml) with constant stirring.

Subsequently, $\text{Co}(\text{NO}_3)_2 \cdot 6\text{H}_2\text{O}$ (1.8 g) in DI water (12 ml) was rapidly added into the above solution. After 6 h of stirring, the resulting purple precipitates were collected by centrifuging, washed with DI water and ethanol for several times, and finally dried in vacuum oven at 60 °C. Middle- (M_ZIF-67) and large-sized ZIF-67 (L_ZIF-67) were simply synthesized by applying the same method above, but using the synthesis solution which was diluted twice or three times compared with that of S_ZIF-67, respectively.

2.2.3. Fabrication of various-sized CNG/Co(OH)₂

Small-, middle-, and large-sized Co_3O_4 nanograins-decorated $\text{Co}(\text{OH})_2$ sheet (S_, M_, and L_CNG/Co(OH)₂) were fabricated *via* hydrothermal treatment of S_, M_, and L_ZIF-67, respectively. For the preparation of S_CNG/Co(OH)₂, the mixture of as-synthesized S_ZIF-67 (0.1 g) and DI water (30 ml) was sufficiently sonicated to obtain clearly dispersed solution. Subsequently, the above solution was transferred into the autoclave with Teflon liner to proceed hydrothermal treatment process, which was conducted at 100 °C for 150 min. Finally, the resulting brown precipitates were acquired by centrifuging, washed with DI water and ethanol for several times, and

dried in vacuum oven at 60 °C. M_ and L_CNG/Co(OH)₂ were synthesized through the identical method to that of S_CNG/Co(OH)₂ except that the M_ or L_ZIF-67 was utilized as the precursor material, respectively.

2.2.4. Fabrication of pure Co₃O₄ and Co(OH)₂

The pure Co₃O₄ and Co(OH)₂ were synthesized by hydrothermal route according to the previous study for comparison [99]. For the preparation of pure Co₃O₄, the mixture of Co(NO₃)₂·6H₂O (0.291 g) and 0.1 M NaOH aqueous solution (20 ml) was hydrothermally treated at 200 °C for 24 h. In the case of pure Co(OH)₂, the solution of Co(NO₃)₂·6H₂O (0.291 g), oleylamine (2 ml), ethanol (10 ml), and DI water (20 ml) was transferred into the autoclave with Teflon liner, and kept at 180 °C for 12 h. The resulting pure Co₃O₄ and Co(OH)₂ were sufficiently washed with DI water and ethanol, and dried in vacuum oven before the characterization.

2.2.5. Fabrication of MPRGO

The mesoporous plasma-reduced graphene oxide (MPRGO) was fabricated by two-step process which included lyophilization of

graphene oxide (GO) solution and plasma reduction according to the previous study [20]. Firstly, GO solution (0.5 mg ml^{-1}) was obtained by modified Hummers' method which has been described elsewhere [8]. Afterwards, as-prepared GO solution was lyophilized for 2 days and subsequently reduced by plasma reduction, which was conducted using commercially available plasma apparatus (APP MyPL-200). The flow rate of carrier gas (Ar), applied plasma power, and the distance between the cathode ray tube and sample were fixed at 8 sccm, 200 W, and 0.5 cm, respectively. After the 2 seconds of plasma reduction, brownish GO turned into the black-colored MPRGO, which was kept in vacuum oven before the characterization.

2.2.6. Characterization

Field-emission scanning electron microscopy (FE-SEM, JEOL JSM-6701F), transmission electron microscopy (TEM, JEOL JEM-2100), high-resolution TEM (HR-TEM, JEOL JEM-3010), and atomic force microscopy (AFM, Park Systems NX-10) were utilized for observing the morphology of the samples. Chemical composition of the samples was examined using elemental mapping mode of scanning TEM (STEM, FEI Tecnai F-20), energy dispersive X-ray spectroscopy

(EDX), and X-ray photoelectron spectroscopy (XPS, VG Scientific Sigma probe). EDX measurements were performed using SEM equipment. X-ray diffraction (XRD, Bruker New D8 Advance) spectra was acquired with Cu-K α radiation ($\lambda=0.15418$ nm) for the phase analyses. Thermogravimetric analysis (TGA) was carried out using PerkinElmer Pyris 6 thermogravimetric analyzer under atmospheric condition. To investigate the structural properties of the samples, N₂ adsorption/desorption isotherms were measured using Micromeritics ASAP 2000 surface area measurement analyzer at 77 K. The specific surface area and pore size distribution of the samples were obtained by the Brunauer–Emmett–Teller (BET) and Barrett–Joyner–Halenda (BJH) method, respectively.

2.2.7. Electrochemical measurements

Firstly, the flexible current collector was prepared by plating polyethylene naphthalate (PEN) film with Au layer (~100 nm). For fabricating working electrodes, the ethanolic solution which contained clearly-dispersed active materials (1 mg ml⁻¹) was drop casted on the current collector (0.5 cm \times 2.0 cm) and dried in oven at 60 °C overnight. In general measurements, the mass loading of active

material was 20–30 μg . As-prepared working electrode was used with Pt wire counter electrode and Ag|AgCl reference electrode for three-electrode electrochemical analysis. All the electrochemical measurements such as cyclic voltammetry (CV), galvanostatic charge/discharge (GCD), and electrochemical impedance spectroscopy (EIS) were conducted in 1 M KOH aqueous electrolyte using Wonatech ZIVE SP2 equipped with ZMAN software. The specific capacitance (C_{sp} , F g^{-1}) and specific capacity (C_{sc} , mAh g^{-1}) of the active materials were obtained from the corresponding GCD result according to the following equation:

$$C_{\text{sp}} = \frac{I\Delta t}{m\Delta V}$$

$$C_{\text{sc}} = \frac{I\Delta t}{m}$$

I : discharge current

Δt : discharge duration

m : mass of active materials

ΔV : potential change during discharging

2.2.8. Fabrication of all-solid-state hybrid supercapacitor (HSC)

The HSC was assembled based on the various-sized CNG/Co(OH)₂ as the positive electrode and MPRGO as the negative electrode with the PVA-KOH gel electrolyte. The electrodes were prepared in the same way as that in the three-electrode system, while the gel electrolyte was obtained as follows: the mixture of PVA (1.67 g), KOH (0.84 g), and DI water (15 ml) was vigorously stirred at 85 °C until the solution clarified. Afterwards, the cooled gel electrolyte was poured onto the electrodes and left for 30 min to ensure that the electrolyte completely wetted the electrode. Finally, the all-solid-state HSC was fabricated by sandwiching two electrolyte-wetted electrodes and overnight drying process; the gel electrolyte served as both electrolyte and separator in this configuration. The energy density (E , Wh kg⁻¹) and power density (P , W kg⁻¹) of as-assembled HSC device were calculated by the following formulas given below:

$$E = \frac{I \int V(t)dt}{m}$$

$$P = \frac{E}{\Delta t}$$

I : discharge current

$\int V(t)dt$: area under the discharge curve of the device

m : total mass loading of the two electrodes

Δt : discharge time.

2.3. ZIF-67-derived Ni-Co LDH/HCS for HSC electrodes

2.3.1. Materials

Hexadecyltrimethylammonium bromide (CTAB, 99.0%), tetraethyl orthosilicate (TEOS, 98.0%), dopamine hydrochloride (DA), 2-methylimidazole (Hmim, 99.0%), cobalt nitrate hexahydrate ($\text{Co}(\text{NO}_3)_2 \cdot 6\text{H}_2\text{O}$, 98.0%), and nickel nitrate hexahydrate ($\text{Ni}(\text{NO}_3)_2 \cdot 6\text{H}_2\text{O}$, 97.0%) were purchased from Sigma-Aldrich. Ammonia aqueous solution (29.0%), sodium hydroxide (NaOH, 98.0%), sulfuric acid (H_2SO_4 , 95.0%), nitric acid (HNO_3 , 60.0%), methanol (CH_3OH , 99.5%), and ethanol ($\text{C}_2\text{H}_5\text{OH}$, 99.5%) were supplied from Samchun Chemical. All of chemicals were used without further purification. Deionized (DI) water was used in all experiment.

2.3.2. Fabrication of micro-sized HCSs

Micro-sized hollow carbon spheres (HCSs) were prepared by traditional template-mediated method using SiO_2 microspheres as the hard templates and DA as the carbon source [46]. The SiO_2

microspheres were produced by modified Stöber method according to the previous report [100]. In the typical synthesis process, CTAB (0.122 g), DI water (15.2 ml), ammonia aqueous solution (1.25 wt%, 10 ml), and ethanol (40 ml) were mixed with constant stirring. Subsequently, TEOS (4.9 ml) was slowly added to the above solution. The mixture was stirred for 3 h to obtain SiO₂ microspheres, which were calcined in air at 550 °C for 6 h to remove organic impurities on their surface. Afterwards, as-prepared SiO₂ microspheres (0.1 g) and DA (0.2 g) were stirred in tris-buffer solution (50 ml, 10 mM, pH = 8.5) for 24 h. The polydopamine (PDA)-coated SiO₂ microspheres (SiO₂@PDAs) were collected by centrifugation, then carbonized under N₂ flow at 400 °C for 2 h, which was followed by further treatment at 800 °C for 3 h. Finally, the SiO₂ cores were removed by dispersing the powders in 2.5 M NaOH aqueous solution at 80 °C for 5 h to acquire black-colored HCSs, which were washed with DI water and dried in vacuum oven before the characterization.

2.3.3. Fabrication of HCS@ZIF-67s

The hybrid structure of HCS and ZIF-67s (HCS@ZIF-67) was fabricated by secondary growth of ZIF-67s on HCS surface. Before the

growth reaction, the surfaces of as-prepared HCSs were functionalized with carboxylic groups by stirring them in the mixed acid solution (sulfuric acid/nitric acid ratio = 3:1) for 12 h at 80 °C. Afterwards, the ZIF-67 growth reaction on HCS was proceeded according to the previous report with minor modification [94]. In the typical procedure, a given amount of carboxyl-functionalized HCSs (70 or 30 mg) and $\text{Co}(\text{NO}_3)_2 \cdot 6\text{H}_2\text{O}$ (0.5 mmol) were stirred in methanol (25 ml) for 1 h. Then, Hmim (4 mmol) in methanol (5 ml) was poured into the above solution with stirring for another 1 h. After 24 h of aging, the dark violet-colored powders were obtained by centrifuging, washed with methanol several times, and dried in vacuum oven. The samples prepared from the reaction system containing 70 or 30 mg of HCSs were named HCS@ZIF-67-1 and HCS@ZIF-67-2, respectively. Besides, as the precursor material for hollow Ni-Co LDH (H-LDH), pristine ZIF-67s were also produced by applying the same method above, without the use of HCSs.

2.3.4. Fabrication of HIH-LDHs

The hybrid architecture of homogeneously distributed ZIF-67-derived H-LDHs on the HCS shell (HIH-LDH) was successfully prepared.

HIH-LDH-1, HIH-LDH-2, and H-LDH were synthesized *via* chemical etching/regrowth process which has been described elsewhere using precursor materials of HCS@ZIF-67-1, HCS@ZIF-67-2, and pristine ZIF-67, respectively [88]. For the fabrication of HIH-LDH-2, HCS@ZIF-67-2 (65 mg) was dispersed in the mixed solution of DI water (4 ml) and ethanol (16 ml), which was followed by addition of Ni(NO₃)₂·6H₂O (160 mg) with stirring for another 30 min. Subsequently, the above solution was transferred into the autoclave with Teflon liner to proceed hydrothermal treatment process, which was conducted at 90 °C for 1 h. After the process, the materials were immediately cooled to room temperature. Finally, the dark green-colored HIH-LDH-2 was acquired by centrifugation, washed with ethanol several times, and dried in vacuum oven. HIH-LDH-1 and H-LDH were fabricated through the similar method to that of HIH-LDH-2 except that HCS@ZIF-67-1 or pristine ZIF-67 was used as the precursor material, respectively.

2.3.5. Characterization

Scanning electron microscopy (SEM) images were obtained with JSM-6701F (JEOL), which was equipped with energy dispersive X-ray

spectroscopy (EDX) measuring tools. High-resolution transmission electron microscopy (HR-TEM) images were attained with JEM-3010 (JEOL). Scanning TEM (STEM) mode of Tecnai F20 (FEI) was used to analyze elemental distribution of the samples. X-ray diffraction (XRD) patterns were acquired with Cu-K α radiation ($\lambda=0.15418$ nm) using New D8 Advance (Bruker). X-ray photoelectron spectroscopy (XPS) spectra were recorded with Sigma probe (VG Scientific). Thermogravimetric analysis (TGA) curves were obtained under atmospheric condition using Pyris 6 thermogravimetric analyzer (PerkinElmer) with the heating rate of 5 °C min⁻¹. Nitrogen adsorption/desorption isotherm measurements were performed with ASAP 2010 analyzer (Micromeritics) at liquid nitrogen temperature (77 K). The surface area and pore-size distribution of the samples were acquired based on the Brunauer–Emmett–Teller (BET) and Barrett–Joyner–Halenda (BJH) theory, respectively.

2.3.6. Electrochemical measurements

The preparation method of working electrodes, the electrode system/electrolyte/measuring instrument applied, and the formulas for calculation of specific capacitance (C_{sp} , F g⁻¹) and specific capacity

(C_{sc} , mAh g⁻¹) are the same as those specified in the former part (2.2.7.).

2.3.7. Fabrication of all-solid-state hybrid supercapacitor (HSC)

The HSC was fabricated by assembling the HIIH-LDH-2-based positive electrode, the MPRGO-based negative electrode, and the PVA-KOH gel electrolyte. The manufacturing strategy of the gel electrolyte, the assembly method of the HSC device, and the calculating formulas of energy density (E , Wh kg⁻¹) and power density (P , W kg⁻¹) are identical to those demonstrated in the former part (2.2.8.).

3. Results and Discussion

3.1. ZIF-8-derived ZnO@carbon/CNF for SC electrodes

3.1.1. Fabrication process of ZPCNF

The fabrication process for ZPCNF is illustrated schematically in **Figure 10**. First, a given amount of ZIF-8 was dispersed in PVA aqueous solution to prepare the electrospinning solution. The ZIF-8 nanocrystals utilized in this study had size distributions in the range of 60–80 nm; the XRD spectra of synthesized particles exhibited only the characteristic peaks of ZIF-8, indicating that ZIF-8 was synthesized without impurities (**Figure 11**) [97]. Afterwards, the as-prepared precursor solution was electrospun to attain ZIF-8/PVA nanofibers. Finally, by the single carbonization process in N₂ atmosphere, ZIF-8/PVA nanofibers were transformed to ZPCNF without losing their unique morphologies.

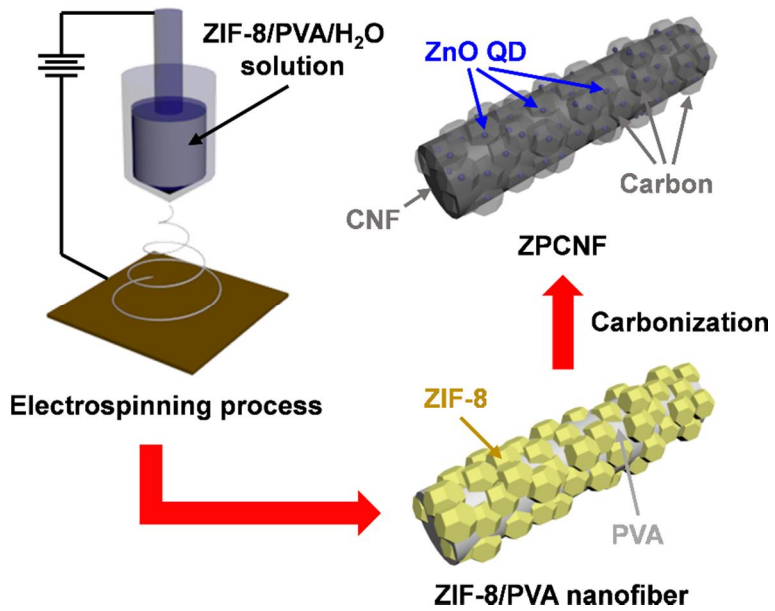


Figure 10. Schematic illustration of the ZPCNF preparation process.

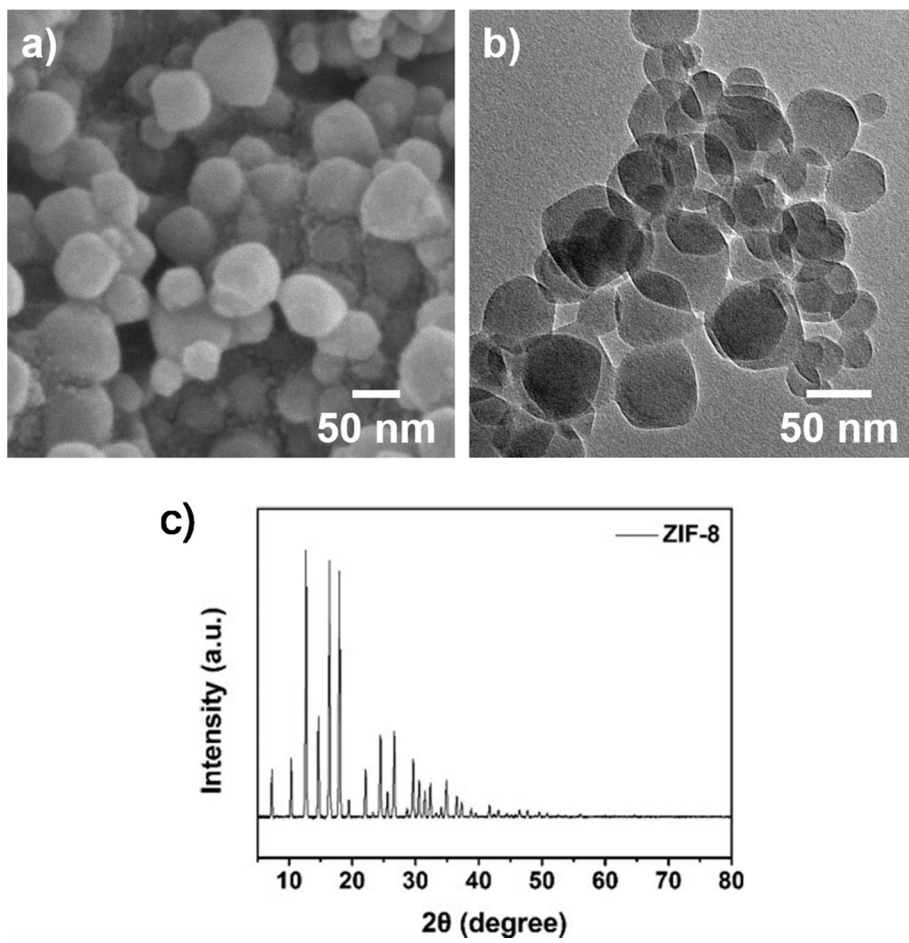


Figure 11. (a) SEM image, (b) TEM image, and (c) XRD pattern of the synthesized ZIF-8 nanocrystals.

3.1.2. Physicochemical properties of the samples

The morphologies of ZPCNF-4 were investigated by various electron microscopy techniques. Additionally, PCNF and ZPCNF-2 were examined as control samples; ZPCNF-2 and ZPCNF-4 refer to ZPCNF prepared using the electrospinning solution containing 2 or 4 wt% ZIF-8, respectively. As shown in the SEM images (**Figure 12a**, **13a**, and **14a**), all fiber samples were on the centimeter length scale with the diameter of ~250 nm. However, the interior of each sample was completely different, which was confirmed by TEM analysis. Unlike the empty interior of PCNF (**Figure 13b**), some ZnO QDs@carbons were observed in the interior of ZPCNF-2 (indicated by the arrows in **Figure 14b**). The sizes of these particles were ~60 nm, indicating that the ZnO QDs@carbons originated from the ZIF-8 nanocrystals (**Figure 14c**). In particular, ZPCNF-4 exhibited the plum-branch-like morphology, with larger amounts of ZnO QDs@carbons over the whole CNF branch compared to ZPCNF-2 (**Figure 12c**). Numerous ZnO QDs@carbons were also discernable on the surface of ZPCNF-4 in the enlarged SEM image (indicated by the arrows in **Figure 12b**). The selected-area electron diffraction (SAED) pattern of ZPCNF-4 (the inset of **Figure 12c**) demonstrated the hexagonal ZnO

wurtzite crystal structure, representing the well-dispersed state of ZnO QDs [101]. The ZnO QD distributions were further confirmed by magnified TEM (**Figure 12d**) and HR-TEM images (**Figure 12e**), indicated by yellow dashed circles. According to the TEM image, ZnO QDs (~10 nm) were uniformly dispersed, not agglomerated, and strongly adhered in the amorphous carbon matrix to construct unit ZnO QDs@carbon; these particles were attached continuously over the whole CNF as building blocks of ZPCNF-4. In the HR-TEM image, crystalline ZnO QDs were observed with the interplane distance of 0.26 nm, corresponding to the (002) plane of ZnO. Furthermore, the lattice fringe with the interplane distance of 0.34 nm was detected corresponding to the (002) plane of CNF, indicating that ZPCNF-4 consisted of CNFs, amorphous carbons, and ZnO QDs.

According to the elemental mapping images (**Figure 12f**) and XPS survey scan (**Figure 15a**), the C, O, and Zn elements were detected over the whole ZPCNF-4. Particularly, the binding energies of the Zn 2p_{3/2} and Zn 2p_{1/2} peaks were located at 1022.4 and 1045.5 eV, respectively, demonstrating the existence of ZnO in ZPCNF-4 (**Figure 15b**). Moreover, the carbon bonding configurations of ZPCNF-4 were further determined by high-resolution C 1s spectra (**Figure 15c**). The

C 1s spectra showed the intensive C–C peak, weak oxygenated carbon peaks (C–O and C=O), and the small shake-up satellite peak ($\pi-\pi^*$) of CNFs. These results implied that oxygen-rich PVA nanofibers lost most of the oxygen functional groups and simultaneously provided them to surrounding ZIF-8 during the carbonization process of ZIF-8/PVA nanofibers. For further investigation of the effect of PVA in the carbonization process of ZIF-8/PVA nanofibers, XRD patterns of ZPCNF-4, ZIF-8/PAN-C, and ZIF-8-C were obtained, as shown in **Figure 16**. The morphologies of ZIF-8/PAN-C and ZIF-8-C are shown in **Figure 17**, which were prepared by the carbonization of electrospun ZIF-8/PAN nanofibers and ZIF-8 nanocrystals, respectively. In particular, ZPCNF-4 showed both the (002) and (100) CNF diffraction peaks and the (100), (002), (101), (102), (110), (103), and (112) ZnO diffraction peaks, while PCNF exhibited only CNF peaks. This result suggests that the composites of ZnO and CNF were successfully fabricated by the carbonization of ZIF-8/PVA nanofibers. However, ZIF-8/PAN-C and ZIF-8-C did not illustrate any characteristic ZnO peaks, indicating that ZnO was not formed from ZIF-8 precursor during the carbonization of these samples. The absence of ZnO in ZIF-8/PAN-C and ZIF-8-C was because PAN and ZIF-8 did not

possess oxygen sources in their chemical structures. Based on these results, it can be deduced that PVA nanofibers play the pivotal role in the successful preparation of ZPCNF-4 by providing oxygen sources to surrounding ZIF-8s to form ZnO QDs@carbons. Meanwhile, the average size of ZnO particles in ZPCNF-4 was calculated using the Scherrer formula ($D = 0.9\lambda/(\beta\cos\theta)$, where D = crystal size, λ = wavelength of radiation used, β = diffraction line full width at half maximum of the peak profile on the 2θ scale in radians, and θ = corresponding diffraction angle) [102]. Based on the (101) ZnO diffraction peak, the measured size of the particles was approximately 10 nm. Thus, combined with the HR-TEM results, the XRD spectrum supported that the generated ZnO particles in ZPCNF-4 could be defined as QDs from their dimensions. Raman spectroscopy also verified that the ZnO in ZPCNF-4 existed as QDs with small sizes (~10 nm). As shown in **Figure 18**, the E_2 phonon frequency (433 cm^{-1}) of ZPCNF-4 was red-shifted compared with that of bulk ZnO (475 cm^{-1}) owing to the small size of ZnO particles, which strongly corroborated the formation of ZnO QDs [74]. Besides ZnO QD bands, the D, G, and D^* bands from amorphous carbons and CNFs were observed at 1347 , 1593 , and 2699 cm^{-1} , respectively, demonstrating

the coexistence of ZnO QDs, amorphous carbons, and CNFs in ZPCNF-4. The TGA measurement of ZPCNF-4 was performed up to 900 °C in air to analyze the amount of ZnO loading in the composite (**Figure 19**). Considering that the remainder after measurement was thermally stable ZnO, the ZnO loading in ZPCNF-4 was 25.1%.

The surface characteristics of PCNF, ZIF-8-C, and ZPCNF-4 were evaluated by N₂ adsorption/desorption isotherms at 77 K. Particularly, ZPCNF-4 showed the obvious type-IV hysteresis loop (**Figure 20a**) along with the pore-size distribution centered at 2.3 and 3.8 nm (**Figure 20b**), implying the presence of mesoporosity. Thus, combined with the increase in nitrogen adsorption at low pressure, ZPCNF-4 possessed the hierarchical pore system including micro- and mesopores. Owing to the hierarchical porous structure, ZPCNF-4 demonstrated the drastically increased surface area (393 m² g⁻¹) and total pore volume (0.44 cm³ g⁻¹) compared with those of PCNF (8 m² g⁻¹ and 0.0063 cm³ g⁻¹). The surface area and total pore volume of ZPCNF-4 were comparable to those of ZIF-8-C (398 m² g⁻¹ and 0.58 cm³ g⁻¹), which was only composed of MOF-derived material. Overall, unlike non-porous structure of PCNF, ZPCNF-4 had the unique porous architecture since its surface was densely covered with ZIF-8-

derived ZnO QDs@carbons, which possessed hierarchical porous structure like ZIF-8-C. The electrical conductivities of ZIF-8-C, PCNF, and ZPCNF-4 were analyzed using the four-probe method (**Figure 21**). 1D materials such as PCNF and ZPCNF-4 exhibited high conductivities since the 1D structure can offer a conductive pathway for electrons. In particular, ZPCNF-4 exhibited significantly enhanced conductivity (18.8 S cm^{-1}) *via* interconnecting ZIF-8-derived particles with 1D CNF, while ZIF-8-C demonstrated poor conductivity (3.7 S cm^{-1}) attributed to the lack of connection between the particles. Accordingly, ZPCNF-4 could take advantage of both the external hierarchical porous structure and the 1D conductive pathway for achieving high electrochemical performances.

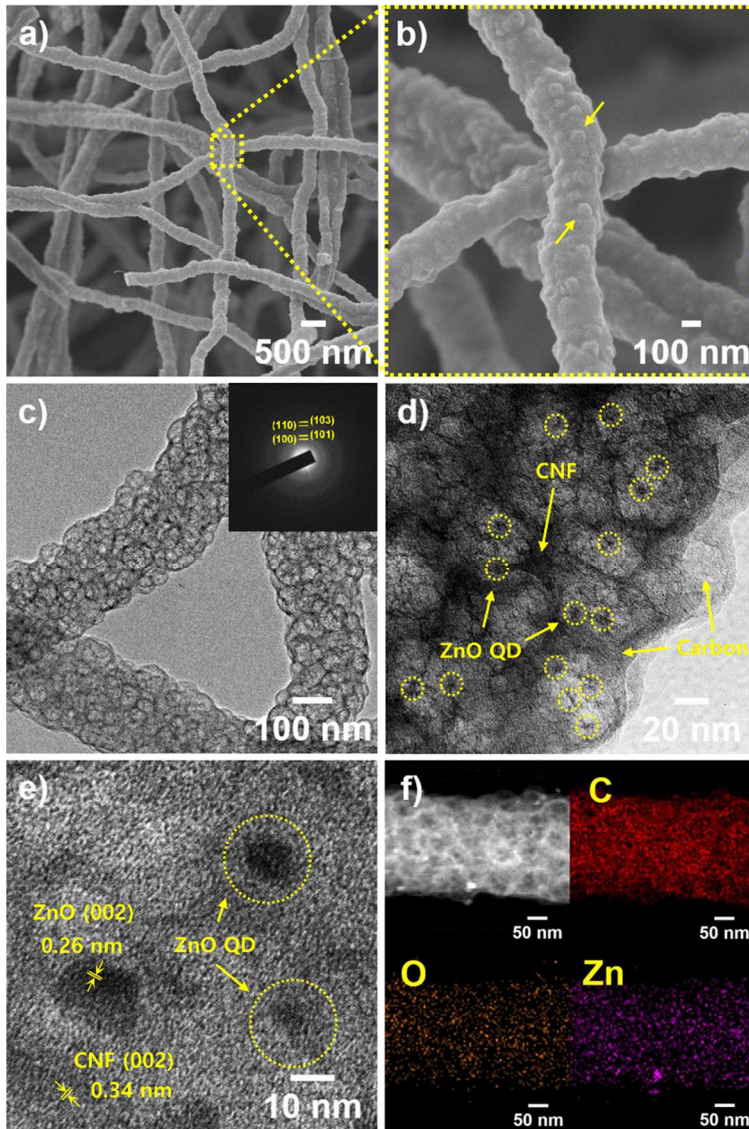


Figure 12. (a, b) SEM images, (c, d) TEM images, (e) HR-TEM image, and (f) STEM image with the corresponding elemental mapping of ZPCNF-4. The inset in (c) is the SAED pattern of ZPCNF-4.

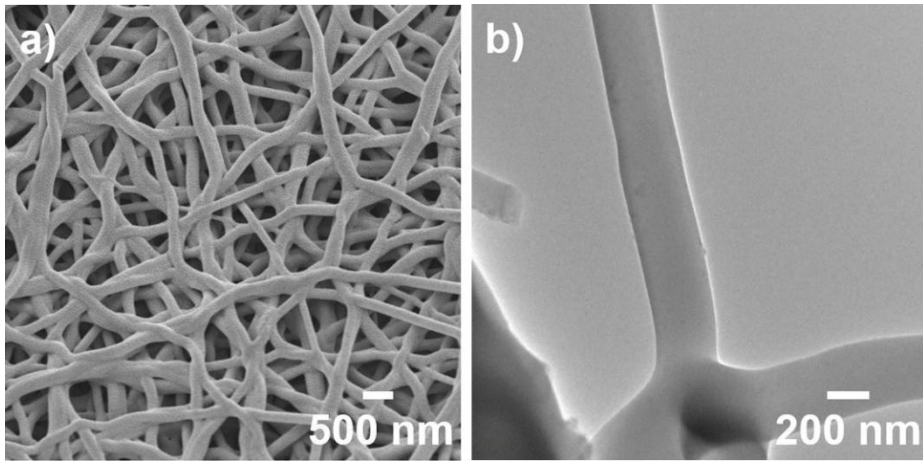


Figure 13. (a) SEM image and (b) TEM image of PCNF.

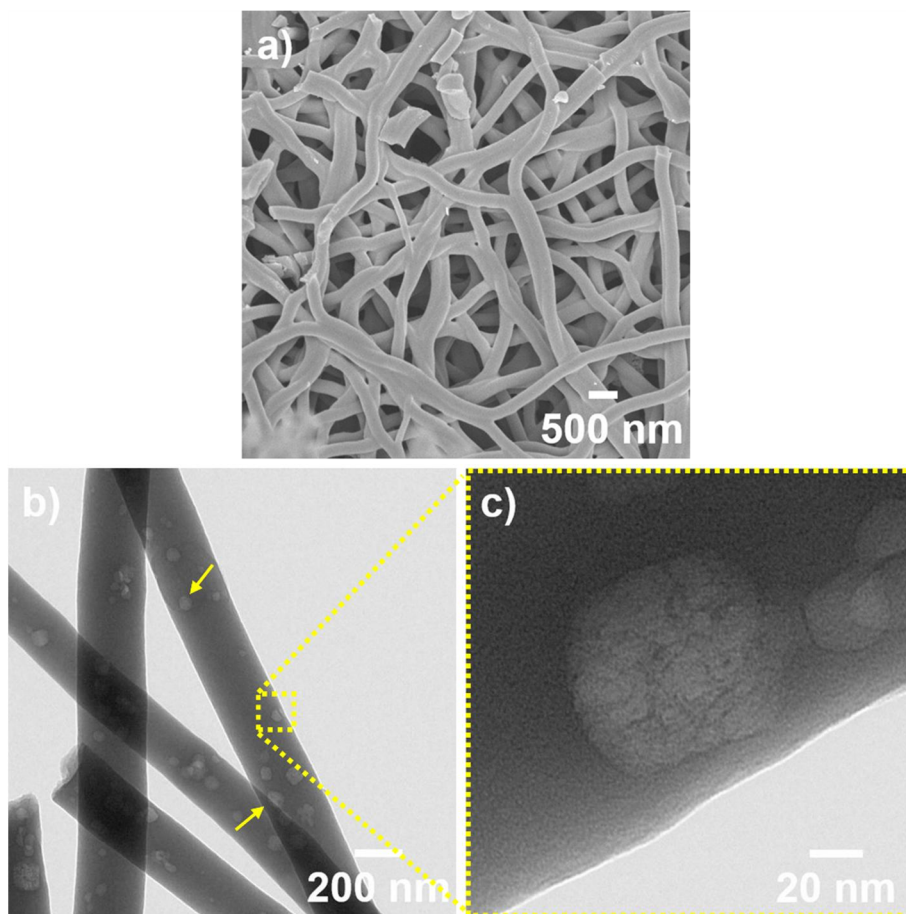


Figure 14. (a) SEM image and (b, c) TEM images of ZPCNF-2.

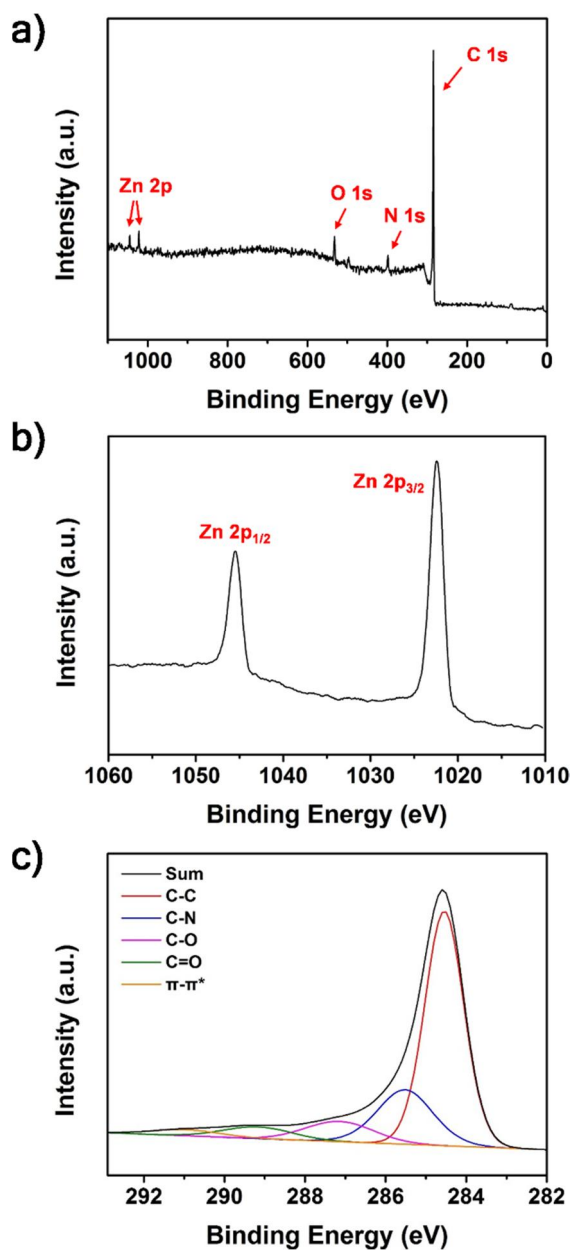


Figure 15. XPS results of ZPCNF-4: (a) survey scan and high-resolution patterns of (b) Zn 2p and (c) C 1s.

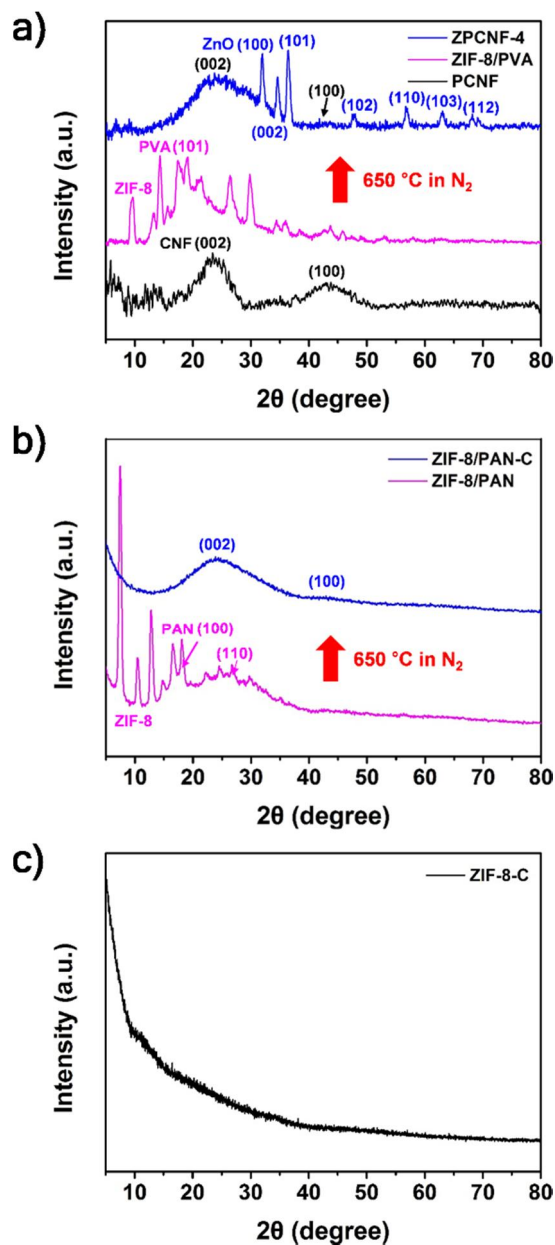


Figure 16. (a) XRD spectra of PCNF, ZIF-8/PVA fiber, ZPCNF-4. (b) XRD spectra of ZIF-8/PAN fiber and ZIF-8/PAN-C. (c) XRD spectra of ZIF-8-C.

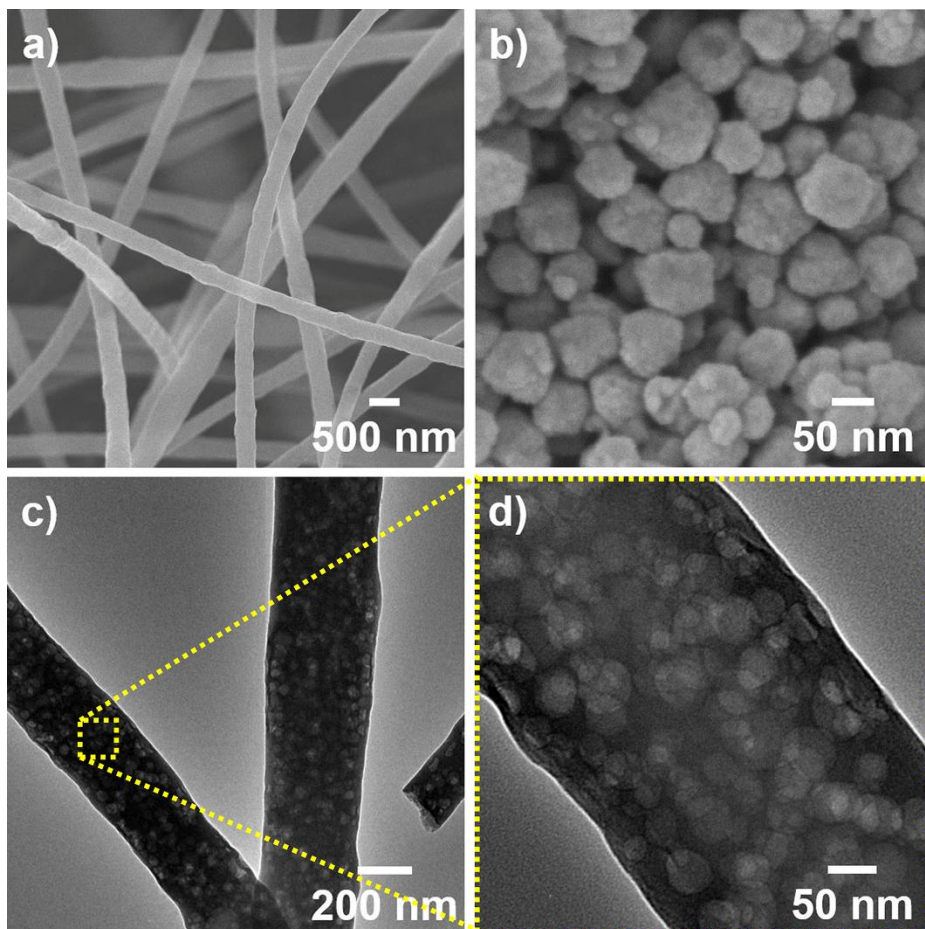


Figure 17. SEM images of (a) ZIF-8/PAN-C and (b) ZIF-8-C; (c, d) TEM images of ZIF-8/PAN-C.

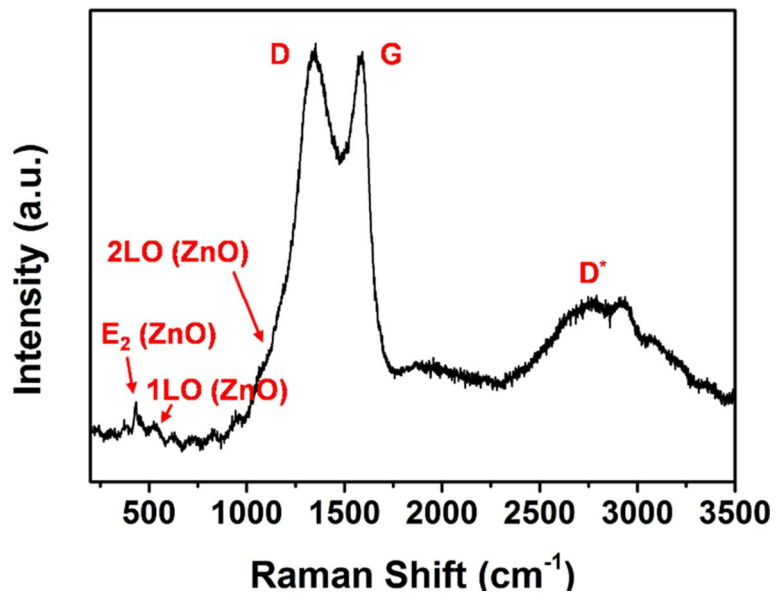


Figure 18. Raman spectrum of ZPCNF-4.

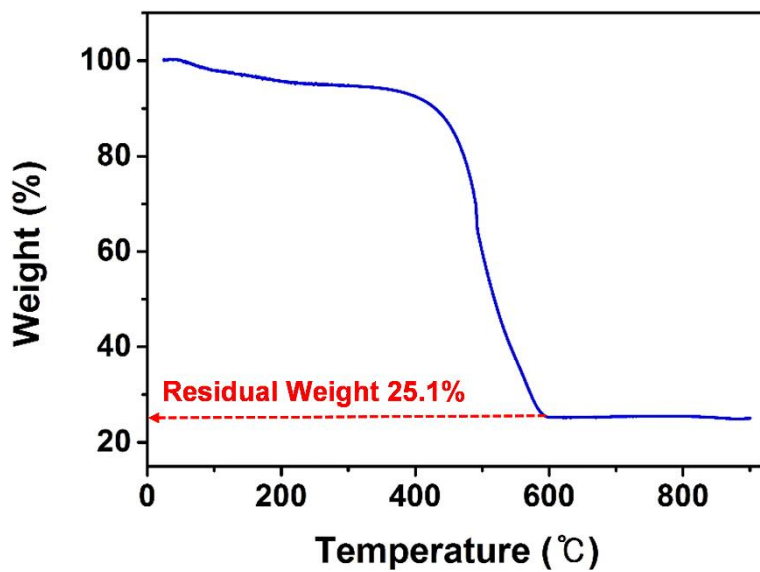


Figure 19. TGA thermogram of ZPCNF-4 at air atmosphere.

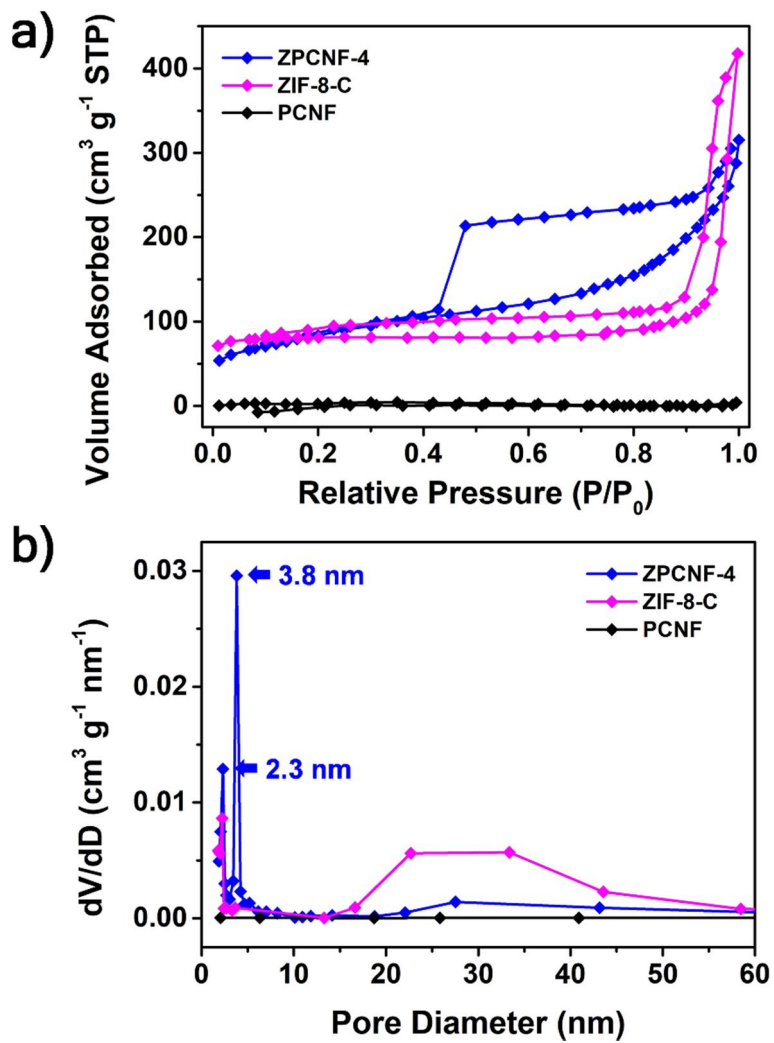


Figure 20. (a) Nitrogen adsorption/desorption plots and (b) pore-size distribution curves of PCNF, ZIF-8-C, and ZPCNF-4.

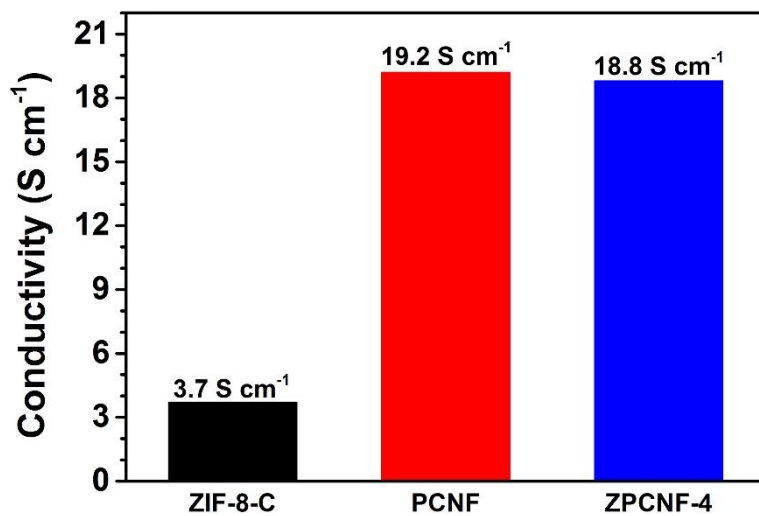


Figure 21. Electrical conductivities of ZIF-8-C, PCNF, and ZPCNF-4.

3.1.3. Electrochemical properties of the samples

To investigate the potential of ZPCNF-4 as the SC electrode material, CV, GCD, and EIS measurements were conducted. **Figure 22a** shows the CV curves of PCNF, ZPCNF-2, and ZPCNF-4 at the scan rate of 10 mV s^{-1} . ZPCNF-4 exhibited the largest CV loop area based on pseudocapacitance from ZnO QDs and electrostatic capacitance from supporting carbons. In particular, ZPCNF-4 maintained its rectangular-shaped CV curve even at high scan rates (**Figure 22b**), indicating that fast, reversible interfacial charge exchange was facilitated by the unique structural characteristics of ZPCNF-4. In addition, the GCD curves of PCNF, ZPCNF-2, and ZPCNF-4 with different current densities were obtained as shown in **Figure 23**. **Figure 24** illustrates the relationships between the specific capacitance and the current density based on the GCD results of the samples. ZPCNF-2 showed almost identical performance to that of PCNF (maximum capacitance of 111.3 F g^{-1} at 0.5 A g^{-1} and 44% capacitance retention at 8 A g^{-1}) since most of the ZnO QDs@carbons were not located on the surface but inside the ZPCNF-2 (**Figure 14**). However, ZPCNF-4 exhibited drastically enhanced capacitance (346 F g^{-1} at 0.5 A g^{-1}) with the increased rate capability (79% capacitance

retention at 8 A g⁻¹) than those of PCNF and ZPCNF-2. The outstanding electrochemical performance of ZPCNF-4 can be attributed to a couple of factors. First, numerous ZnO QDs were uniformly dispersed over the whole ZPCNF-4 without aggregation, which would effectively enhance the total capacitance by offering pseudocapacitances. Second, the 1D CNFs located along the main axis of ZPCNF-4 could act as efficient conductive pathways for electrons during the charge/discharge process. Finally, hierarchical porous surfaces provided a large ion-accessible area along with numerous electrolyte transfer channels to boost ion transportation throughout the architecture, resulting in improvements of specific capacitance and rate capability. The advances in electrochemical properties could be further confirmed from the Nyquist plots of the samples (**Figure 25**). 1D materials including ZPCNF-4 (5.5 Ω) displayed low equivalent series resistance (R_s) derived from high conductivity. In addition to low R_s , ZPCNF-4 showed the smallest charge transfer resistance (R_{ct}) (28.8 Ω) among the measured samples because the large surface area of ZPCNF-4 effectively reduced the diffusion path of electrolyte ions. Furthermore, ZPCNF-4 retained 85% of its maximum capacitance after 5000 charge/discharge cycles, demonstrating the high stability

and practical applicability of ZPCNF-4 as the SC electrode material **(Figure 26)**.

To further improve the electrochemical performance, it was attempted to prepare ZPCNF-6 using electrospinning solution containing 6 wt% ZIF-8. However, ZPCNF-6 could not be synthesized since the precursor solution containing 6 wt% ZIF-8 was difficult to be electrospun into fibers because of the over-high viscosity; the viscosity of electrospinning solution displayed increasing trend with the increase of the amounts of ZIF-8 **(Figure 27)**. In this regard, ZPCNF-4 was chosen as the optimized sample without further addition of ZIF-8.

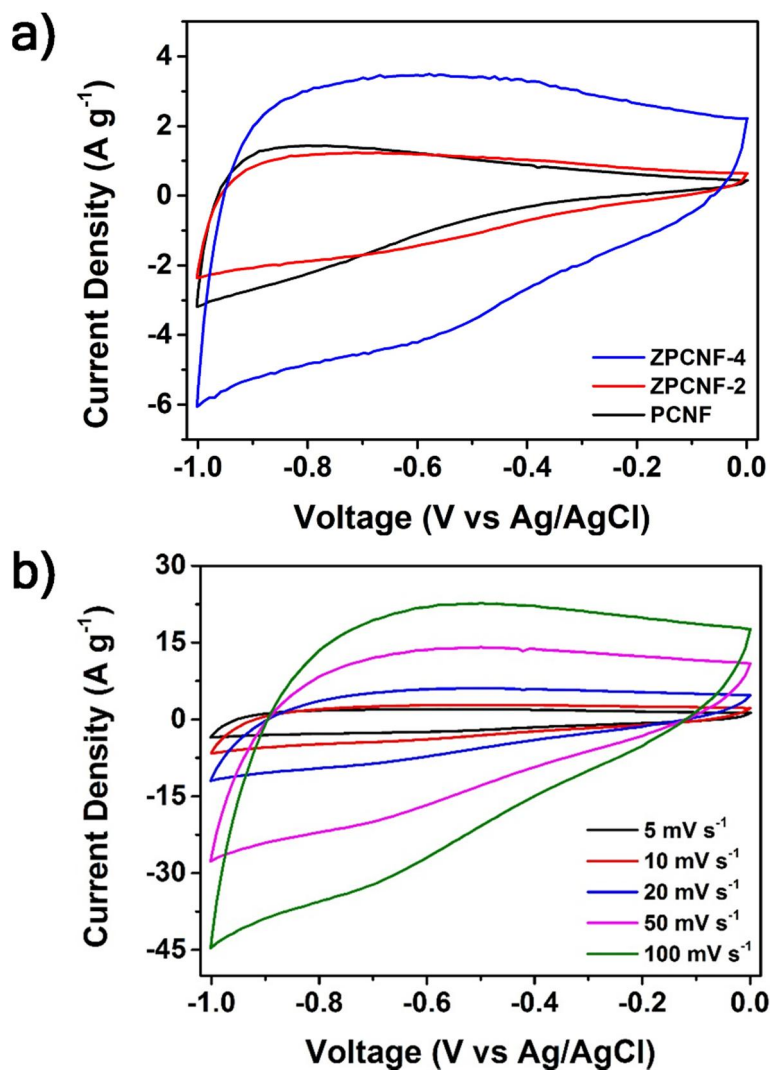


Figure 22. (a) CV curves of PCNF, ZPCNF-2, and ZPCNF-4 at the scan rate of 10 mV s^{-1} . (b) CV curves of ZPCNF-4 with different scan rates.

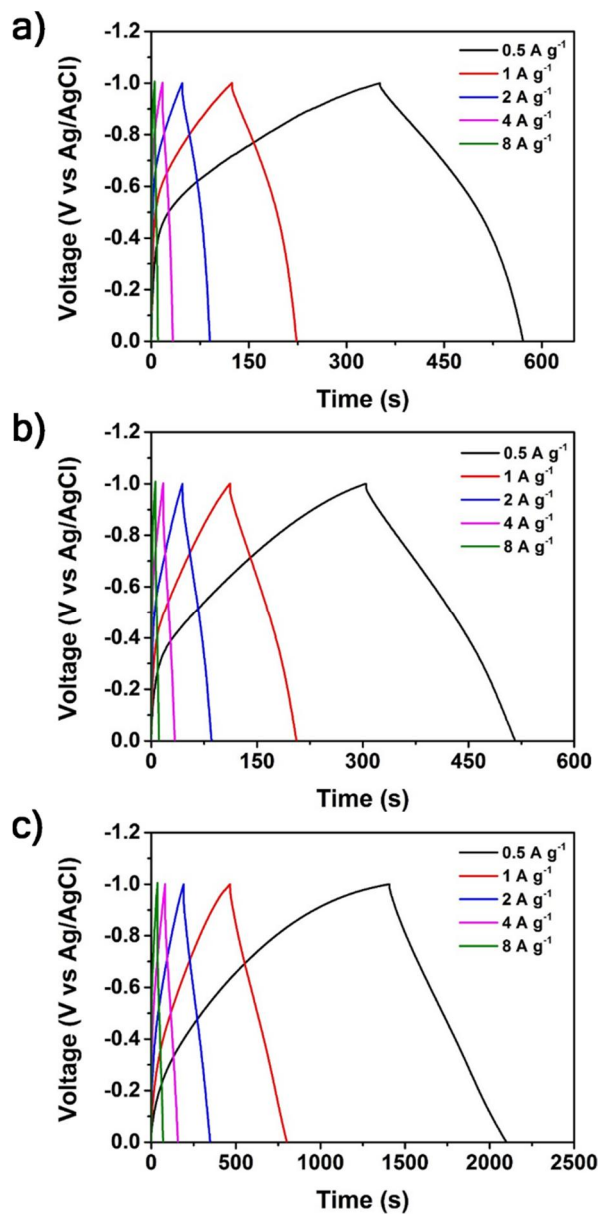


Figure 23. GCD curves of (a) PCNF, (b) ZPCNF-2, and (c) ZPCNF-4 with different current densities.

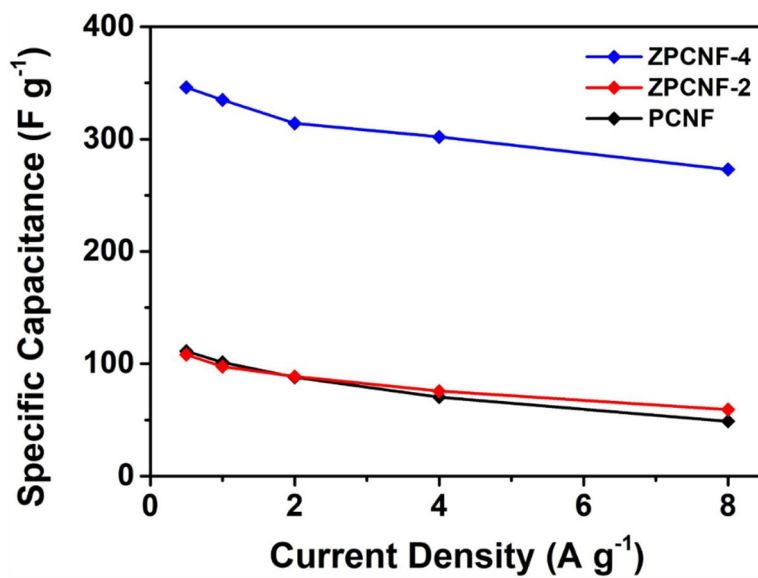


Figure 24. Specific capacitance of PCNF, ZPCNF-2, and ZPCNF-4 as a function of current density.

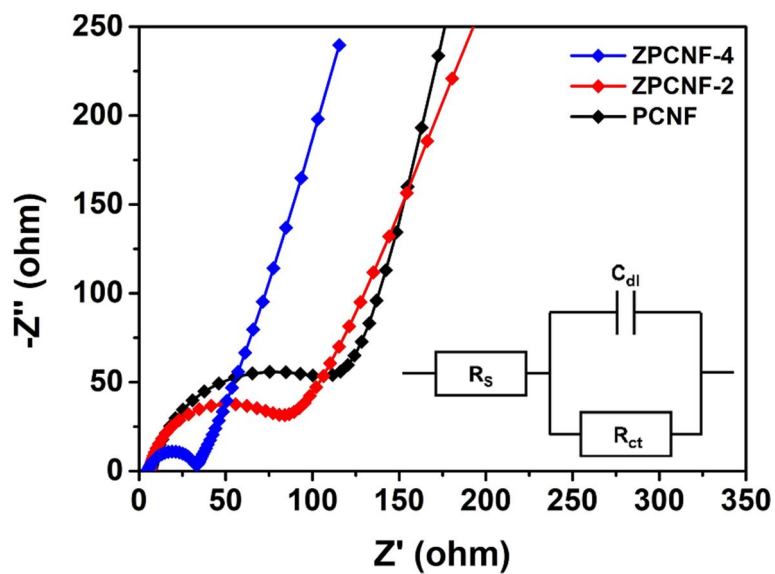


Figure 25. Nyquist plots of PCNF, ZPCNF-2, and ZPCNF-4. The inset shows the equivalent circuit diagram.

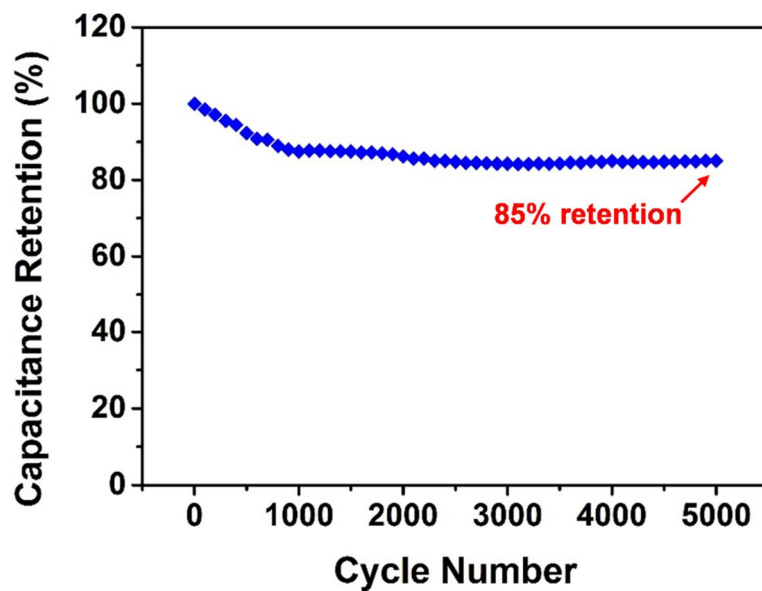


Figure 26. Cycling performance of ZPCNF-4 measured at 1 A g^{-1} for 5000 cycles.

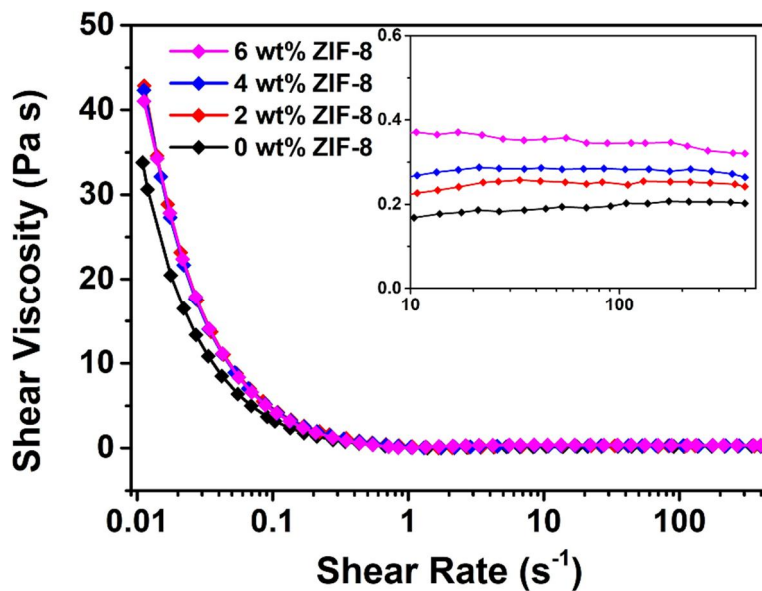
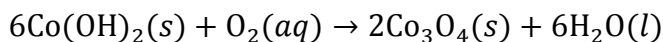


Figure 27. Shear viscosity as a function of the shear rate for electrospinning solutions containing different amounts of ZIF-8. The inset shows the magnified data in the high shear rate range.

3.2. ZIF-67-derived Co₃O₄/Co(OH)₂ for HSC electrodes

3.2.1. Fabrication process of CNG/Co(OH)₂

Figure 28 demonstrates the conversion mechanism of ZIF-67 to CNG/Co(OH)₂ through hydrothermal treatment in aqueous systems. At the early stages of the transformation process, the cobalt ions of ZIF-67 hydrolyze to produce hexagonal Co(OH)₂ plates, and the ZIF-67 crystals are etched simultaneously by the protons generated from the hydrolysis reaction [88]. Afterwards, numerous Co₃O₄ nanograins are introduced onto the surface of the Co(OH)₂ sheet by the well-known thermodynamically favorable oxidative reaction of Co(OH)₂ and dissolved oxygen, as given below [103,104]:



Particularly, the reaction system described above provided a more simple and fast route (<3 h) for fabricating the Co₃O₄/Co(OH)₂ hybrids compared with that of previously reported methods that required extra hydrolyzing agents (*e.g.*, NaOH, NH₄OH) and tedious processing times [99]. Furthermore, the size of CNG/Co(OH)₂ was controlled by employing different sizes of ZIF-67 as the precursor material. In this work, S₋, M₋, and L₋ZIF-67 were manipulated to fabricate S₋, M₋, and L₋CNG/Co(OH)₂, respectively.



Figure 28. Schematic illustration of the synthesis procedure for size-controllable CNG/Co(OH)₂ using various-sized ZIF-67 as the precursor material.

3.2.2. Physicochemical properties of the samples

The crystal structures of the samples were examined by XRD patterns (**Figure 29**). All ZIF-67 samples (S_, M_, and L_ZIF-67) exhibited only the characteristic peaks of ZIF-67, demonstrating that as-synthesized particles were phase-pure [98]. After the hydrothermal reaction, however, these peaks disappeared and diffraction peaks of brucite-like β -Co(OH)₂ and cubic spinel Co₃O₄ newly appeared for all sizes of ZIF-67 crystals [105]. In addition, all CNG/Co(OH)₂ architectures showed additional peaks around $2\theta = 11.5^\circ$ and 23.6° (marked with the asterisk), associated with (003) and (006) diffraction of the layered double hydroxide, respectively [88]. The result above indicated that the ZIF-67 crystal was successfully converted to CNG/Co(OH)₂ with layered architecture as a result of hydrothermal treatment, regardless of their sizes.

The morphologies of various-sized ZIF-67 and CNG/Co(OH)₂ were compared using SEM technique. The ZIF-67 crystals showed rhombic dodecahedral shape, and the average sizes of S_, M_, and L_ZIF-67 were 0.9, 2.4, and 4.1 μm , respectively, as shown in **Figure 30a**, **30c**, and **30e**. After the hydrothermal conversion process, however, S_, M_, and L_ZIF-67 lost their original shape, and were converted into the

hybrid structure consisted of Co_3O_4 nanograins (~ 35 nm) and $\text{Co}(\text{OH})_2$ plates of different sizes (S_- , M_- , and L_- CNG/ $\text{Co}(\text{OH})_2$). The average size of S_- , M_- , and L_- CNG/ $\text{Co}(\text{OH})_2$ was 0.8, 1.2, and 1.6 μm , respectively, as shown in **Figure 30b**, **30d**, and **30f**. In particular, unlike the pure $\text{Co}(\text{OH})_2$ plate with smooth surface (**Figure 31**), the rough surface was observed due to the presence of numerous Co_3O_4 nanograins on the surface of CNG/ $\text{Co}(\text{OH})_2$ architectures.

Meanwhile, it was also attempted to transform ZIF-67, which was smaller than S_- ZIF-67 and larger than L_- ZIF-67, to the CNG/ $\text{Co}(\text{OH})_2$ architecture *via* the hydrothermal treatment. However, the conversion process did not proceed properly if the precursor material (ZIF-67) was too small or too large. Specifically, if the size of the starting material (ZIF-67) was too small, then the CNG/ $\text{Co}(\text{OH})_2$ structure collapsed (**Figure 32**). When the ZIF-67s were too large, only the partial transformation occurred, as they could not be dispersed completely throughout the reaction system. In this regard, ZIF-67 within the specific size range (0.9–4.1 μm) was applied in this study (*i.e.*, S_- , M_- , and L_- ZIF-67).

To further investigate the morphological features of the CNG/ $\text{Co}(\text{OH})_2$ architecture, TEM and AFM images of

L_CNG/Co(OH)₂ were acquired. According to the TEM images, a large number of Co₃O₄ nanograins were distributed homogeneously over the Co(OH)₂ plate to construct a CNG/Co(OH)₂ unit (**Figure 33a**). These morphologies with rough surface were advantageous for achieving large electrochemical interfaces. In accordance with the SEM images, the size of single Co₃O₄ nanograin was confirmed to be *ca.* 35 nm, as indicated by yellow dashed circles (**Figure 33b**). The Co(OH)₂ sheets possessed the hexagonal-layered structure derived from their specific molecular arrangement, with the thickness of *ca.* 2 nm as indicated by AFM height profile analysis (**Figure 33c**) [106]. In the HR-TEM image showing the hydroxide/oxide interface of the composite (**Figure 33d**), lattice fringes of both Co(OH)₂ and Co₃O₄ were clearly evident. Specifically, lattice fringes with the interplanar distance of 0.24 nm corresponding to the (101) planes of Co(OH)₂, and lattice spacings of 0.47 nm corresponding to the (111) planes of Co₃O₄, were identified over each region [103,107]. Moreover, the coexistence of Co(OH)₂ and Co₃O₄ in the architecture was further confirmed by the SAED pattern of L_CNG/Co(OH)₂, which exhibited the diffraction rings of both materials (**Figure 33e**) [108].

The chemical composition of CNG/Co(OH)₂ architecture was analyzed by the elemental mapping mode of STEM and EDX measurements. According to the elemental mapping images (**Figure 33f**), Co and O elements were detected over the entire structure, whereas C elements were hardly observed. Given the absence of C atoms in the CNG/Co(OH)₂, the image of holey carbon grid located behind it was attained. The absence of C atoms in the CNG/Co(OH)₂ architectures was further revealed by the EDX spectra. Unlike the ZIF-67 crystals which consisted of C, N, and Co elements (**Figure 34**), the CNG/Co(OH)₂ structures mainly contained Co and O elements (**Figure 35**). These changes in chemical composition by the hydrothermal reaction implied that the ZIF-67 crystals were completely converted to CNG/Co(OH)₂ architectures without impurities. In addition, according to EDX data, as-synthesized ZIF-67s were similar in elemental composition (**Table 1**), regardless of their size, and so were the CNG/Co(OH)₂ composites (**Table 2**). This result indicated that the reaction conditions (*e.g.*, total amount of cobalt ions in the solution, reaction time, reaction temperature) for the preparation of S_, M_, and L_CNG/Co(OH)₂ were identical, although the size of ZIF-67 used in the reaction was different. Thus, all

resulting CNG/Co(OH)₂ displayed similar elemental composition, suggesting that the hybrid configurations were analogous. Meanwhile, XPS analysis was conducted on S₋, M₋, and L₋CNG/Co(OH)₂ to confirm the chemical valence state of cobalt ions therein (**Figure 36**). Regardless of their sizes, CNG/Co(OH)₂ architectures showed saturation peaks derived from the Co(OH)₂ structure, representing the existence of Co²⁺ [109]. Particularly, 2p_{3/2} peaks of CNG/Co(OH)₂ architectures appeared at lower binding energies than that of the Co²⁺ species (~781.7 eV), owing to the addition of the Co³⁺ species, which was derived from Co₃O₄ [110]. The 2p_{3/2} peaks of S₋, M₋, and L₋CNG/Co(OH)₂ were located around 779.7, 779.8, and 780.6 eV, respectively. Accordingly, XPS results further corroborated the coexistence of Co(OH)₂ and Co₃O₄ in the CNG/Co(OH)₂ architecture.

The TGA curves of S₋, M₋, and L₋CNG/Co(OH)₂ were obtained under atmospheric condition (**Figure 37**). All CNG/Co(OH)₂ architectures showed the initial weight loss at around 150 °C, followed by the second weight loss step. The initial weight loss of 2–4% was due to the removal of water, which was mostly adsorbed by interaction with the hydroxyl groups of Co(OH)₂ in hybrid architectures. Since the exposed surface of Co(OH)₂ was smaller in

S_CNG/Co(OH)₂ compared to M_ and L_CNG/Co(OH)₂, the water removal from S_CNG/Co(OH)₂ was relatively small (0.3%). Afterwards, S_, M_, and L_CNG/Co(OH)₂ demonstrated similar amounts of weight losses (~13.5%), which were attributed to the decomposition of hybrid structures into the respective compounds. Combined with the elemental composition data by EDX measurements, the results above suggested that hybrid configurations of S_, M_, and L_CNG/Co(OH)₂ were analogous.

The surface properties of S_, M_, and L_CNG/Co(OH)₂ were characterized by nitrogen adsorption/desorption isotherm measurements (**Figure 38**). The CNG/Co(OH)₂ architectures presented mesoporous characteristics; the pores of S_, M_, and L_CNG/Co(OH)₂ were mainly distributed around 2.13, 2.07, and 2.01 nm, respectively. Among these hybrid structures, L_CNG/Co(OH)₂ showed the largest BET surface area (151.6 m² g⁻¹) after S_CNG/Co(OH)₂ (106.5 m² g⁻¹) and M_CNG/Co(OH)₂ (120.2 m² g⁻¹). As the size of CNG/Co(OH)₂ architectures decreased, they became more agglomerated, resulting in the reduction of overall surface area. As shown in SEM image of S_CNG/Co(OH)₂ (**Figure 30b**), the size difference between Co(OH)₂ and Co₃O₄ was smaller in

S_CNG/Co(OH)₂ compared with that of L_CNG/Co(OH)₂. Accordingly, the role of Co(OH)₂ as the supporting backbone for Co₃O₄ was less effective in S_CNG/Co(OH)₂, resulting in agglomeration between the hybrids as if they were single Co₃O₄ materials. Interestingly, all CNG/Co(OH)₂ architectures demonstrated enhanced surface area compared with that of single Co₃O₄ (20.2 m² g⁻¹) and Co(OH)₂ (68.4 m² g⁻¹). Owing to the aggregation issues, pure Co₃O₄ and Co(OH)₂ possessed low surface area. However, in the hybrid structure of CNG/Co(OH)₂, the Co(OH)₂ sheet served as the effective supporting backbone for Co₃O₄ nanograins, resulting in alleviation of aggregation between active materials. Due to these unique morphological features of CNG/Co(OH)₂ architectures, they could offer highly enhanced electrochemical interface for charge storage process.

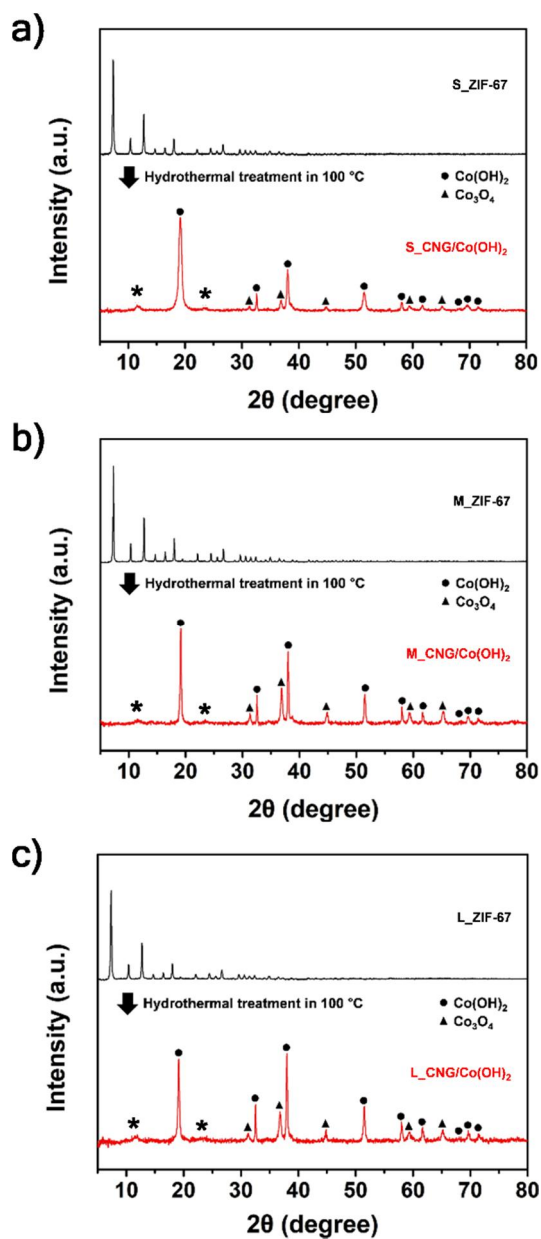


Figure 29. XRD patterns before and after the hydrothermal reaction of (a) S_ZIF-67, (b) M_ZIF-67, and (c) L_ZIF-67.

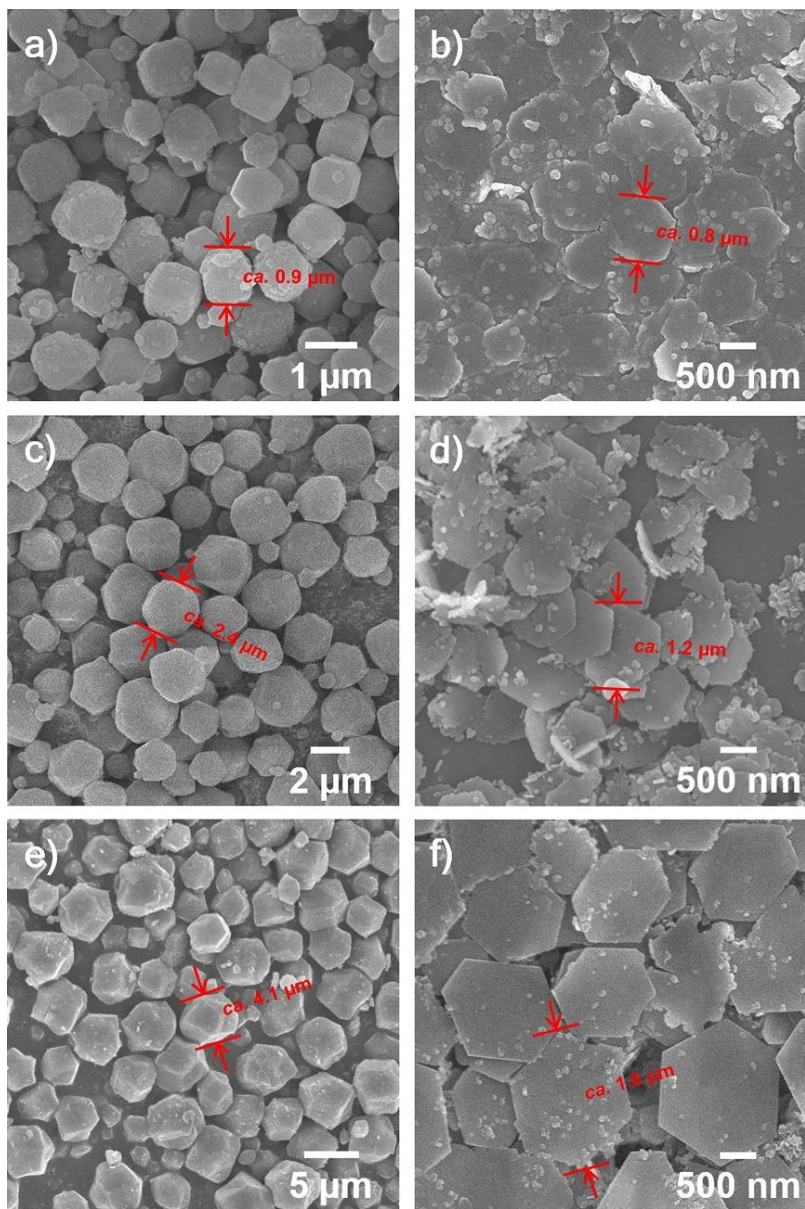


Figure 30. SEM images of (a) S_ZIF-67, (b) S_CNG/Co(OH)₂, (c) M_ZIF-67, (d) M_CNG/Co(OH)₂, (e) L_ZIF-67, and (f) L_CNG/Co(OH)₂.

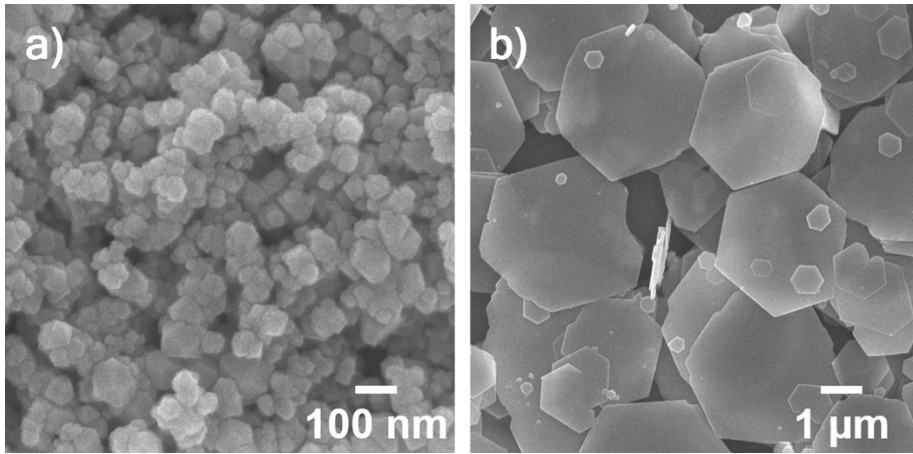


Figure 31. SEM images of (a) pure Co_3O_4 and (b) pure $\text{Co}(\text{OH})_2$.

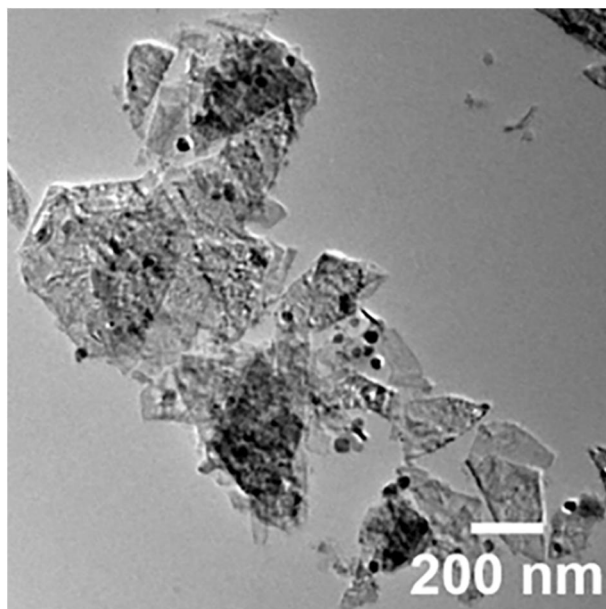


Figure 32. TEM image of CNG/Co(OH)₂ architecture obtained using 200 nm-sized ZIF-67 as the precursor material.

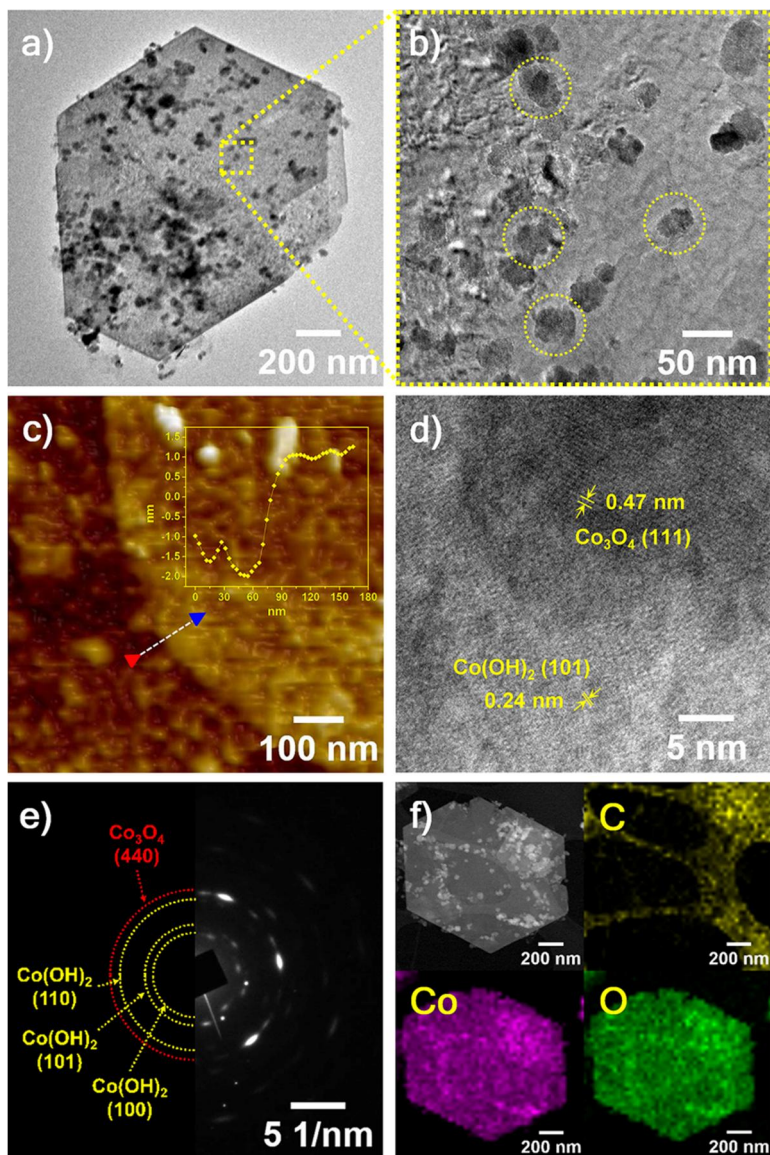


Figure 33. (a, b) TEM images, (c) AFM image (inset: height profile result), (d) HR-TEM image, (e) SAED pattern, and (f) STEM image with the corresponding elemental mapping (C, Co, and O) of L_CNG/Co(OH)₂.

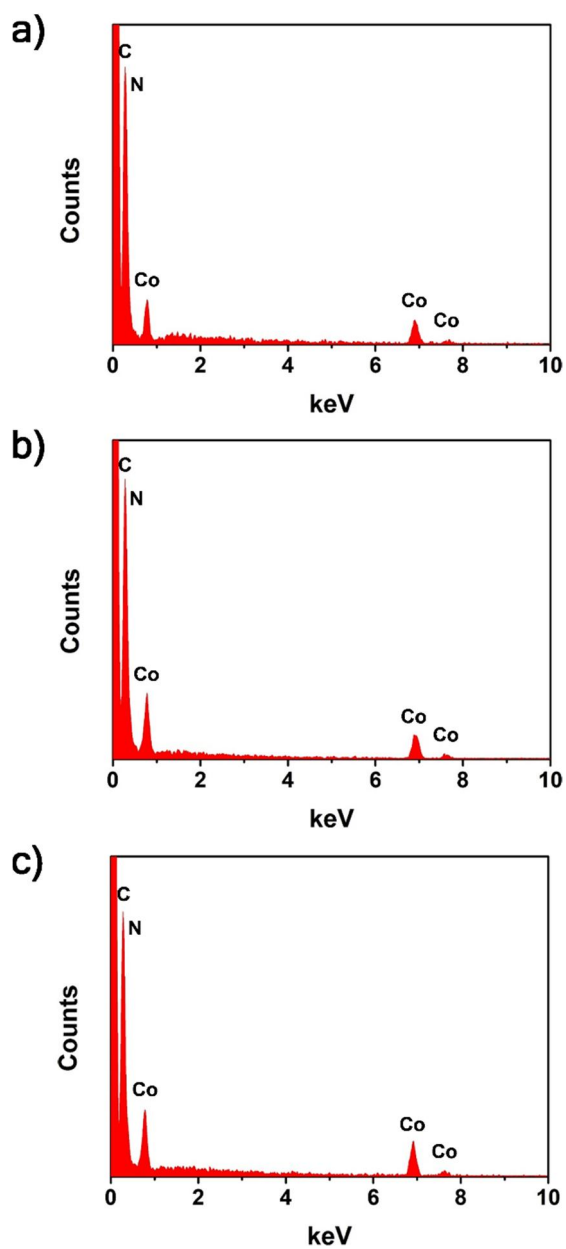


Figure 34. EDX spectra of (a) S_ZIF-67, (b) M_ZIF-67, and (c) L_ZIF-67.

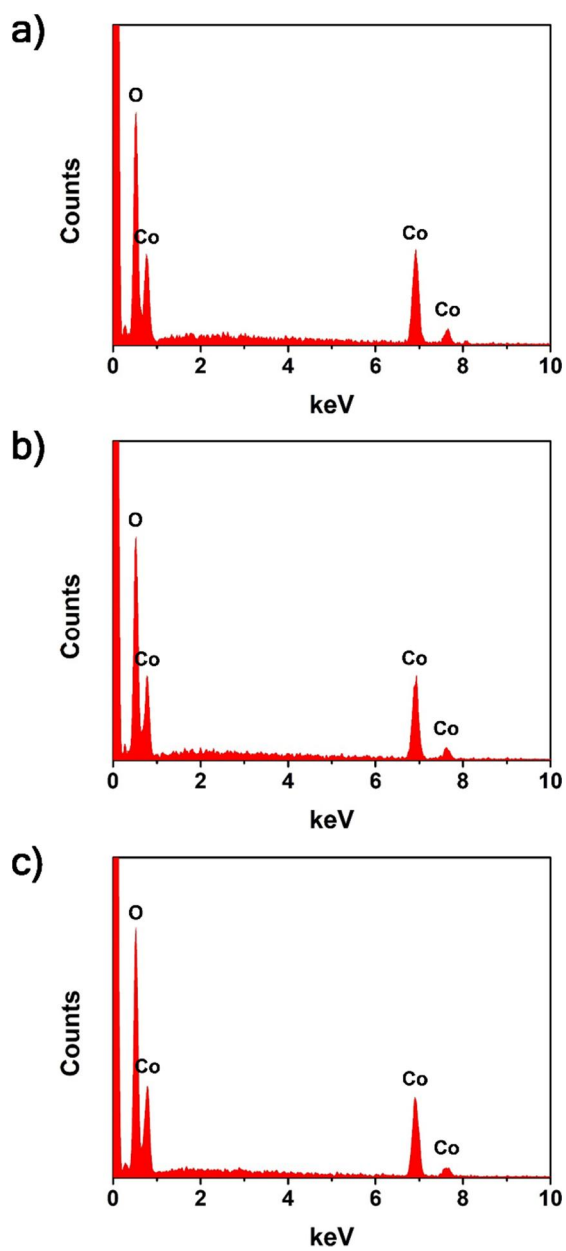


Figure 35. EDX spectra of (a) S_CNG/Co(OH)₂, (b) M_CNG/Co(OH)₂, and (c) L_CNG/Co(OH)₂.

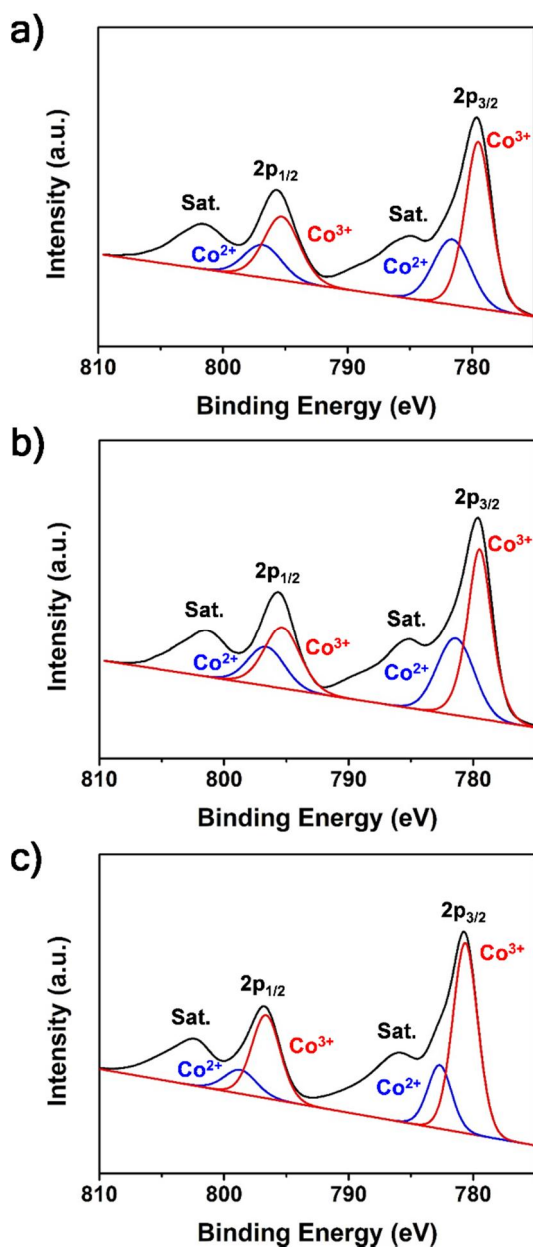


Figure 36. Co 2p XPS spectra of (a) S_CNG/Co(OH)₂, (b) M_CNG/Co(OH)₂, and (c) L_CNG/Co(OH)₂.

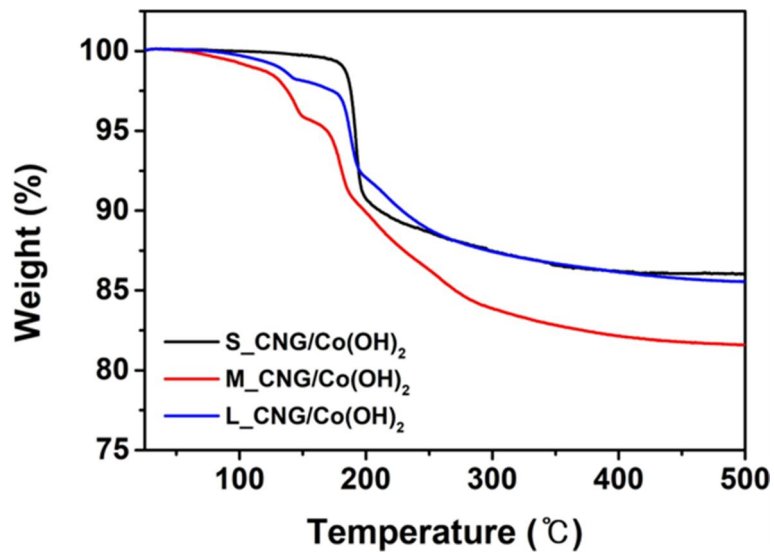


Figure 37. TGA curves of S_, M_, and L_CNG/Co(OH)₂ structures.

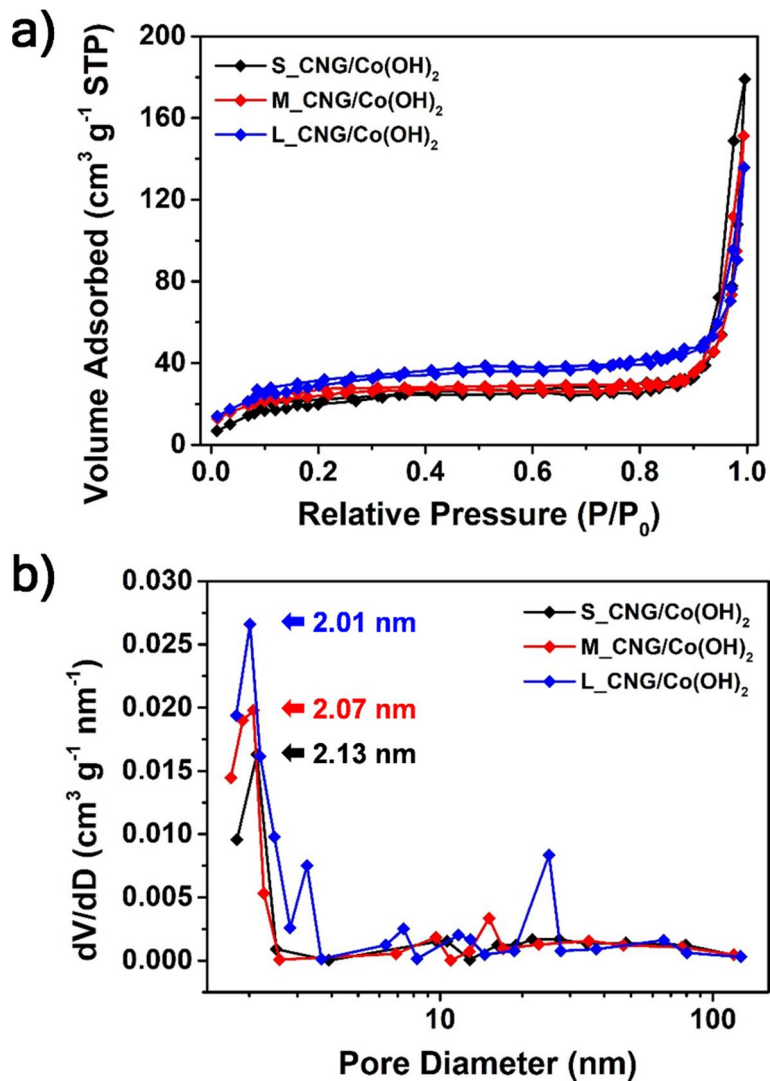


Figure 38. Nitrogen adsorption/desorption plots and (b) pore-size distribution curves of various-sized CNG/Co(OH)₂ architectures.

Table 1. Elemental composition data of various-sized ZIF-67 crystals obtained by EDX measurements.

Sample	C (At%)	N (At%)	Co (At%)
S_ZIF-67	57.7	39.6	2.7
M_ZIF-67	54.9	42.3	2.8
L_ZIF-67	58.2	37.9	3.9

Table 2. Elemental composition data of various-sized CNG/Co(OH)₂ obtained by EDX measurements.

Sample	O (At%)	Co (At%)
S_CNG/Co(OH)₂	69.1	30.9
M_CNG/Co(OH)₂	70.8	29.2
L_CNG/Co(OH)₂	73.2	26.8

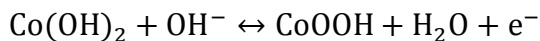
3.2.3. Electrochemical properties of the samples

The electrochemical performances of various-sized CNG/Co(OH)₂ architectures were evaluated in the 1 M KOH electrolyte with three-electrode system. Initially, the CV curves of S₋, M₋, and L₋CNG/Co(OH)₂ were obtained at different scan rates in the potential window of -0.1 to 0.4 V (vs. Ag|AgCl) (**Figure 39**). As can be seen from the shapes of these curves, all samples exhibited battery-type faradaic behavior with a couple of redox peaks, which were apparently distinct from the rectangular EDLC curve. The redox peaks of S₋, M₋, and L₋CNG/Co(OH)₂ were maintained up to the scan rate of 100 mV s⁻¹, demonstrating the fast, reversible faradaic process between the samples and the electrolyte. At the fixed scan rate of 10 mV s⁻¹, L₋CNG/Co(OH)₂ offered the larger CV loop area compared with those of S₋ and M₋CNG/Co(OH)₂, confirming the highest specific capacity of L₋CNG/Co(OH)₂ (**Figure 40**). Based on the GCD results in **Figure 41**, the specific capacities of S₋, M₋, and L₋CNG/Co(OH)₂ under various current densities were calculated and plotted as shown in **Figure 42**. Notably, L₋CNG/Co(OH)₂ exhibited the remarkable capacity of 184.9 mAh g⁻¹ at 1 A g⁻¹, which was larger than that of S₋CNG/Co(OH)₂ (113.9 mAh g⁻¹) and M₋CNG/Co(OH)₂

(128.4 mAh g⁻¹). When the current density increased to 16 A g⁻¹, the S_, M_, and L_CNG/Co(OH)₂ maintained their capacities up to 70, 74, and 76% of their maximum capacities, respectively. The high capacity values and reliable rate capabilities of CNG/Co(OH)₂ architectures originated from their unique structural characteristics (*e.g.*, rough surface, hybrid configuration), which provided enlarged electrochemical interfaces and decreased ion diffusion length. Meanwhile, the specific capacities of pure Co₃O₄ and Co(OH)₂ were also calculated from their GCD results for comparison (**Figure 43**). Compared with the CNG/Co(OH)₂ with distinctive structure, the pure Co₃O₄ (46.5 mAh g⁻¹ at 1 A g⁻¹ and 71% retention at 16 A g⁻¹) and Co(OH)₂ (31.8 mAh g⁻¹ at 1 A g⁻¹ and 70% retention at 16 A g⁻¹) demonstrated inferior performances due to their low electrochemical interfaces. To further investigate the electrochemical properties of the samples, EIS analysis was conducted in the frequency range from 10 mHz to 100 kHz (**Figure 44**). As the size of CNG/Co(OH)₂ increased, the smaller charge transfer resistance (R_{ct}) and steeper line slope were acquired, meaning that the charge transfer process was the most facilitated on the surface of L_CNG/Co(OH)₂. The R_{ct} values of S_, M_, and L_CNG/Co(OH)₂ were 15.5, 7.1, and 3.8 Ω , respectively,

which were obtained from the semicircles of the corresponding plots. The smaller R_{ct} of L_CNG/Co(OH)₂ compared with those of other CNG/Co(OH)₂ structures was ascribed to larger surface area of the L_CNG/Co(OH)₂, which provided more electrochemical interfaces for energy storage reaction. Furthermore, the cycling performances of CNG/Co(OH)₂ architectures were evaluated by 5000 cycles of charging/discharging at 4 A g⁻¹ (**Figure 45**). As a result, the specific capacities of S_, M_, and L_CNG/Co(OH)₂ were maintained up to 78, 80, and 90% of their initial capacities, respectively. Overall, the unique structural features of CNG/Co(OH)₂ effectively decreased the ion diffusion length between the electroactive materials and electrolyte to attain outstanding electrochemical performance, which was higher in the order of S_, M_, and L_CNG/Co(OH)₂. The better electrochemical performances of L_CNG/Co(OH)₂ can be attributed to a couple of factors. First, the contribution of capacity derived from Co(OH)₂ was more effective in M_ and L_CNG/Co(OH)₂ compared with that of S_CNG/Co(OH)₂. Due to the coexistence of Co(OH)₂ and Co₃O₄ in CNG/Co(OH)₂, oxidation peaks of both Co(OH)₂ and Co₃O₄ were observed at +0.06 and +0.25 V in its CV curve (denoted as (a)

and (b) in **Figure 40**), respectively, which were associated with the reactions below [81,105]:



Among them, the (a) peak area of M_ or L_CNG/Co(OH)₂ was observed to be bigger than that of S_CNG/Co(OH)₂. Based on the results above, the Co(OH)₂ in S_CNG/Co(OH)₂ was affected by the introduction of Co₃O₄ nanograins during the hydrothermal reaction. Second, the electrochemical interface was larger in the order of S_ (106.5 m² g⁻¹), M_ (120.2 m² g⁻¹), and L_CNG/Co(OH)₂ (151.6 m² g⁻¹) (**Figure 38**). Therefore, the electrochemical reaction of both Co₃O₄ and Co(OH)₂ with the electrolyte was further promoted as the size of the CNG/Co(OH)₂ architecture became larger.

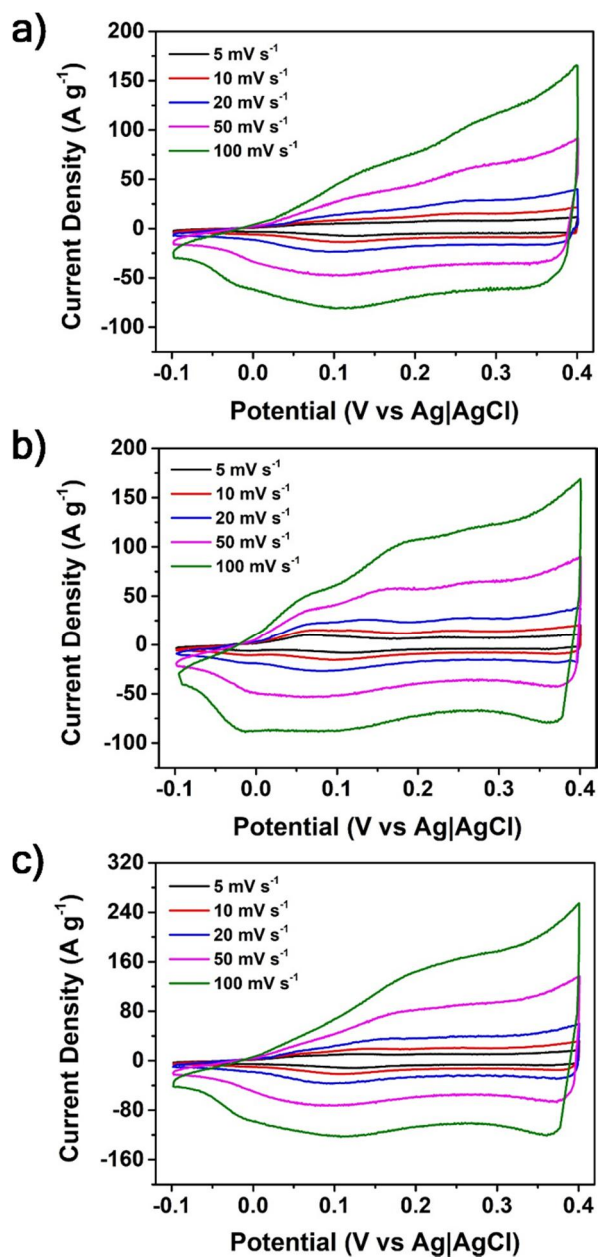


Figure 39. CV curves of (a) S_CNG/Co(OH)₂, (b) M_CNG/Co(OH)₂, and (c) L_CNG/Co(OH)₂ with different scan rates.

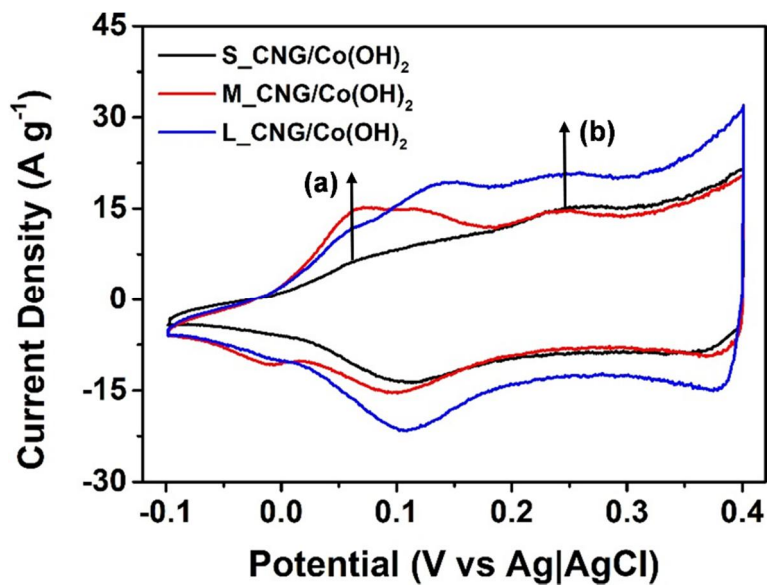


Figure 40. CV curves of S₋, M₋, and L₋CNG/Co(OH)₂ at the scan rate of 10 mV s⁻¹.

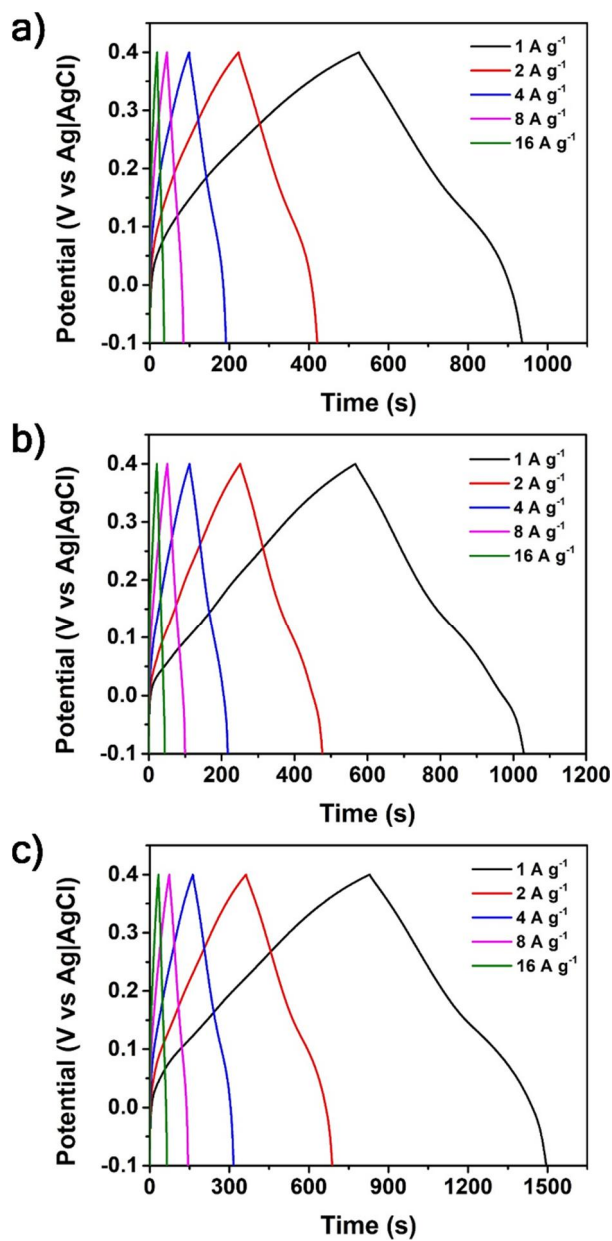


Figure 41. GCD curves of (a) S_CNG/Co(OH)₂, (b) M_CNG/Co(OH)₂, and (c) L_CNG/Co(OH)₂ with different current densities.

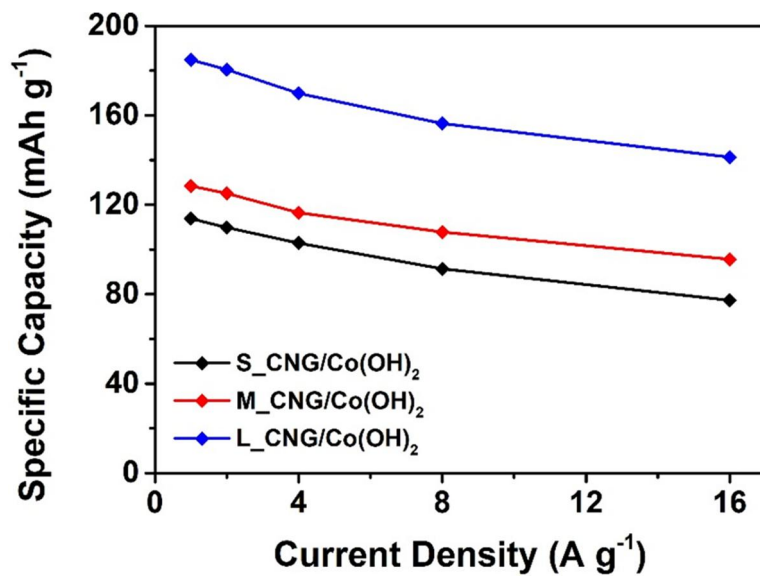


Figure 42. Specific capacity of S_, M_, and L_CNG/Co(OH)₂ as a function of current density.

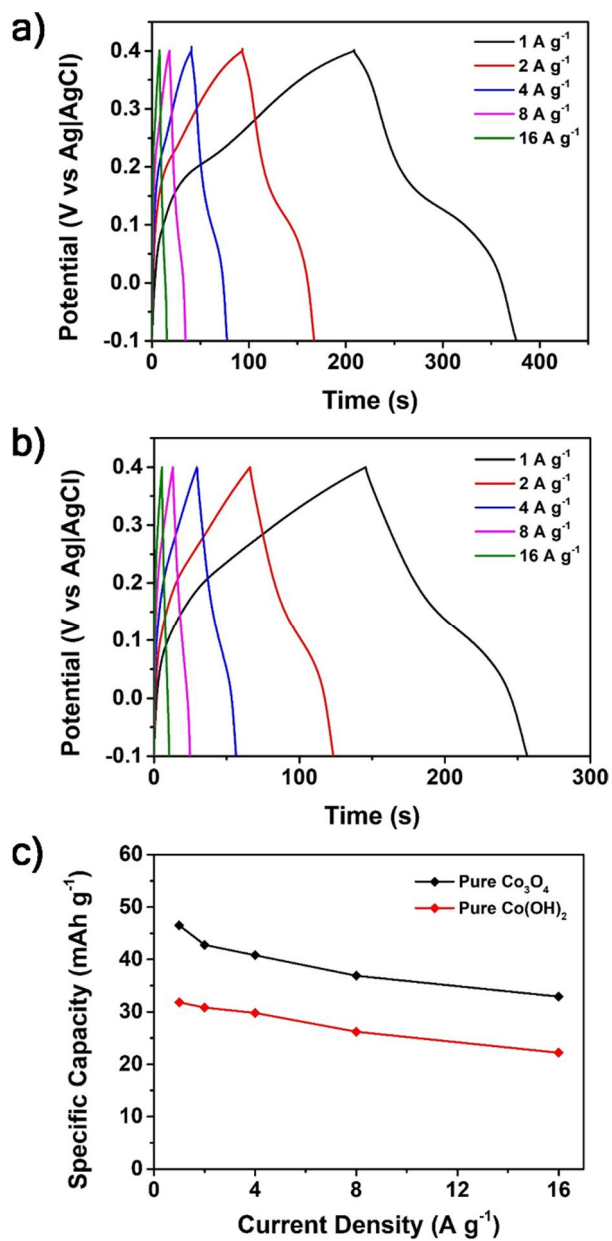


Figure 43. GCD curves of (a) pure Co_3O_4 and (b) pure $\text{Co}(\text{OH})_2$; (c) specific capacity of pure Co_3O_4 and $\text{Co}(\text{OH})_2$ as a function of current density.

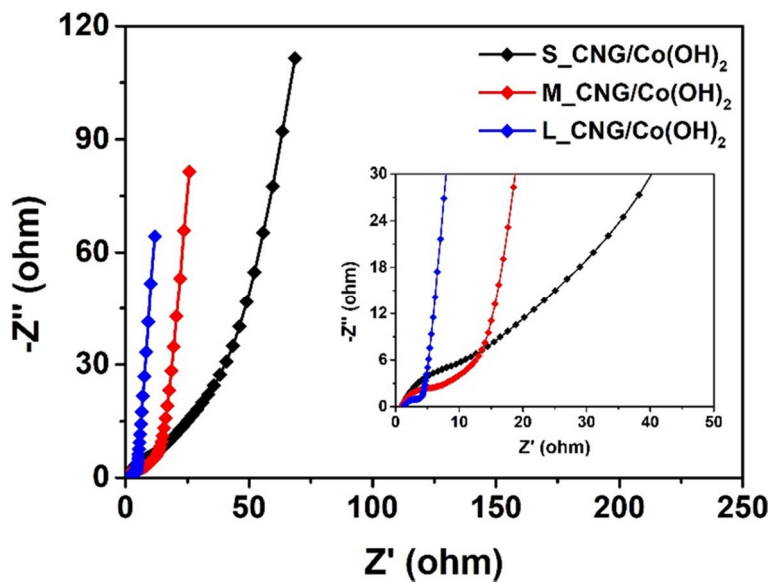


Figure 44. Nyquist plots of S₋, M₋, and L₋CNG/Co(OH)₂ in the frequency range from 10 mHz to 100 kHz. The inset shows the high-frequency region of the plots.

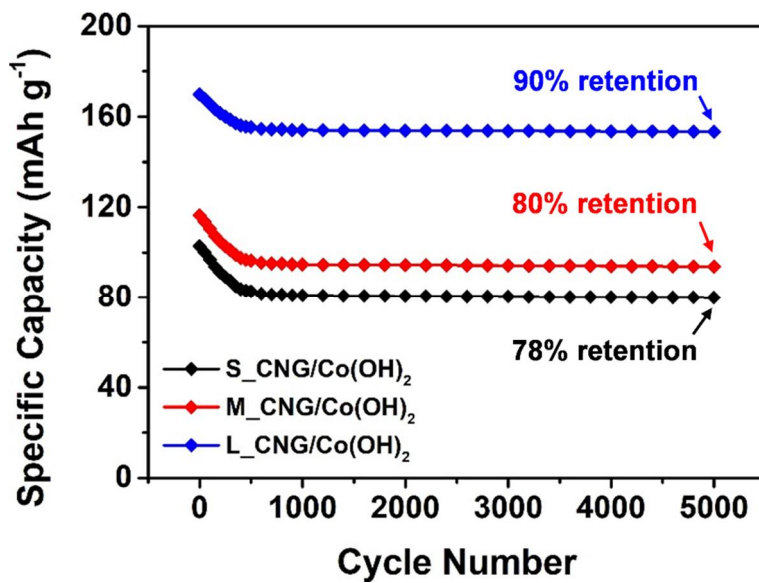


Figure 45. Cycling performances of S_, M_, and L_CNG/Co(OH)₂ measured at 4 A g⁻¹ for 5000 cycles.

3.2.4. Characterization and electrochemical properties of negative electrode material (MPRGO)

As the negative electrode material, MPRGO was prepared according to the previous work [20]. Briefly, MPRGO is the graphene material with improved surface area by minimizing restacking issues of graphene sheets through the combination of lyophilization and plasma reduction. In specific, at the first stage of MPRGO synthesis, the GO solution by modified Hummers' method was lyophilized to obtain a 3D-GO architecture [8]. Afterwards, the 3D-GO architecture was rapidly reduced (~ 2 s) to MPRGO by the plasma reduction process. By synergistic effects of both processes, several morphological features were introduced into MPRGO, which were confirmed by SEM and TEM images. First, a number of MPRGO sheets were randomly stacked to create 3D web-like structures (**Figure 46a**). Second, numerous crack-shaped mesopores, and some macropores, were discernable on the surface of MPRGO sheets, as indicated by the yellow dashed circles in **Figure 46b**. Finally, the MPRGO sheets possessed abundant wrinkles on their surface (**Figure 46c**). Owing to these morphological features, MPRGO attained the enhanced surface area, as high as $606.8 \text{ m}^2 \text{ g}^{-1}$, which was characterized by nitrogen

adsorption/desorption isotherm tests. According to the test results, in accordance with microscopy data, MPRGO exhibited mesoporosity with the type-IV hysteresis loop (**Figure 47a**) and the narrow pore-size distribution centered near 3.38 nm (**Figure 47b**). It has been reported that the mesopores play the important role in charge storage by providing suitable path for solvated ions and more reaction sites for electrochemical interactions [49]. Thus, the enlarged electrochemical interface and mesoporosity of MPRGO could promote the transportation of electrolyte ions throughout MPRGO during the charge/discharge process, resulting in enhancement of the specific capacitance and rate capability.

The electrochemical measurements of MPRGO were performed in the three-electrode cell using the 1 M KOH aqueous electrolyte. The CV curves were acquired in the potential range from -1 to 0 V (vs. Ag|AgCl) at various scan rates (20 – 500 mV s^{-1}) (**Figure 48a**). Unlike the CNG/Co(OH)₂ architectures, MPRGO showed the rectangular-shaped curve, meaning that the charge storage of MPRGO arose from EDLC. Particularly, the CV curve of MPRGO displayed no deformation even at the high scan rate of 500 mV s^{-1} , implying high rate performance. According to GCD results obtained at different

current densities (**Figure 48b**), the specific capacitances of MPRGO were calculated and plotted as a function of current density (**Figure 48c**). As a result of calculation, the maximum capacitance of MPRGO was determined to be 270 F g^{-1} at the current density of 4 A g^{-1} . Even at the current density of 64 A g^{-1} , the specific capacitance was still 212 F g^{-1} (80% retention of its highest capacitance), demonstrating the significantly high rate capability. The high specific capacitance and reliable rate performance of MPRGO can be attributed to a couple of factors. First, the large surface area of MPRGO not only provided increased ion accessible sites but also decreased the diffusion length of electrolyte ions. Second, carbon-based capacitive materials were known to render high rate capability since the electrostatic charge storage process was theoretically much faster than the faradaic reaction [43]. Considering the above discussion, it was obvious that MPRGO could be applied as the excellent negative electrode material for constructing the HSC with CNG/Co(OH)₂.

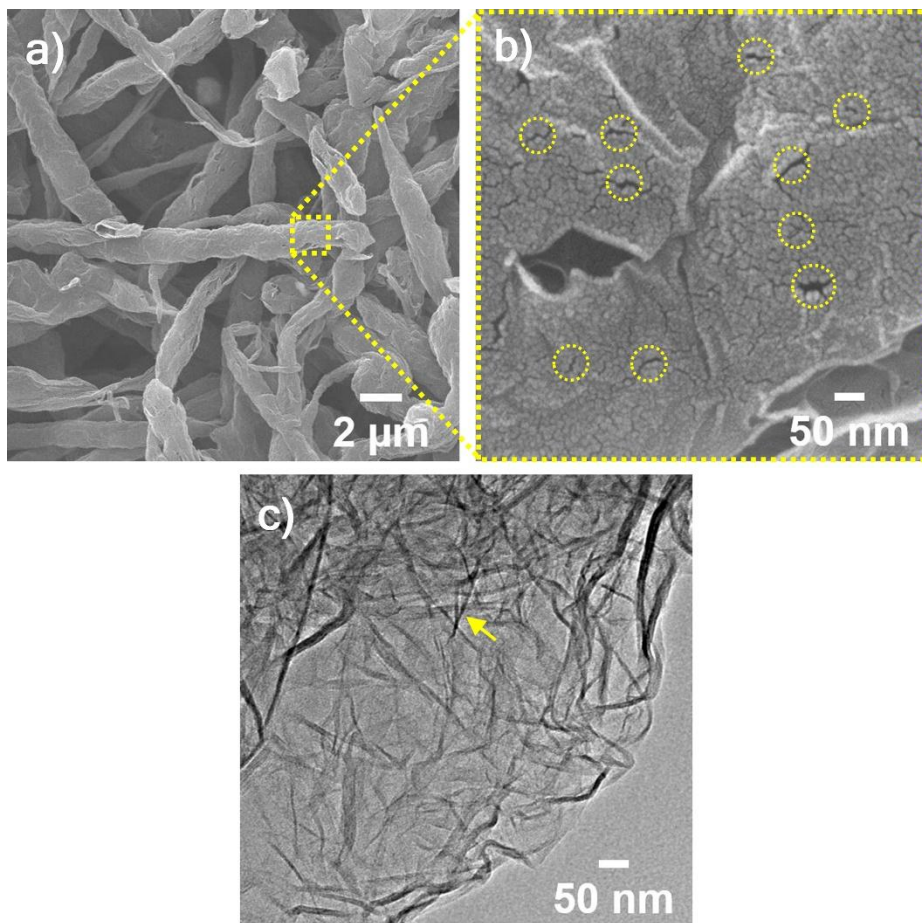


Figure 46. (a, b) SEM images and (c) TEM image of MPRGO.

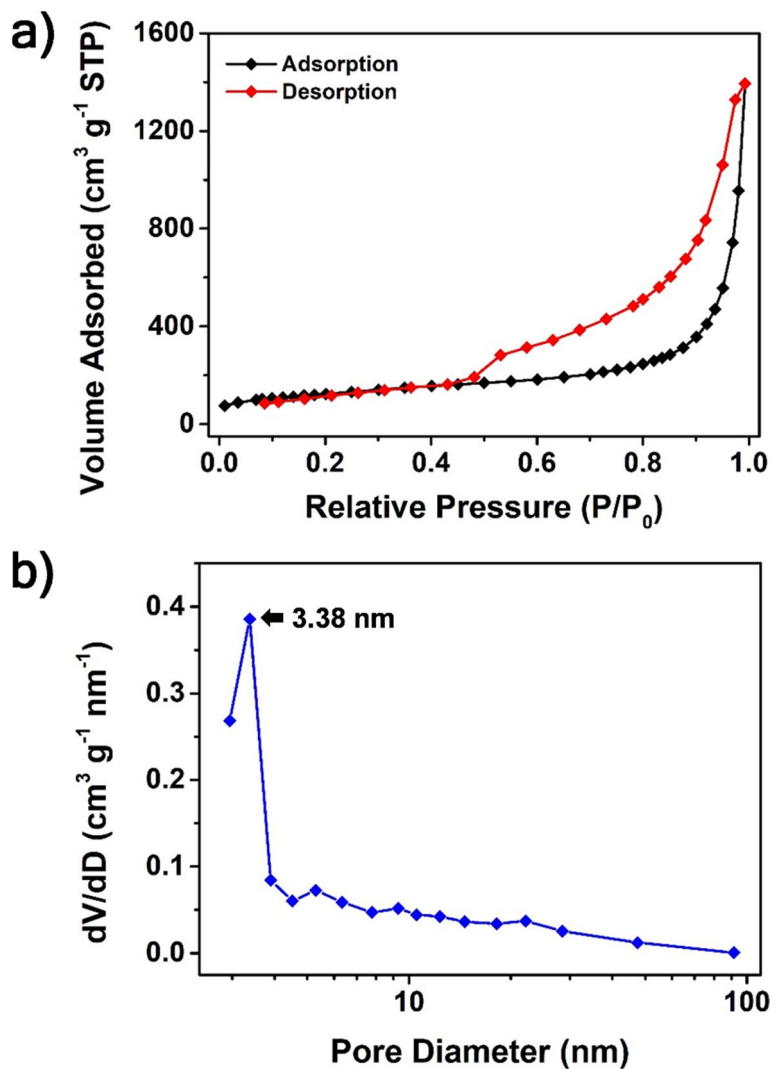


Figure 47. (a) Nitrogen adsorption/desorption plot and (b) pore-size distribution curve of MPRGO.

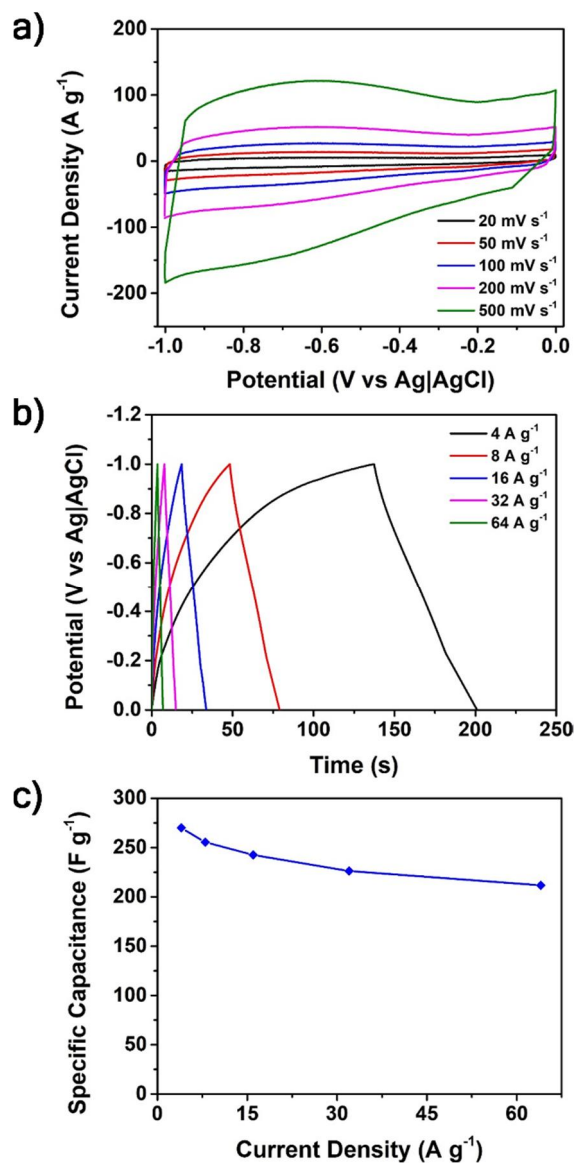


Figure 48. Electrochemical results of MPRGO: (a) CV curves with different scan rates. (b) GCD curves at different current densities. (c) Specific capacitance as a function of current density.

3.2.5. Studies of the hybrid supercapacitor (HSC)

Nowadays, multifarious HSCs are prepared to improve the energy density of SC cell [57–62]. In the HSCs, unlike symmetric SCs, two different active materials are employed in each electrode, which extends the operating voltage window of the cell. In this part, all-solid-state HSC devices were assembled using various-sized CNG/Co(OH)₂ architectures, MPRGO, and PVA-KOH gel electrolyte. **Figure 49** shows the simple structure of as-prepared HSC devices, including S_CNG/Co(OH)₂//MPRGO, M_CNG/Co(OH)₂//MPRGO, and L_CNG/Co(OH)₂//MPRGO. Particularly, the mass ratio between the positive electrode (m_+) and the negative electrode (m_-) was determined according to the charge balance theory, which was described by the following equation [58]:

$$\frac{m_+}{m_-} = \frac{C_- \times \Delta V_-}{C_+}$$

C_- : specific capacitance of negative electrode

ΔV_- : potential window of negative electrode

C_+ : specific capacity of positive electrode

Using the values obtained with three-electrode system at the current density of 4 A g⁻¹, the optimal mass ratios (m_+/m_-) for S_, M_, and L_CNG/Co(OH)₂-based HSC were calculated to be 0.850, 0.703, and

0.541, respectively. **Figure 50** shows the CV curves of as-prepared HSCs with different voltage windows, which were measured at the scan rate of 50 mV s^{-1} . Interestingly, the voltage windows of all HSCs could be extended up to 1.4 V. For all HSCs, the largest CV loop area was obtained when increasing the voltage window to 1.4 V. **Figure 51** illustrates the CV curves of as-prepared HSCs at various scan rates with the voltage window of 0–1.4 V. In particular, all CV curves showed quasi-rectangular shapes, demonstrating the capacitive behavior of as-assembled HSCs. For further investigation, the GCD curves of as-fabricated HSC devices with different current densities were acquired (**Figure 52**). At the fixed current density of 4 A g^{-1} , L_CNG/Co(OH)₂-based HSC offered the longest discharging time, implying its highest energy storage ability. The specific capacities of as-prepared HSCs at various current densities were attained using the corresponding GCD results, and plotted as shown in **Figure 53**. At 4 A g^{-1} , the specific capacity of L_CNG/Co(OH)₂//MPRGO reached 58.9 mAh g^{-1} , which was better than those of S_CNG/Co(OH)₂//MPRGO (41.0 mAh g^{-1}) and M_CNG/Co(OH)₂//MPRGO (42.9 mAh g^{-1}). In addition, it was noticeable that as-prepared HSC devices demonstrated decent rate capabilities even at high current density of 64 A g^{-1} ; the

M_ and L_CNG/Co(OH)₂//MPRGO exhibited the capacity retention of 77%. The S_CNG/Co(OH)₂-based HSC showed relatively low rate performance (48% capacity retention at 64 A g⁻¹) compared with that of other HSC devices, which was due to the high R_{ct} of S_CNG/Co(OH)₂. The high R_{ct} of S_CNG/Co(OH)₂ caused the electrode not to participate fully in the charge exchange reaction at the high current density of 64 A g⁻¹. The cycle stability of the HSC device is the important factor for practical application. Thus, the cycling tests were implemented on as-prepared HSC devices by 5000 cycles of charging/discharging at 16 A g⁻¹ (**Figure 54**). After 5000 cycles, the S_, M_, and L_CNG/Co(OH)₂//MPRGO retained 78, 82, and 91% of their original capacity, respectively, demonstrating long-term stability. Considering the results above, the combination of CNG/Co(OH)₂ architectures and MPRGO effectively improved the electrochemical performances of as-prepared HSCs.

The energy and power densities of as-prepared HSCs were calculated, and plotted in **Figure 55**, so-called Ragone plot. Notably, L_CNG/Co(OH)₂//MPRGO delivered the maximum energy density of 37.6 Wh kg⁻¹ at the power density of 2.4 kW kg⁻¹, which still remained at 33.1 Wh kg⁻¹ at the peak power density of 47 kW kg⁻¹.

Thus, these outstanding electrochemical performances of CNG/Co(OH)₂-based HSCs revealed their promising application potential.

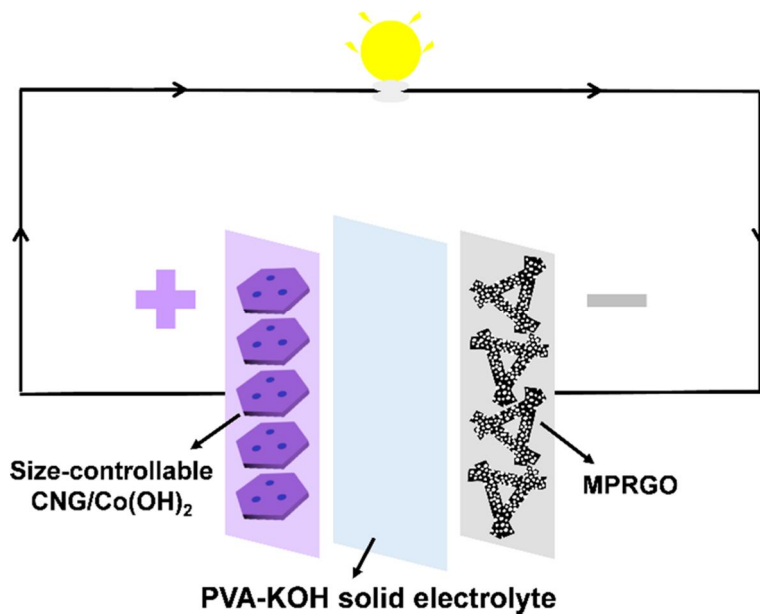


Figure 49. Schematic illustration of CNG/Co(OH)₂-based HSC devices.

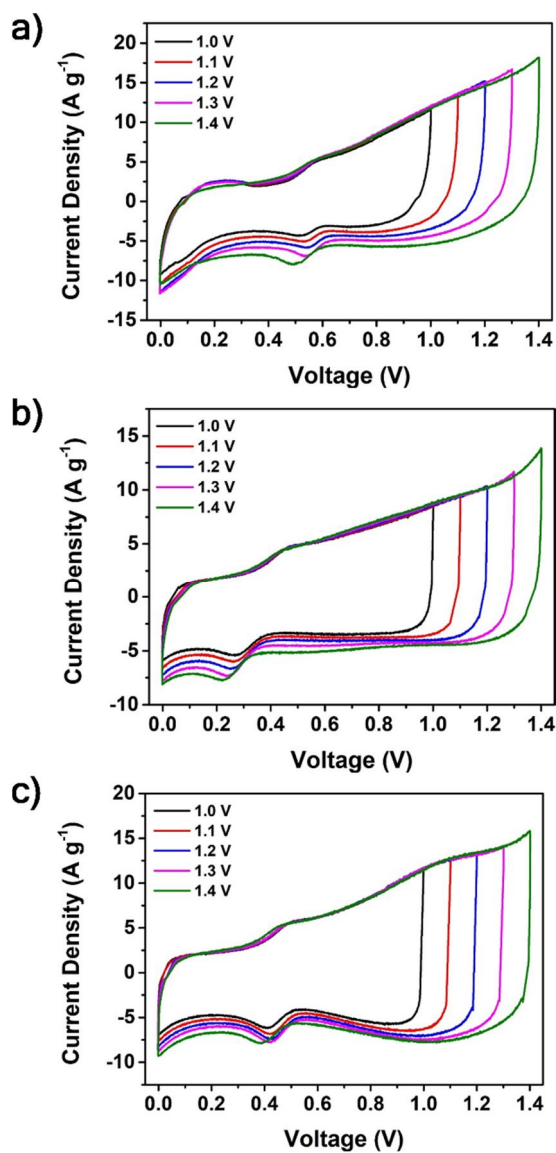


Figure 50. CV curves of as-prepared HSCs under various voltage windows, which were measured at 50 mV s^{-1} : (a) S_CNG/Co(OH)₂//MPRGO. (b) M_CNG/Co(OH)₂//MPRGO. (c) L_CNG/Co(OH)₂//MPRGO.

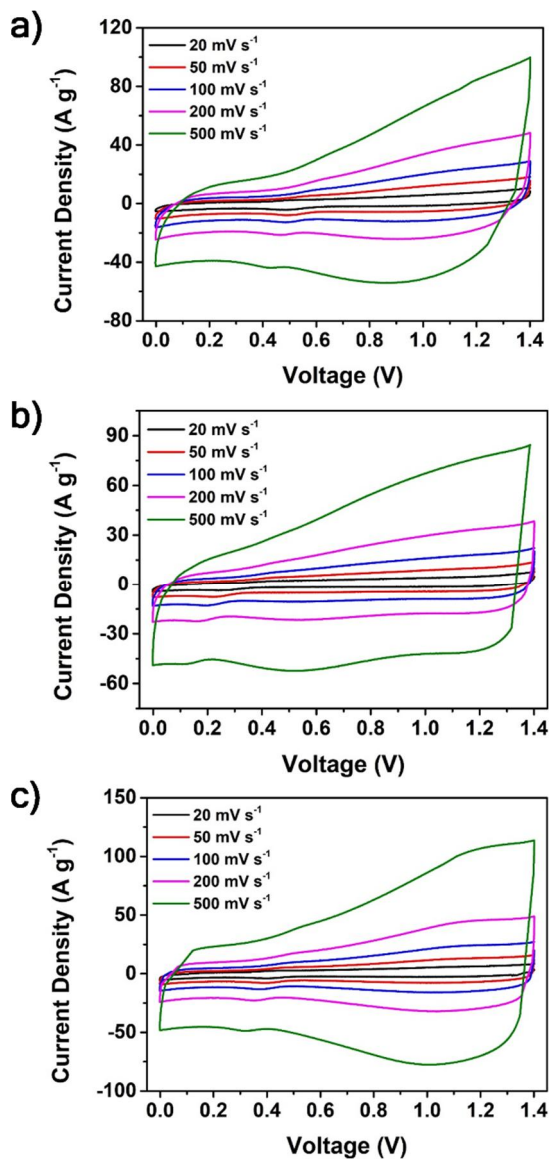


Figure 51. CV curves of (a) S_CNG/Co(OH)₂/MPRGO, (b) M_CNG/Co(OH)₂/MPRGO, and (c) L_CNG/Co(OH)₂/MPRGO with different scan rates.

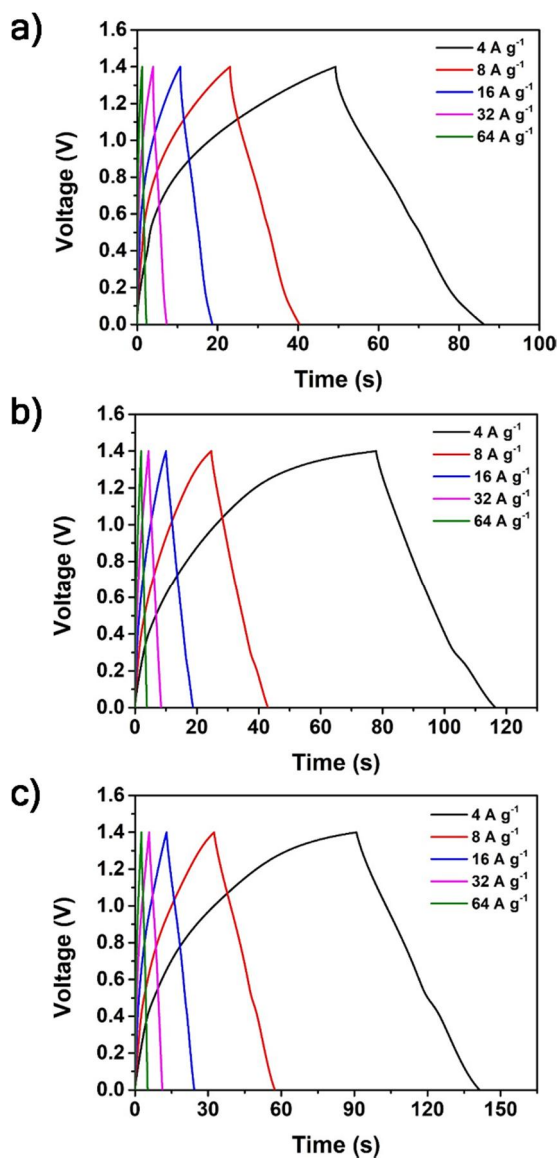


Figure 52. GCD curves of (a) S_CNG/Co(OH)₂/MPRGO, (b) M_CNG/Co(OH)₂/MPRGO, and (c) L_CNG/Co(OH)₂/MPRGO with different current densities.

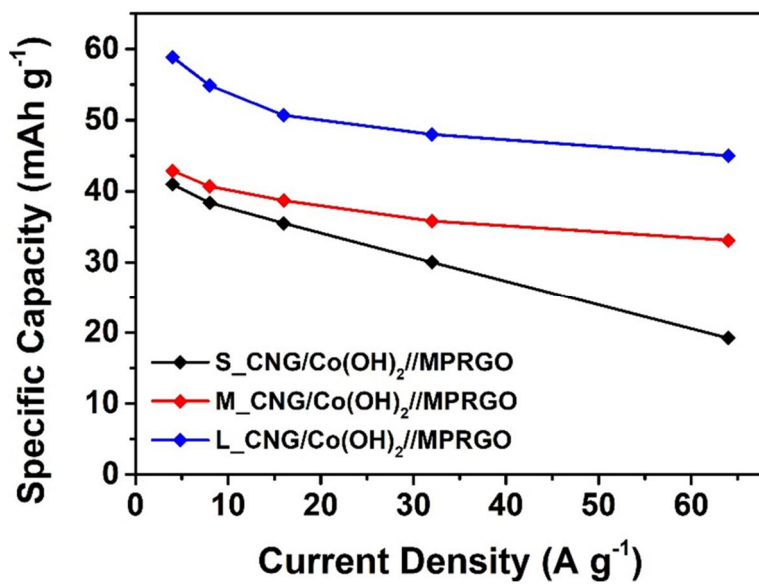


Figure 53. Specific capacity of S_, M_, and L_CNG/Co(OH)₂-based HSC as a function of current density.

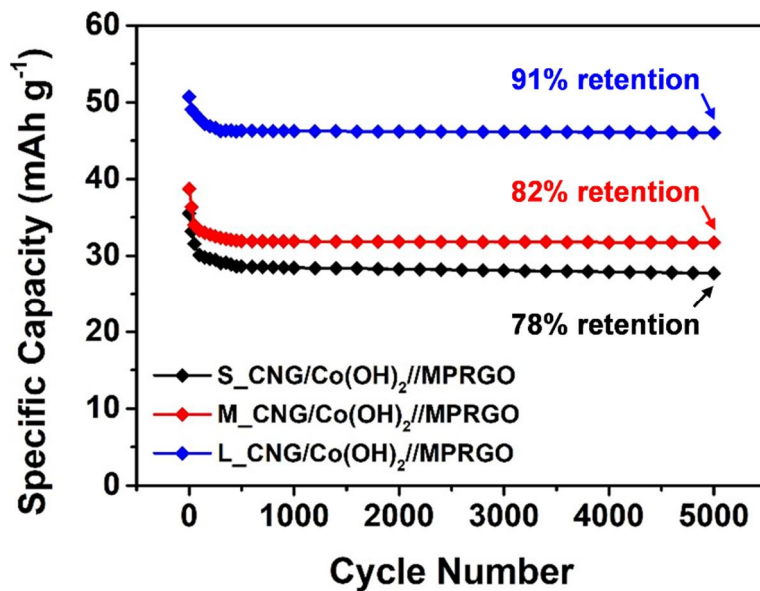


Figure 54. Cycling performances of S_, M_, and L_CNG/Co(OH)₂-based HSCs measured at 16 A g⁻¹ for 5000 cycles.

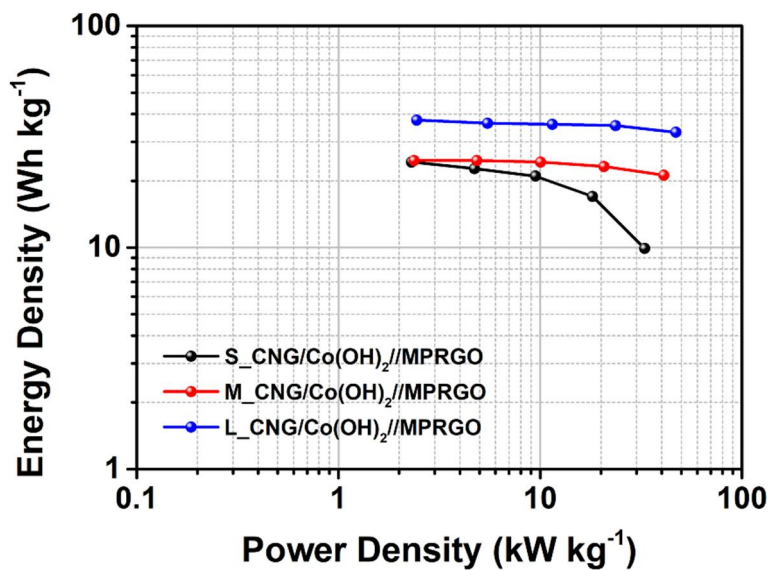


Figure 55. Ragone plots of S_, M_, and L_CNG/Co(OH)₂-based HSCs.

3.3. ZIF-67-derived Ni-Co LDH/HCS for HSC electrodes

3.3.1. Fabrication process of HIH-LDH

The synthetic strategy for HIH-LDH is schematically illustrated in **Figure 56**, which can be divided into three dominating steps. In the first step, SiO₂ microspheres obtained from modified Stöber method were employed as hard templates for preparing micro-sized HCSs [100]. After the polymer coating process by self-polymerization of DA at alkaline pH value, the resulting SiO₂@PDAs were carbonized at 800 °C and etched by NaOH solution to attain monodisperse HCSs. In the second step, HCS@ZIF-67, the precursor of HIH-LDH, was synthesized by secondary growth of ZIF-67s on the inner surface of HCS. Particularly, before the growth reaction, HCSs were functionalized with carboxylic groups to increase the affinity of their surface to ZIF materials [49]. When HCSs were not functionalized, ZIF-67s were hardly grown on the carbon shell and agglomerated with each other (**Figure 57**). The final step was converting ZIF-67s on HCS to H-LDHs by hydrothermal treatment process with Ni salts. During the process, Ni salts were hydrolyzed ($\text{Ni}^{2+} + 2\text{H}_2\text{O} = \text{Ni}(\text{OH})_2 + 2\text{H}^+$), and ZIF-67s were etched starting from their center by the protons generated from the hydrolysis reaction [88,91]. Simultaneously, the released Co

ions co-precipitated with Ni ions to form Ni-Co LDH shells, resulting in the well-defined hollow structure of H-LDH. Consequently, a novel hybrid of homogeneously distributed H-LDHs on HCS carbon shell (HH-LDH) was fabricated, demonstrating the distinctive hollow-in-hollow structure.

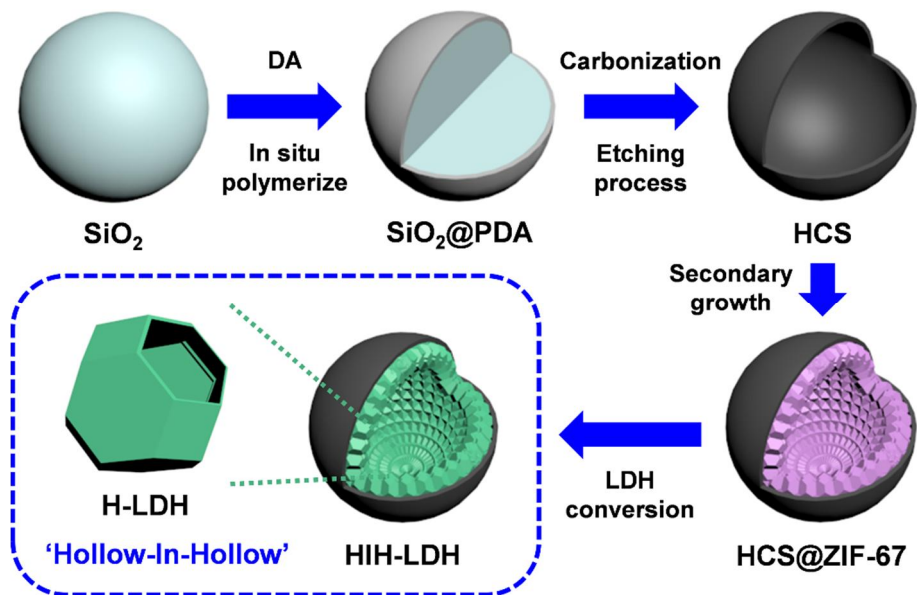


Figure 56. Schematic illustration for the fabrication process of HIH-LDH.

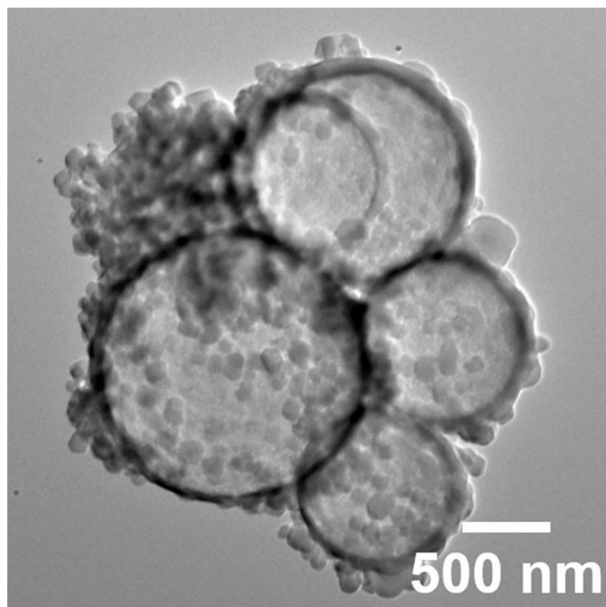


Figure 57. TEM image of HCS@ZIF-67s synthesized without introduction of carboxylic groups to HCS surfaces.

3.3.2. Physicochemical properties of the samples

Morphological features of the samples at each fabrication step were investigated by various microscopy techniques. According to the TEM images, SiO₂ microspheres showed uniform diameter (*ca.* 1.2 μm), indicating good monodispersity (**Figure 58a**). The HCSs, prepared by polymer coating, carbonization, and etching process of SiO₂ hard templates, well retained the spherical shape with the large void of 1.2 μm, which was in accordance with the size of SiO₂ used (**Figure 58b**). The shell thickness of HCS was about 50 nm, which could serve as the growth substrate for ZIF-67s, providing good mechanical strength (**Figure 58c**). As a result of growth reaction, ZIF-67s were distributed homogeneously over the HCS surface to construct a HCS@ZIF-67 unit (**Figure 59a and 59b**); The average size of as-synthesized ZIF-67s was determined to be 120 nm. In particular, HCS@ZIF-67s with different ZIF-67 content (HCS@ZIF-67-1 and HCS@ZIF-67-2) were prepared by adjusting the synthesis condition. The surface of HCS@ZIF-67-1 was not completely covered with ZIF-67s as indicated by yellow arrow in **Figure 59a**, while HCS@ZIF-67-2 exhibited sufficient amount of ZIF-67 to cover entire carbon shell (**Figure 59b**). After the hydrothermal treatment with Ni salts, HCS@ZIF-67-1 and HCS@ZIF-

67-2 were converted to HIH-LDH-1 and HIH-LDH-2, respectively. During the transformation from HCS@ZIF-67-1 to HIH-LDH-1, ZIF-67s lost their original morphology, and resulting randomly oriented Ni-Co LDH nanosheets covered the HCS surface (**Figure 59c** and **59d**). On the other hand, in the case of HIH-LDH-2, ZIF-67s in the precursor were successfully converted to H-LDHs without losing their unique structure, resulting in pomegranate-like morphology (**Figure 59e**). The inner diameter of as-formed H-LDHs was *ca.* 120 nm, which was in agreement with the size of ZIF-67s transformed, as indicated by yellow dashed circles in **Figure 59f**. The internal morphologies of the samples were further analyzed through the SEM images of the broken samples. As shown in **Figure 60a**, HCS maintained the spherical shape and hollow interior structure after the template etching process by the NaOH solution. The SEM image of HCS@ZIF-67-2 (**Figure 60b**) confirmed that the ZIF-67s were mainly grown on the inner side of the carbon shell, which densely covered the whole carbon shell. In the SEM image of HIH-LDH-2 (**Figure 60c**), the hollow particles were observed on the surface of carbon shell, as indicated by yellow dashed circles. The shell of these particles were comprised of numerous interlaced LDH nanosheets. On the other hand, the LDH nanosheets of

HIH-LDH-1 were randomly distributed on the carbon shell rather than forming the particles (**Figure 60d**). These results suggested that the hollow-in-hollow structure was successfully achieved from the synthesis condition of HIH-LDH-2, but not from that of HIH-LDH-1. Additionally, pristine ZIF-67s were synthesized and applied for preparing H-LDHs, which were examined by TEM techniques as control samples. Under the same reaction conditions, pristine ZIF-67 represented larger size (*ca.* 300 nm) than when it was synthesized as the composite form (HCS@ZIF-67) (**Figure 61a**). This phenomenon can be explained by the Co ion adsorption on the HCS surface, which limits the growth space of ZIF-67 crystals [94]. As displayed in **Figure 61b**, H-LDHs retained the unique crystal shape of pristine ZIF-67s, demonstrating the inner void size of 300 nm, which was analogous to the size of ZIF-67s transformed. **Figure 62a** illustrates the HR-TEM image of HIH-LDH-2, especially the interface between the carbon shell and Ni-Co LDHs. In the HR-TEM image, the lattice distances of 0.36 nm and 0.77 nm were observed, which corresponded to the (002) planes of HCS and the (003) planes of LDH structure, respectively. Moreover, the SAED pattern of HIH-LDH-2 showed the diffraction rings of both HCS and LDH architecture (**Figure 62b**). The SAED

pattern and HR-TEM result above corroborated the coexistence of HCS and Ni-Co LDHs in the hybrid structure of HIH-LDH-2. The elemental composition of HIH-LDH-2 was investigated by STEM and EDX measurements. According to the elemental mapping images (**Figure 63b**), C, O, Ni, and Co elements were found over the whole structure of HIH-LDH-2. Particularly, the carbon was intensely detected in the shell of architecture since it was dominantly derived from HCS. The concentration of carbon atoms in the shell was also confirmed by STEM-EDX line analysis along the indicated path (**Figure 63a** and **63c**), revealing the hollow nature of HIH-LDH-2. Based on the EDX spectrum of HIH-LDH-2 (**Figure 64**), C, O, Ni, and Co elements were identified and no Si atoms were recognized, implying that HIH-LDH-2 consisted of HCS and Ni-Co LDHs without remnant SiO₂ template in its architecture.

Figure 65a shows the variation of crystal structure at each preparation step of HIH-LDH-2, which was examined by comparing the XRD patterns of HCS, HCS@ZIF-67-2, and HIH-LDH-2. The HCS exhibited two characteristic peaks around $2\theta = 24.5^\circ$ and 44.0° , which were assigned to the (002) and (100) diffractions, respectively, indicating that the HCS only consisted of carbon shells without

remnant SiO₂ or PDA in its structure. After the ZIF-67 growth reaction, HCS@ZIF-67-2 displayed both the HCS diffraction peaks and the additional characteristic peaks of ZIF-67s, demonstrating the successfully formed composite of HCS and ZIF-67. In the XRD pattern of HIIH-LDH-2, the ZIF-67 diffraction peaks of HCS@ZIF-67-2 disappeared and newly appeared peaks were observed at around $2\theta = 11.4^\circ$, 22.7° , 34.0° , and 60.4° , which were indexed to the (003), (006), (009), and (110) diffractions of LDH structures, respectively. This result suggested that the ZIF-67s of HCS@ZIF-67-2 were completely converted to Ni-Co LDHs with preservation of HCS crystal structure as a result of the transformation process. The XRD results of H-LDH, HIIH-LDH-1, and HIIH-LDH-2 were also compared in **Figure 65b**. All samples represented LDH diffraction peaks as their dominant crystal structures. Particularly, unlike the pattern of H-LDH, the (002) diffraction of HCS was detected in the HIIH-LDH-1 and HIIH-LDH-2, meaning that they were composed of Ni-Co LDHs and their supporting carbon shells. Meanwhile, the (003) diffraction peak of LDH was recognized as different intensity for each sample, implying that the proportion of Ni-Co LDH in architecture was higher in the order of HIIH-LDH-1, HIIH-LDH-2, and H-LDH. The TGA curves of H-LDH,

HIH-LDH-1, and HIH-LDH-2 were obtained under atmospheric condition (**Figure 66**). As the temperature increased up to 800 °C, three steps of weight losses were observed for all samples, which were appeared in the approximate temperature range of 25–240, 240–300, and 300–800 °C. The initial weight losses of the samples were due to the stripping of physically adsorbed water. These amounts were higher in the order of H-LDH (10.9%), HIH-LDH-1 (14.4%), and HIH-LDH-2 (17.2%), implying the difference in the surface area of the samples in the same order. The second weight losses were attributed to the decomposition of the Ni-Co LDHs into the respective compounds, which was the highest in the H-LDH because it contained the largest amount of Ni-Co LDHs in its structure. The weight losses observed above 300 °C were owing to the decomposition of carbon species. In this step, compared with the small loss (8.6%) of H-LDH derived from residual ligands, HIH-LDH-1 (48.6%) and HIH-LDH-2 (29.7%) showed significant weight losses because they included additional HCS in their hybrid architectures. Judging from this result, the proportion of Ni-Co LDHs in the hybrid structure of HIH-LDH-1 and HIH-LDH-2 was estimated to be 51.4 and 70.3%, respectively.

The elemental valence states of H-LDH and HIH-LDH-2 were

investigated by XPS analysis. In the high-resolution C 1s spectra (**Figure 67a**), the C–C peak of HIIH-LDH-2 exhibited much higher intensity than that of H-LDH, which was owing to the addition of HCSs. Besides, the intensity of O–C=O peak was relatively high in HIIH-LDH-2 since the carbon shell of the composite was functionalized with carboxylic groups during the synthesis procedure of HIIH-LDH-2. As shown in **Figure 67b**, the Ni 2p spectra of H-LDH and HIIH-LDH-2 were fitted well with two obvious satellite peaks and two spin-orbit doublets ($2p_{1/2}$ and $2p_{3/2}$), which were assigned to the state of Ni^{2+} [111]. In the spectra of Co 2p (**Figure 67c**), the low intensities of satellite peaks were observed, suggesting the coexistence of Co^{2+} and Co^{3+} in the samples [112]. As a result of Co 2p deconvolution, the spin-orbits of H-LDH and HIIH-LDH-2 could be split into two peaks, which were corresponding to the Co^{2+} and Co^{3+} , respectively. Thus, the elemental valence states of H-LDH and HIIH-LDH-2 were confirmed to be consistent with the previously reported Ni-Co LDH-based materials [111–113].

The surface properties of H-LDH, HIIH-LDH-1, and HIIH-LDH-2 were evaluated using nitrogen adsorption/desorption isotherm measurements. As shown in **Figure 68a**, all samples presented type-IV hysteresis

curves, indicating the presence of mesoporosity. According to the pore-size distribution data (**Figure 68b**), the pores of H-LDH, HIIH-LDH-1, and HIIH-LDH-2 were mainly distributed around 3.20, 3.17, and 3.07 nm, respectively, which further confirmed the mesoporosity of the samples. These mesopores were commonly derived from slit-shaped pores generated by the interlaced Ni-Co LDH nanosheets [94]. Meanwhile, HIIH-LDH-2 ($304.3 \text{ m}^2 \text{ g}^{-1}$) showed highly enhanced surface area compared with that of H-LDH ($223.0 \text{ m}^2 \text{ g}^{-1}$) because Ni-Co LDHs had less agglomeration when they were in the hybrid form with HCS than single material. In the hybrid structure of HIIH-LDH-2, the carbon shell served as the effective supporting backbone for Ni-Co LDHs, resulting in alleviation of aggregation between the electroactive materials. Although HIIH-LDH-1 was also present in the hybrid form, it did not exhibit much increased surface area ($235.7 \text{ m}^2 \text{ g}^{-1}$) since its Ni-Co LDHs lost their unique hollow structure and randomly oriented. Overall, abundant mesopores, enlarged surface area, and formation of hollow-in-hollow structure of HIIH-LDH-2 could provide much advantage during the charge storage reaction.

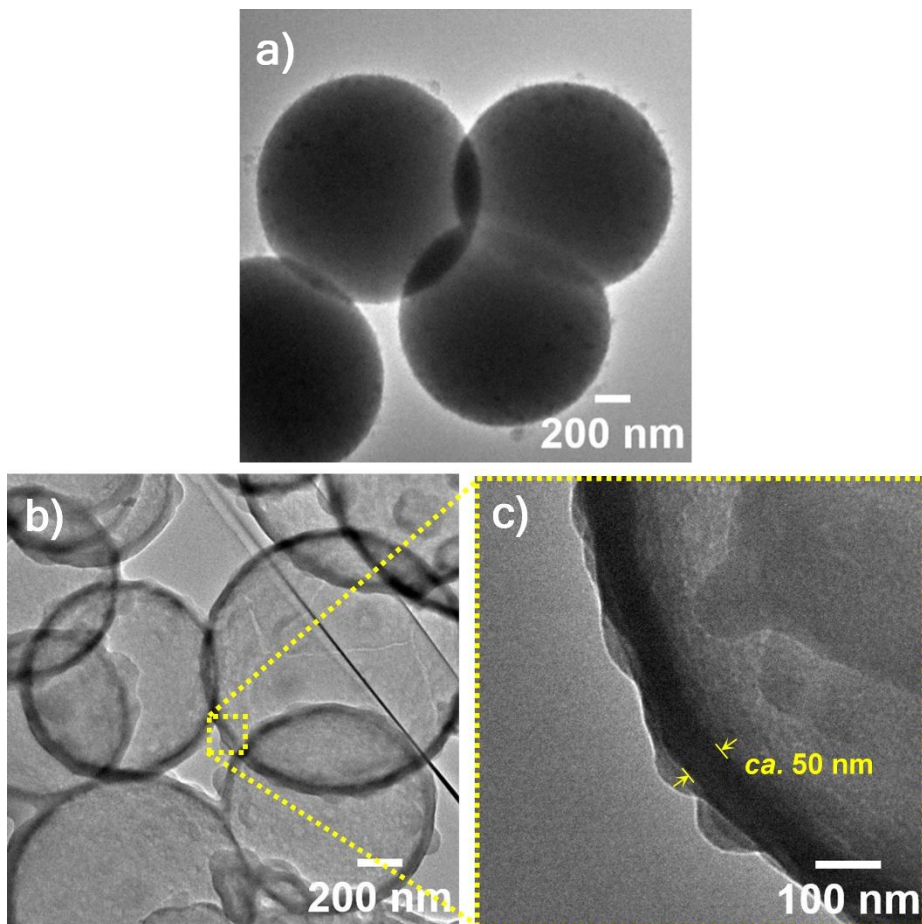


Figure 58. TEM images of (a) SiO₂ microsphere and (b, c) micro-sized HCS.

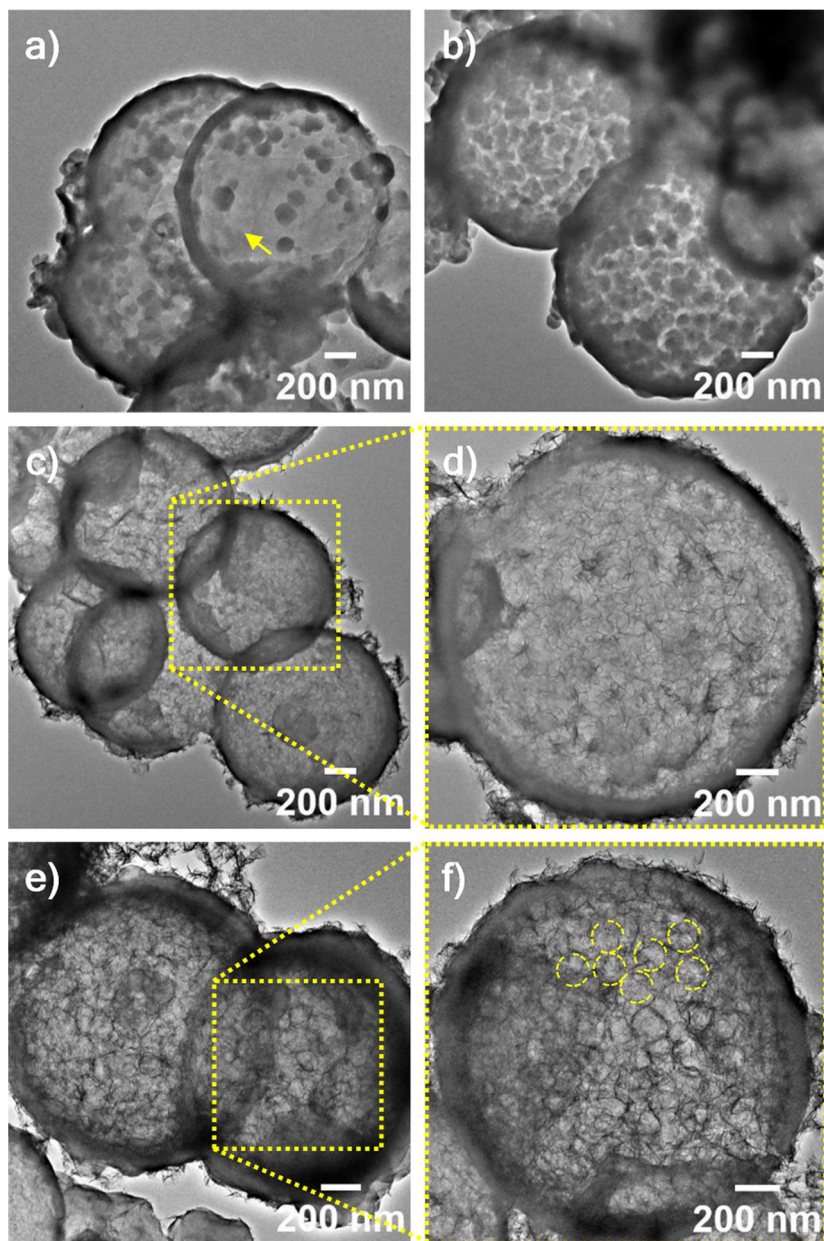


Figure 59. TEM images of (a) HCS@ZIF-67-1, (b) HCS@ZIF-67-2, (c, d) HIH-LDH-1, and (e, f) HIH-LDH-2.

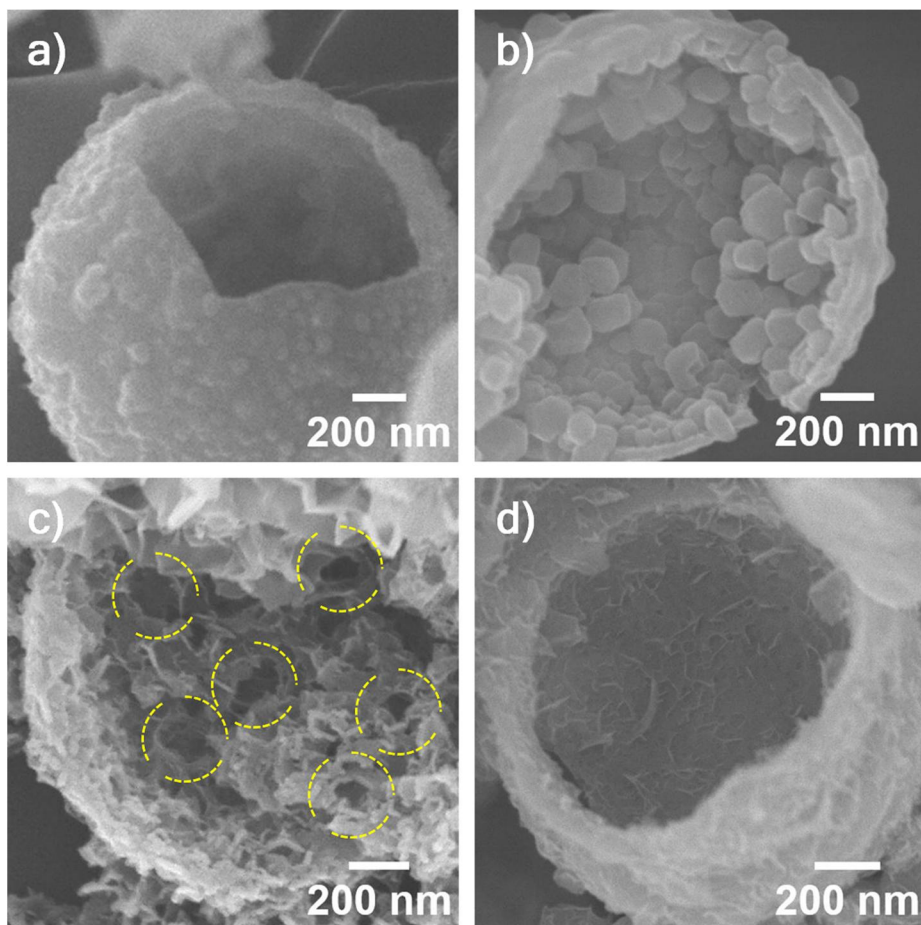


Figure 60. SEM images of (a) HCS, (b) HCS@ZIF-67-2, (c) HIH-LDH-2, and (d) HIH-LDH-1.

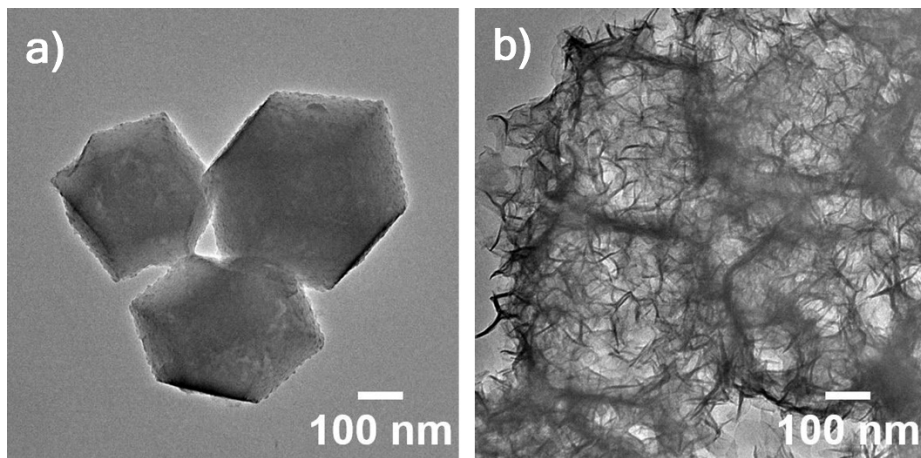


Figure 61. TEM images of (a) pristine ZIF-67 and (b) H-LDH.

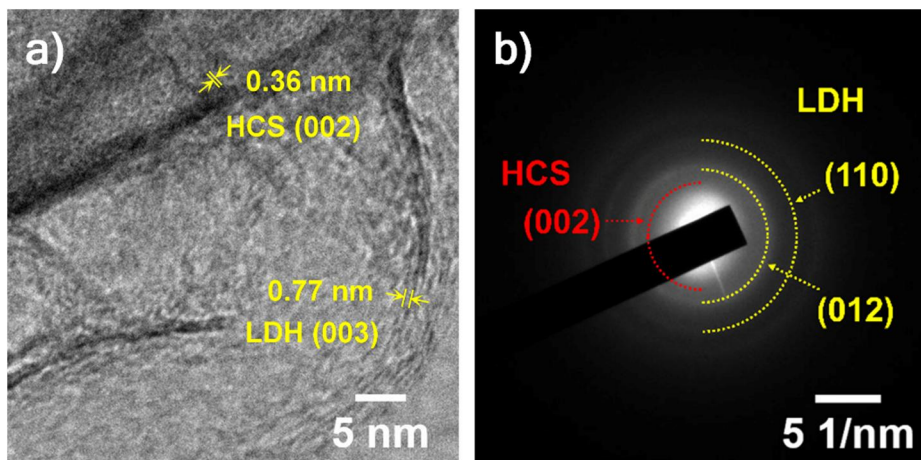


Figure 62. (a) HR-TEM image and (b) SAED pattern of HIIH-LDH-2.

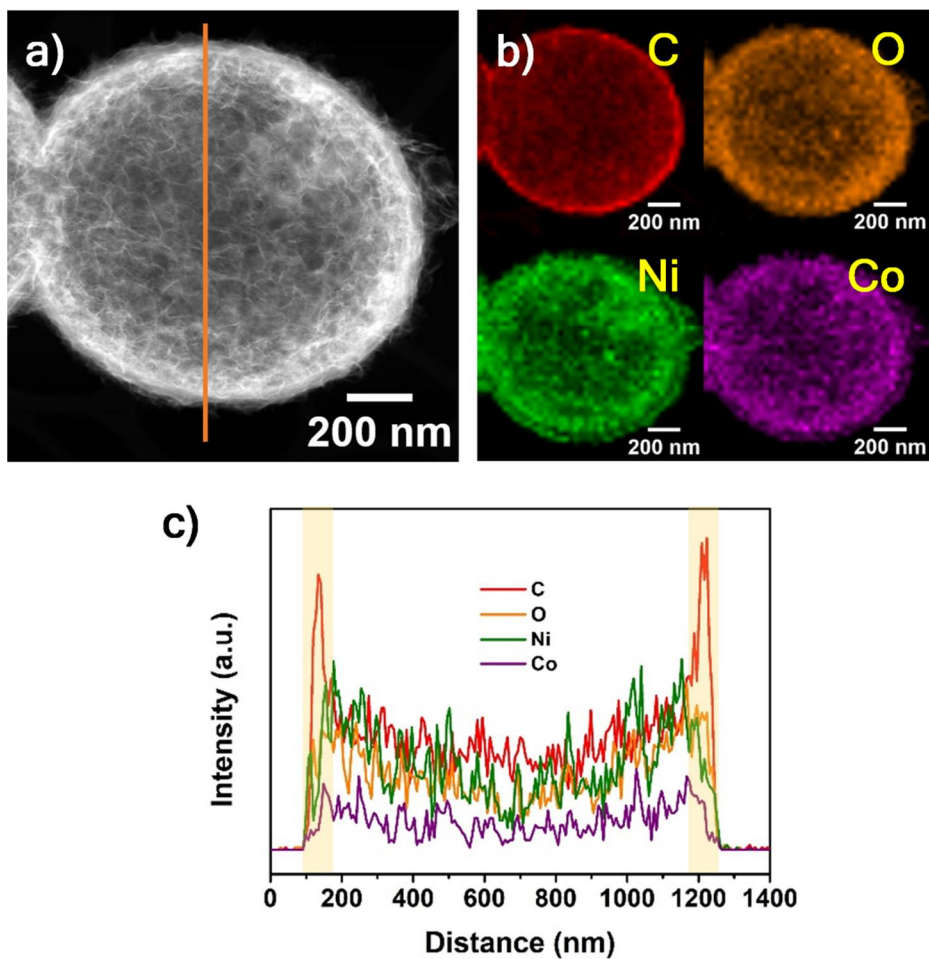


Figure 63. (a) STEM image, (b) STEM elemental mapping images (C, O, Ni, and Co), and (c) STEM-EDX line analysis result of HIH-LDH-2.

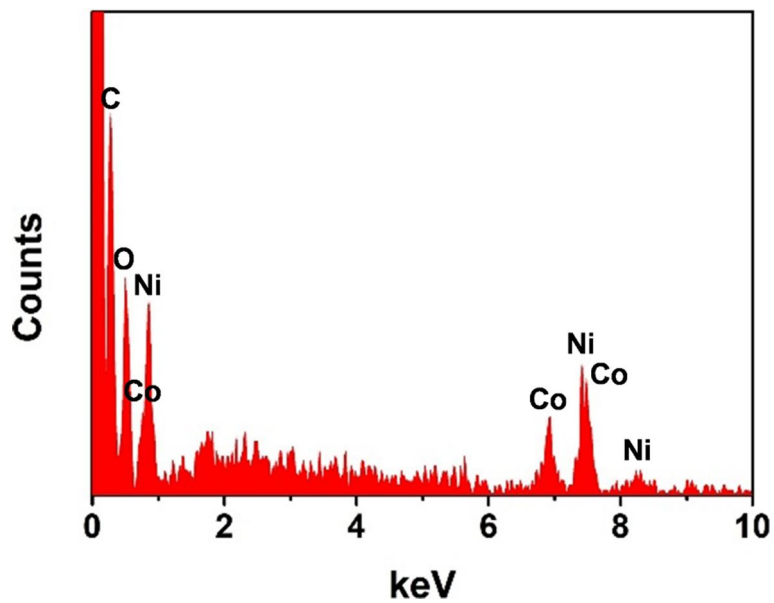


Figure 64. EDX spectrum of HIH-LDH-2.

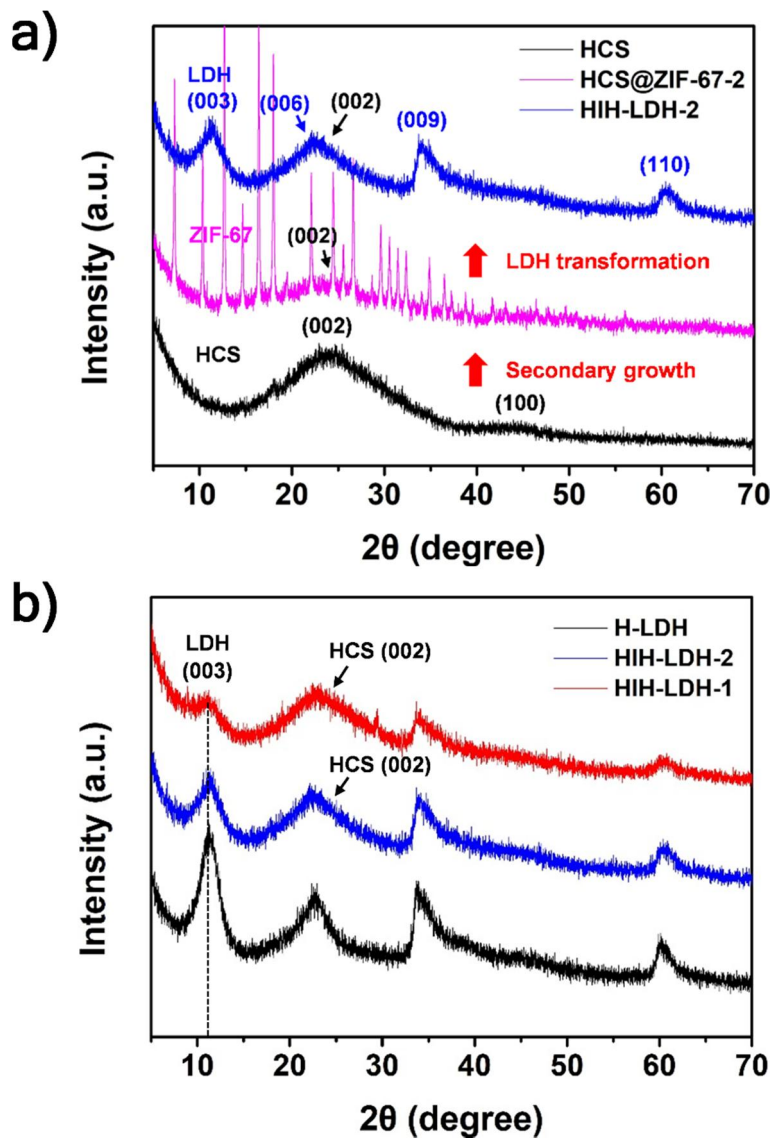


Figure 65. (a) XRD spectra of HCS, HCS@ZIF-67-2, and HIH-LDH-2. (b) XRD spectra of H-LDH, HIH-LDH-1, and HIH-LDH-2.

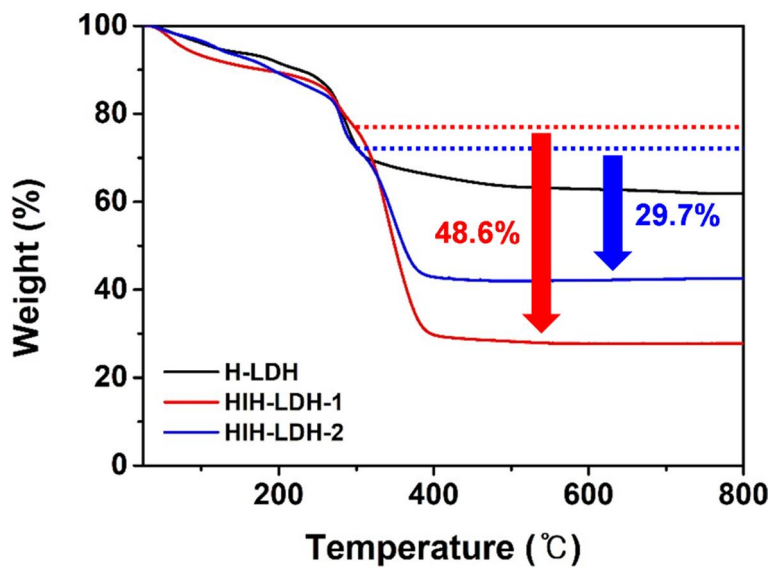


Figure 66. TGA curves of H-LDH, HIH-LDH-1, and HIH-LDH-2.

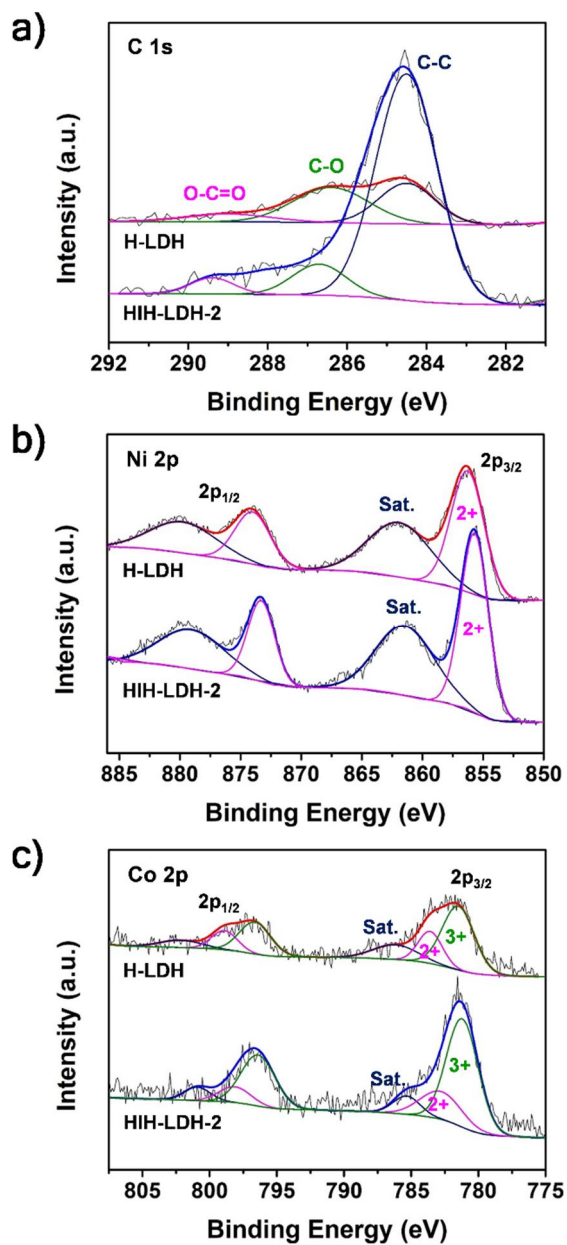


Figure 67. The high-resolution XPS patterns of H-LDH and HIH-LDH-2: (a) C 1s. (b) Ni 2p. (c) Co 2p.

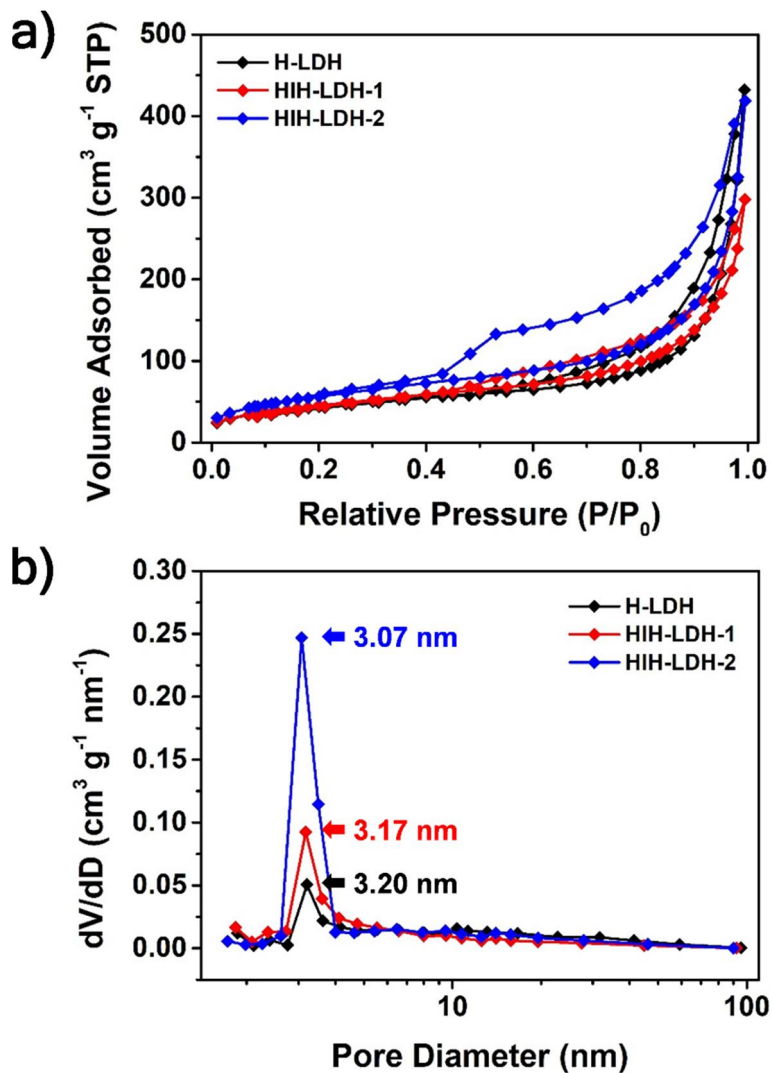
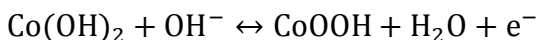
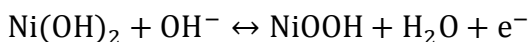


Figure 68. (a) Nitrogen adsorption/desorption plots and (b) pore-size distribution curves of H-LDH, HIH-LDH-1, and HIH-LDH-2.

3.3.3. Electrochemical properties of the samples

From the motivation by the unique structural characteristics such as hollow-in-hollow structure, the potential of HIIH-LDH-2 as the SC electrode was investigated in 1 M KOH electrolyte with three-electrode system. The electrochemical properties of H-LDH and HIIH-LDH-1-based electrodes were also evaluated for comparison. **Figure 69** shows the comparative CV curves of H-LDH, HIIH-LDH-1, and HIIH-LDH-2 at the fixed scan rate of 20 mV s^{-1} in the potential range of 0.0–0.5 V (vs. Ag|AgCl). As can be seen from the shapes of these curves, all samples demonstrated battery-type behaviors with apparent redox peaks, indicating that the energy storage of the samples mainly came from the faradaic reactions of Ni-Co LDHs in their structures. In specific, the anodic peaks of the samples were observed at 0.321–0.346 V and the cathodic peaks were appeared at 0.224–0.229 V, which were associated with the faradaic reactions below [94,114]:



Particularly, HIIH-LDH-2 offered higher redox current intensity and larger CV loop area compared with those of H-LDH and HIIH-LDH-1, implying its higher energy storage performance. The CV profiles of the

H-LDH, HIIH-LDH-1, and HIIH-LDH-2-based electrodes at various scan rates are also illustrated in **Figure 70**. Noticeably, when the scan rate increased from 20 to 400 mV s^{-1} , the shapes of the CV curves of HIIH-LDH-1 and HIIH-LDH-2 were almost unchanged, while that of H-LDH was somewhat distorted. This was further confirmed by the smaller anodic/cathodic peak shift of HIIH-LDH-1 (+0.052 V/−0.025 V) and HIIH-LDH-2 (+0.072 V/−0.043 V) than that of H-LDH (+0.109 V/−0.058 V). Considering the above result, in composite form, the hollow structure of HCS effectively supported the fast and reversible faradaic reaction of Ni-Co LDHs at high scan rate condition, resulting in improved rate performance of HIIH-LDH-1 and HIIH-LDH-2. For further investigation, GCD curves of H-LDH, HIIH-LDH-1, and HIIH-LDH-2 with different current densities were obtained at potential range from 0.0 V to 0.5 V (*vs.* Ag|AgCl) (**Figure 71**). All samples displayed nonlinear discharging curves with obvious potential plateaus, indicating that they were battery-like materials, which were consistent with the CV results. **Figure 72** exhibits the specific capacities of the samples under current densities of 5–80 A g^{-1} , which were calculated based on the corresponding discharging curves. Compared to the other samples, HIIH-LDH-1 delivered lower capacity values (110.7 mAh g^{-1} at 5 A g^{-1})

due to the low proportion (51.4%) of Ni-Co LDH in its hybrid configuration (**Figure 66**). Interestingly, although HII-LDH-2 was also present in hybrid form, the maximum capacity value of HII-LDH-2 (156.4 mAh g⁻¹ at 5 A g⁻¹) was comparable to that of H-LDH (160.0 mAh g⁻¹ at 5 A g⁻¹), which was only composed of the Ni-Co LDHs. Furthermore, when the current density increased to 80 A g⁻¹, HII-LDH-2 showed drastically enhanced rate performance (70% retention of its maximum capacity) compared with that of H-LDH (49% retention) (**Table 3**). The high specific capacity and remarkable rate capability of HII-LDH-2 can be attributed to a couple of factors. First, HII-LDH-2 included the high proportion (70.3%) of hollow Ni-Co LDHs in its hybrid architecture. These materials possessed the unique hollow and mesoporous structures derived from numerous interlaced Ni-Co LDH nanosheets, providing sufficient faradaic reaction sites. Second, HII-LDH-2 demonstrated the larger electrochemical interface (304.3 m² g⁻¹) compared with that of H-LDH (223.0 m² g⁻¹). Because the HCS served as the effective growth substrate for hollow Ni-Co LDHs, the agglomeration of electroactive materials was alleviated compared to single H-LDHs, resulting in enlarged electrochemical interface of HII-LDH-2. Accordingly, the charge storage reaction of

HIH-LDH-2 was further promoted with decreased ion diffusion length. Finally, the distinctive hollow-in-hollow structure significantly increased the rate capability of HIH-LDH-2. It has been reported that the hollow structure can improve the rate performance by serving as the electrolyte reservoir, which rapidly supplied the electrolyte ions to surrounding electroactive materials [43,44]. Unlike H-LDH, HIH-LDH-2 offered two different sizes of ion reservoirs in its architecture; bigger one with carbon shell and smaller one consisting of Ni-Co LDH nanosheets. During the charge storage process of HIH-LDH-2, dual ion reservoirs were applied to promote the ion diffusion throughout the architecture, resulting in high capacity retention even at severe discharging condition. Since the hollow-in-hollow structure could not be achieved in the synthesis condition of HIH-LDH-1, it did not exhibit much improved rate performance (50% capacity retention at 80 A g^{-1}). **Figure 73** displays the EIS plots of H-LDH, HIH-LDH-1, and HIH-LDH-2 between the frequency range from 10 mHz to 100 kHz. All plots of the samples consisted of semicircle and straight line in the high- and low-frequency regions, respectively. In particular, charge transfer resistance (R_{ct}) of each sample was acquired by measuring the semicircle diameter of corresponding plot. The R_{ct} of H-LDH, HIH-

LDH-1, and HII-LDH-2 was 1.529, 1.124, and 0.879 Ω , respectively, meaning that the charge transfer process was the most facilitated on the surface of HII-LDH-2. The smaller R_{ct} value of HII-LDH-2 compared with that of H-LDH and HII-LDH-1 was related to its larger electrochemical interface and unique hollow-in-hollow structure, which effectively shortened the ion transport path. **Figure 74** illustrates the cycling test results of the samples, which were performed by 10000 cycles of charging/discharging at the current density of 10 A g⁻¹. Notably, HII-LDH-1 and HII-LDH-2 maintained 74.3 and 73.4% of their original capacities after 10000 cycles, while H-LDH only retained 45.2% of its initial capacity (**Table 3**). This result indicated that the supporting carbon shells of HII-LDH-1 and HII-LDH-2 effectively buffered the volume changes of surrounding Ni-Co LDHs during the cycle tests, resulting in enhancement of cycle stabilities.

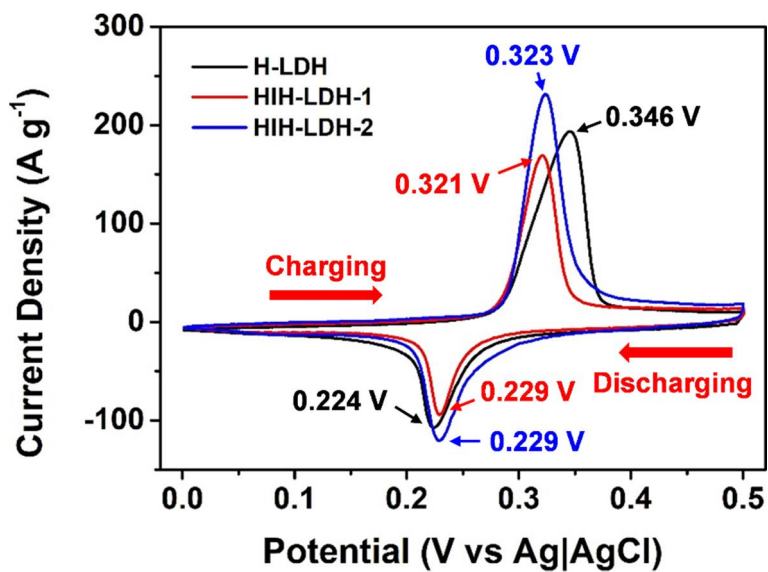


Figure 69. CV curves of H-LDH, HIH-LDH-1, and HIH-LDH-2 at the scan rate of 20 mV s^{-1} .

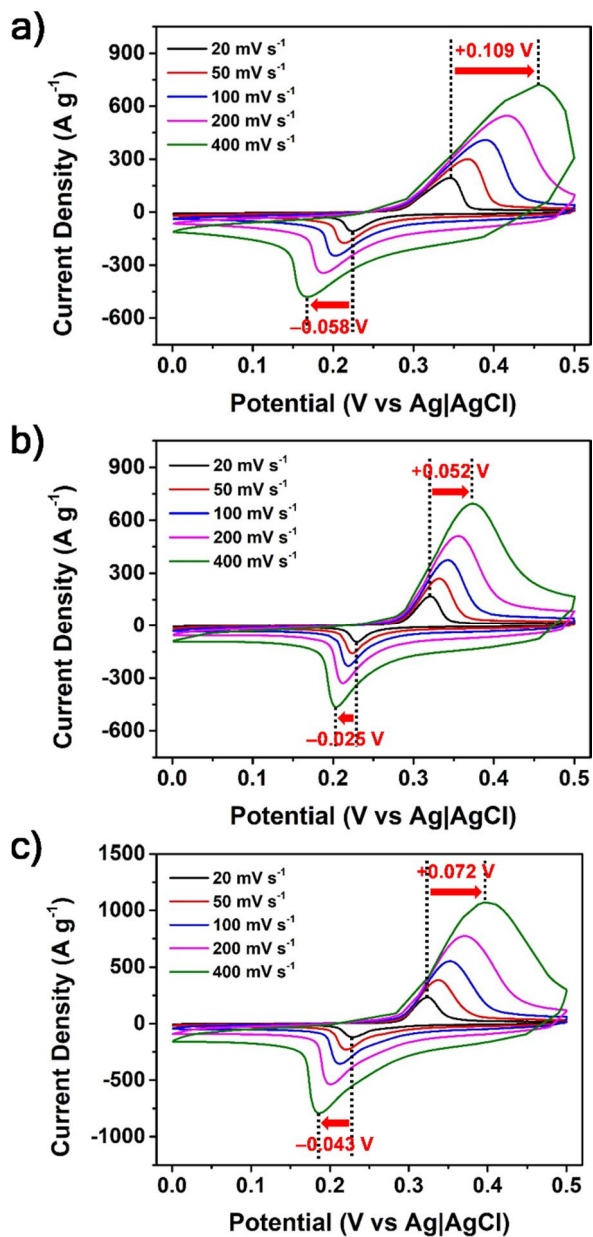


Figure 70. CV curves of (a) H-LDH, (b) H1H-LDH-1, and (c) H1H-LDH-2 with different scan rates.

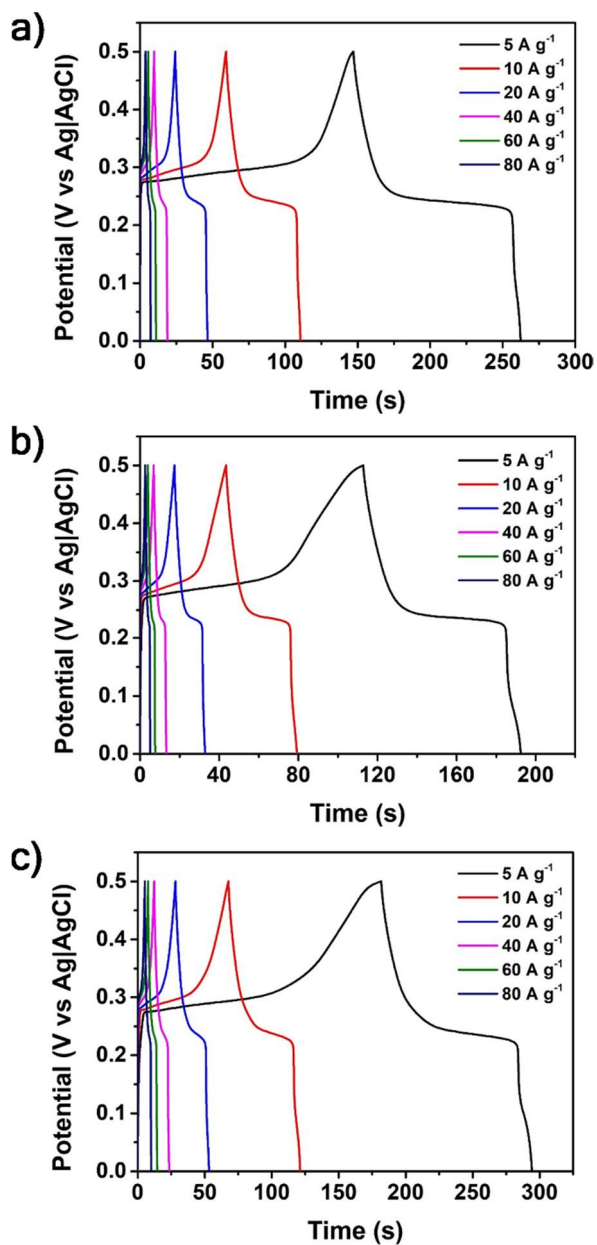


Figure 71. GCD curves of (a) H-LDH, (b) HIH-LDH-1, and (c) HIH-LDH-2 with different current densities.

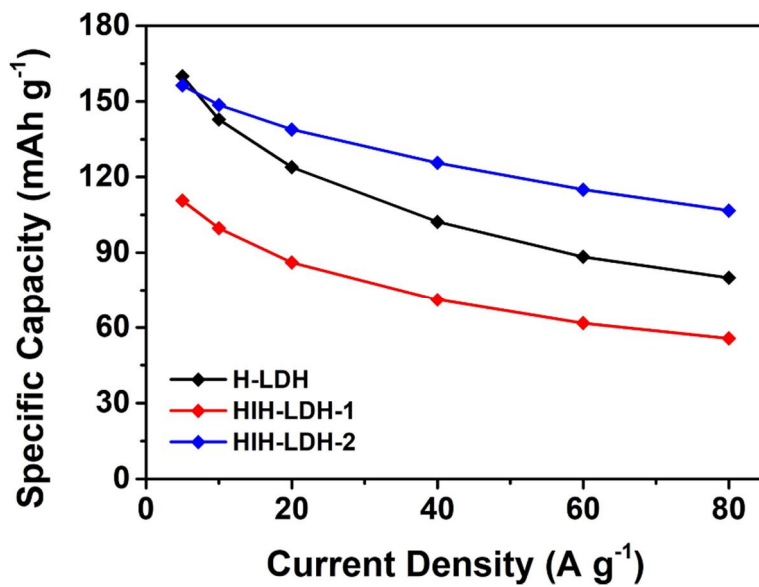


Figure 72. Specific capacity of H-LDH, HIH-LDH-1, and HIH-LDH-2 as a function of current density.

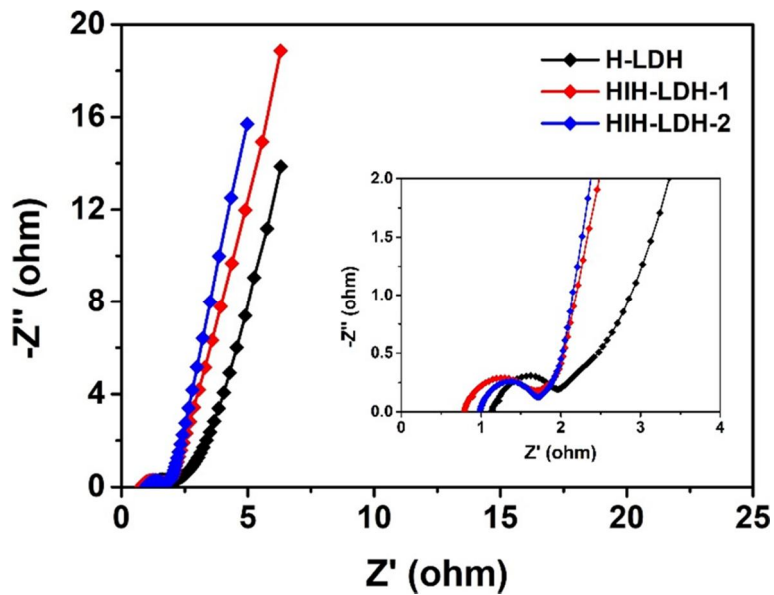


Figure 73. Nyquist plots of H-LDH, HIH-LDH-1, and HIH-LDH-2 in the frequency range from 10 mHz to 100 kHz. The inset shows the high-frequency region of the plots.

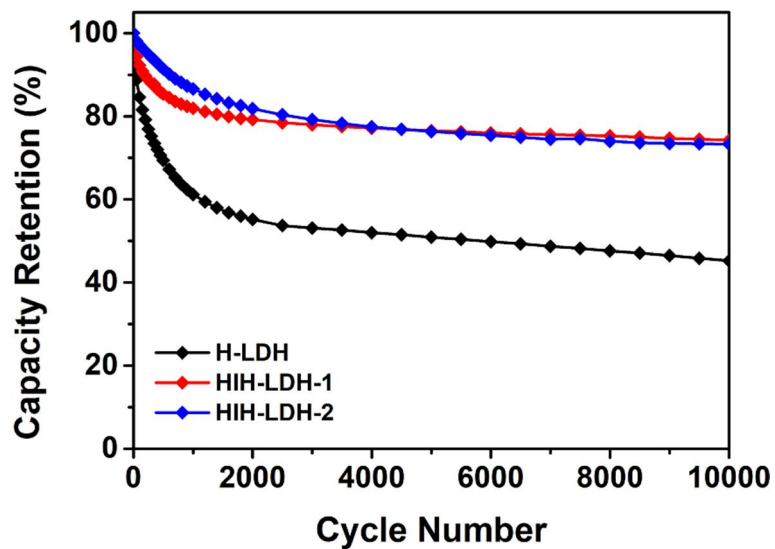


Figure 74. Cycling performances of H-LDH, HIH-LDH-1, and HIH-LDH-2 measured at 10 A g^{-1} for 10000 cycles.

Table 3. Rate capabilities (5–80 A g⁻¹) and cycle stabilities (10 A g⁻¹, 10000 cycles) of H-LDH, H1H-LDH-1, and H1H-LDH-2.

Sample	Rate capability (capacity retention, %)	Cycle stability (capacity retention, %)
H-LDH	49.4	45.2
H1H-LDH-1	50.2	74.3
H1H-LDH-2	70.0	73.4

3.3.4. Characterization and electrochemical properties of negative electrode material (MPRGO)

The morphological and structural features of MPRGO are already specified in the former part (3.2.4.). In this part, GCD tests at higher current densities (5–80 A g⁻¹) and EIS measurement of MPRGO are additionally presented.

The electrochemical properties of MPRGO were analyzed in 1 M KOH electrolyte with three-electrode system. The GCD curves were acquired under different current densities (5–80 A g⁻¹) in the potential range from -1 to 0 V (*vs.* Ag|AgCl) (**Figure 75a**). Particularly, MPRGO displayed capacitive behavior with linear discharging curves. According to the calculation of specific capacitance using GCD results, the capacitance of MPRGO was 300.3 F g⁻¹ at 5 A g⁻¹, and it was still 247.8 F g⁻¹ when the current density increased to 80 A g⁻¹ (83% retention) (**Figure 75b**). As a result of EIS measurement, MPRGO showed the low R_{ct} value (10.6 Ω) and steep slope in its Nyquist plot, demonstrating the ideal capacitive behavior (**Figure 75c**).

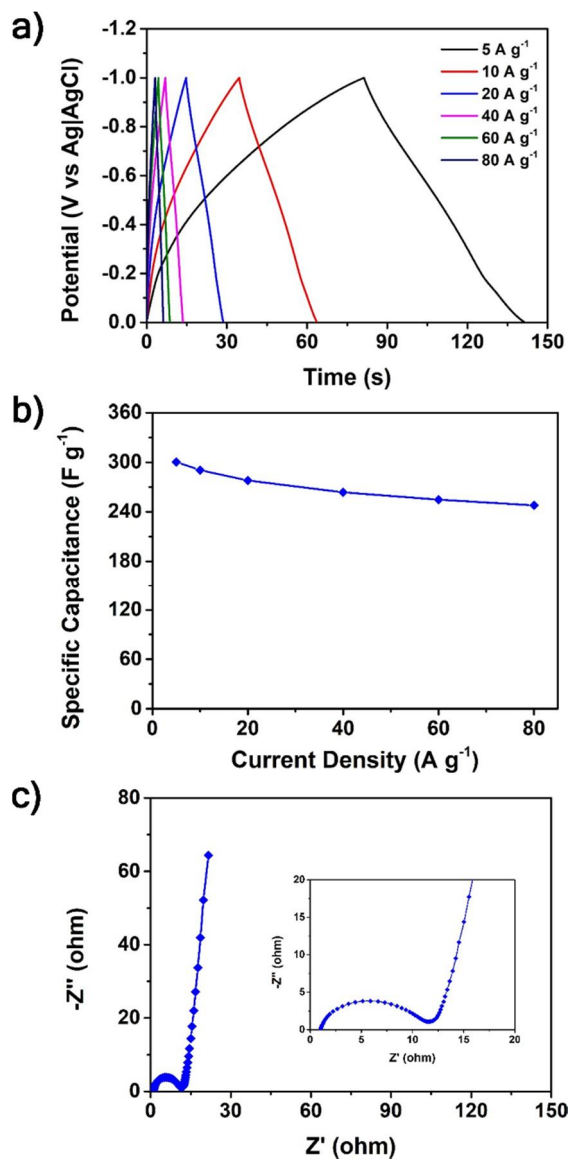


Figure 75. Electrochemical results of MPRGO: (a) GCD curves with different current densities. (b) Specific capacitance as a function of current density. (c) Nyquist plot (inset: high-frequency region of the plot).

3.3.5. Studies of the hybrid supercapacitor (HSC)

For evaluating the practical applicability, HIIH-LDH-2-based HSC was facilely fabricated using HIIH-LDH-2 as the positive electrode, MPRGO as the negative electrode, and the PVA-KOH gel electrolyte (**Figure 76**). Before assembling the device, the mass loading of the positive electrode (m_+) and negative electrode (m_-) was optimized according to the equation of charge balance theory, which was described in the former part (3.2.5.). Using the values obtained with three-electrode system at the current density of 5 A g^{-1} , the optimal mass ratio (m_+/m_-) was determined to be 0.535. In order to find out the maximum applicable voltage window of the as-prepared HSC device, CV tests were implemented at the constant scan rate of 50 mV s^{-1} under different voltage windows (**Figure 77**). As a result, when increasing the operating voltage window to 0.0–1.5 V, some variations were observed from the CV curve, meaning that irreversible reactions (*e.g.*, hydrogen/oxygen evolution) occurred within the HSC device above the voltage window of 0.0–1.4 V. As such, the voltage window of the HSC device could be extended up to 1.4 V. **Figure 78a** exhibits the CV curves of HIIH-LDH-2//MPRGO at different scan rates with the voltage window of 0.0–1.4 V. Unlike the obvious redox peaks observed in the

CV curves of HIIH-LDH-2-based electrode, the CV curves of HIIH-LDH-2//MPRGO displayed quasi-rectangular shapes, representing its typical capacitive behavior. Particularly, even at the high scan rate of 400 mV s^{-1} , the shape of the CV curves was almost same, indicating the high rate capability of the HSC device. The GCD curves of HIIH-LDH-2//MPRGO with different current densities in the voltage window of 0.0–1.4 V were depicted in **Figure 78b**. Combined with the CV data, the nearly linear discharging curves of HIIH-LDH-2//MPRGO further implied its capacitive behavior. The calculated specific capacities of HIIH-LDH-2//MPRGO as a function of current density are illustrated in **Figure 78c**. According to the calculation, the capacity value of HIIH-LDH-2//MPRGO was 53.4, 49.5, 45.4, 40.6, 37.4, and 35.3 mAh g^{-1} when the current density was 5, 10, 20, 40, 60, and 80 A g^{-1} , respectively.

Based on the above electrochemical results, the energy density and power density of HIIH-LDH-2//MPRGO were calculated and expressed as the Ragone plot (**Figure 79**). Notably, HIIH-LDH-2//MPRGO showed the maximum energy density of 34.5 Wh kg^{-1} at the power density of 3.2 kW kg^{-1} , and it maintained 24.5 Wh kg^{-1} at the peak power density of 55 kW kg^{-1} . Additionally, HIIH-LDH-2//MPRGO

exhibited excellent cycling stability by preserving 84.0% of its initial capacity after 10000 cycles of charging/discharging at a current density of 10 A g⁻¹ (**Figure 80**). Therefore, considering the above results, the combination of HII-LDH-2 and MPRGO has potential applicability to high-performance HSC devices. In particular, the singularly high power density of HII-LDH-2//MPRGO can be favorably applied to the modern electronic industry increasingly demanding high-rate devices.

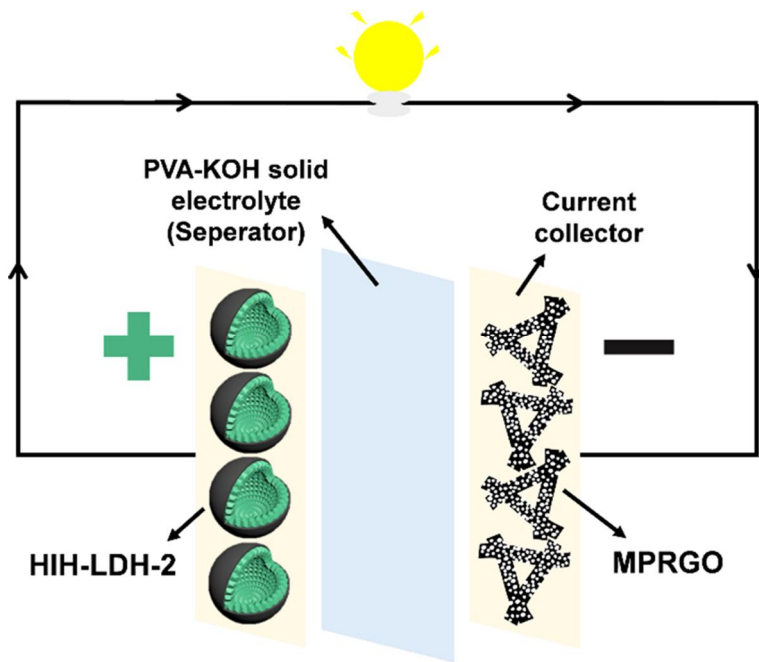


Figure 76. Schematic diagram of the assembled HSC device (HIH-LDH-2//MPRGO).

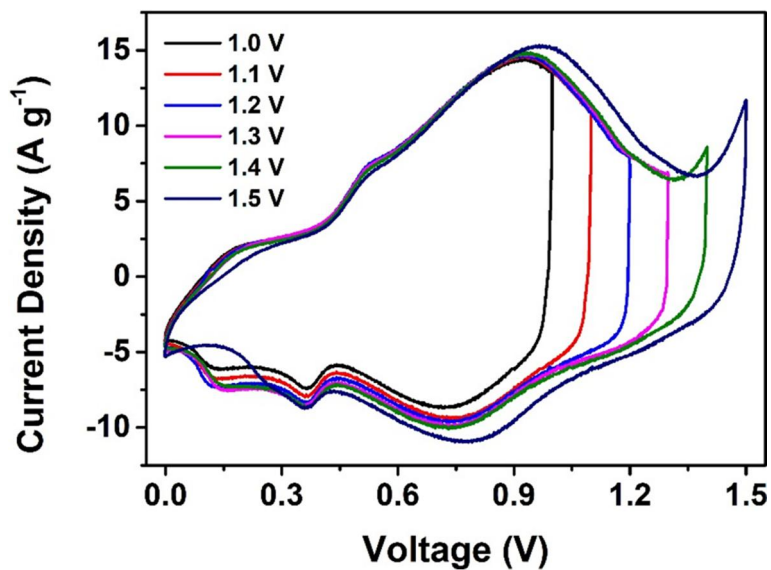


Figure 77. CV curves of HIH-LDH-2-based HSC under various voltage windows, which were measured at 50 mV s⁻¹.

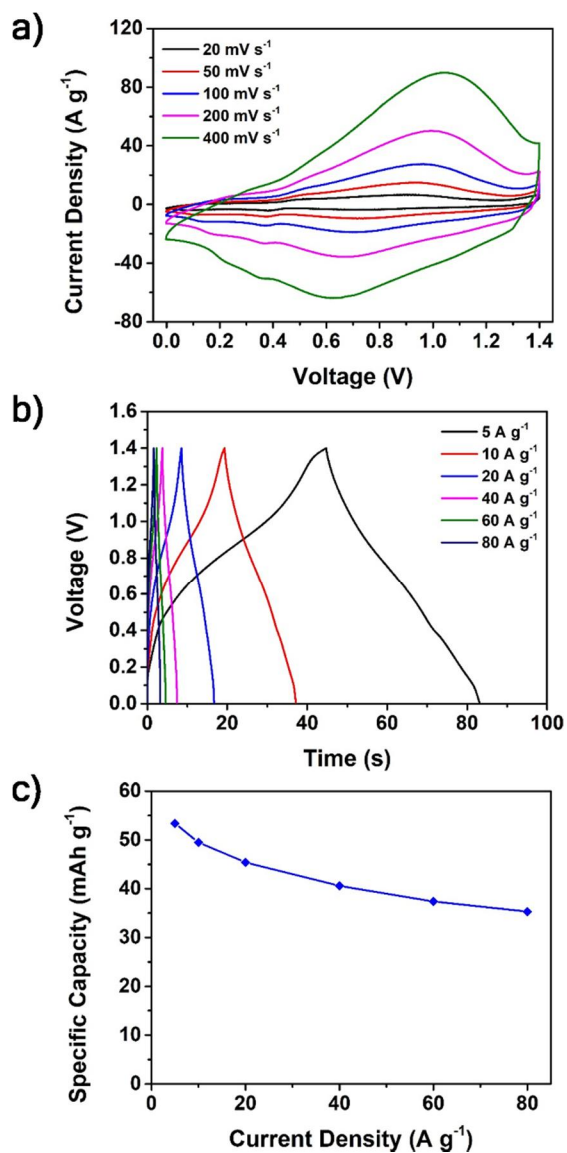


Figure 78. Electrochemical results of HIH-LDH-2//MPRGO: (a) CV curves with different scan rates. (b) GCD curves under various current densities. (c) Specific capacity as a function of current density.

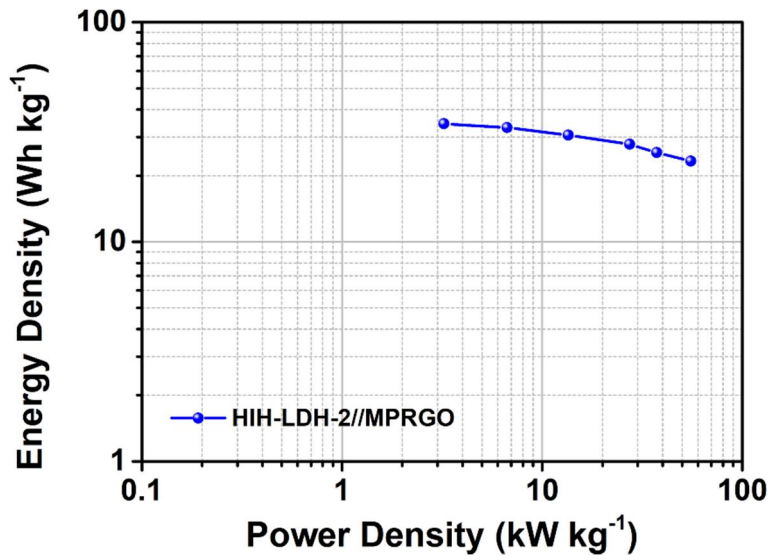


Figure 79. Ragone plot of HIH-LDH-2-based HSC.

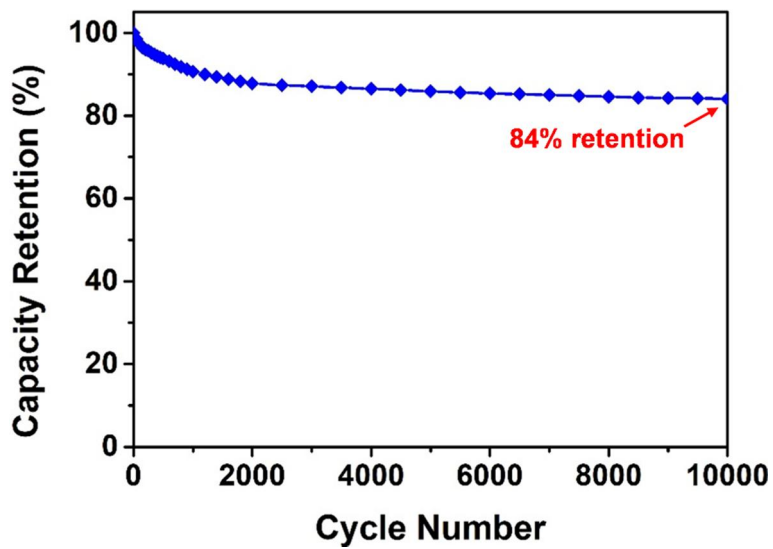


Figure 80. Cycling performances of HIH-LDH-2-based HSC measured at 10 A g^{-1} for 10000 cycles.

4. Conclusion

A variety of ZIF derivatives/carbon structures were synthesized and successfully employed for SC electrodes. In the manufacturing process, the well-controlled ZIF precursor conversion reaction or additional carbon hybridization allowed the resulting active material to possess the favorable structures for charge storage such as 1D, heterogeneous composite, and hollow architectures. Owing to their decent intrinsic properties and rationally designed structures, the SC electrode materials prepared in this dissertation offered high electrochemical performances in terms of charge storage capability, rate performance, and cycle stability. The subtopics are concluded in the viewpoint of each subtopic as follows:

1. ZPCNF-4, a hybrid structure of ZnO QDs@carbons and CNF, is produced *via* carbonization of electrospun ZIF-8/PVA nanofibers. Interestingly, this hierarchical fibrous architecture has porous structure and pseudocapacitive ZnO QDs on the surface, and 1D conductive path on the central axis. Because of these structural characteristics, ZPCNF-4 showed high capacitance (346.0 F g^{-1} at 0.5 A g^{-1}), which was 3.1 folds enhanced value compared to PCNF, along with reliable rate

performance (79% capacitance retention at 8 A g^{-1}) and long-term cycle stability (85% capacitance retention after 5000 cycles).

2. Various-sized ZIF-67s were transformed into their respective CNG/Co(OH)₂ architectures using the facile, one-pot hydrothermal reaction. These heterogeneous composites were composed of numerous Co₃O₄ nanograins and their supporting Co(OH)₂ plate. By preventing aggregation issues, CNG/Co(OH)₂ exhibited larger electrochemical interface than that of single Co₃O₄ or Co(OH)₂. Owing to their unique morphological features, CNG/Co(OH)₂ structures demonstrated large capacity value, which was higher in the order of S₋, M₋, and L₋ CNG/Co(OH)₂. In particular, L₋ CNG/Co(OH)₂ delivered remarkable capacity (184.9 mAh g^{-1} at 1 A g^{-1}), which was 4–5 times higher value compared with that of single Co₃O₄ or Co(OH)₂, along with decent rate capability (76% capacity retention at 16 A g^{-1}) and reliable cycle stability (90% capacity retention after 5000 cycles). Moreover, L₋ CNG/Co(OH)₂-based HSC illustrated the maximum energy density of 37.6 Wh kg^{-1} and peak power density of 47 kW kg^{-1} , representing practical applicability.

3. A novel hybrid material with hollow-in-hollow structure consisting of ZIF-67-derived hollow Ni-Co LDHs and their supporting HCS

carbon shell was synthesized by chemical regrowth/etching process of HCS@ZIF-67. Particularly, during the charge storage reaction, as-formed hollow-in-hollow structure provided much advantages including enlarged electrochemical interface, intact architecture of hollow Ni-Co LDHs therein, and promoted ion diffusion by the dual hollow system. Thus, HIH-LDH-2 displayed high capacity (156.4 mAh g⁻¹ at 5 A g⁻¹), excellent rate capability (70% capacity retention at 80 A g⁻¹), and long cycle life (74% capacity retention after 10000 cycles). According to the above results, the rate and cycle performances of HIH-LDH-2 were 1.4 and 1.6 folds improved than those of H-LDH, respectively. Furthermore, HIH-LDH-2-based HSC showed its practical applicability by offering the maximum energy density of 34.5 Wh kg⁻¹ and peak power density of 55 kW kg⁻¹.

References

- [1] P. Simon, Y. Gogotsi, *Nat. Mater.*, **2008**, 7, 845.
- [2] M. F. El-Kady, V. Strong, S. Dubin, R. B. Kaner, *Science*, **2012**, 335, 1326.
- [3] M. D. Stoller, R. S. Ruoff, *Energy Environ. Sci.*, **2010**, 3, 1294.
- [4] B. Li, F. Dai, Q. Xiao, L. Yang, J. Shen, C. Zhang, M. Cai, *Energy Environ. Sci.*, **2016**, 9, 102.
- [5] J. S. Lee, D. H. Shin, J. Jang, *Energy Environ. Sci.*, **2015**, 8, 3030.
- [6] K. Qiu, Y. Lu, D. Zhang, J. Cheng, H. Yan, J. Xu, X. Liu, J. -K. Kim, Y. Luo, *Nano Energy*, **2015**, 11, 687.
- [7] D. H. Shin, J. S. Lee, J. Jun, J. Jang, *J. Mater. Chem. A*, **2014**, 2, 3364.
- [8] J. S. Lee, C. Lee, J. Jun, D. H. Shin, J. Jang, *J. Mater. Chem. A*, **2014**, 2, 11922.
- [9] M. Huang, Y. Zhang, F. Li, L. Zhang, Z. Wen, Q. Liu, *J. Power Sources*, **2014**, 252, 98.
- [10] R. R. Salunkhe, B. P. Bastakoti, C. -T. Hsu, N. Suzuki, J. H. Kim, S. X. Dou, C. -C. Hu, Y. Yamauchi, *Chem. Eur. J.*, **2014**, 20, 3084.
- [11] Y. Wang, Y. Song, Y. Xia, *Chem. Soc. Rev.*, **2016**, 45, 5925.
- [12] J. Xie, P. Yang, Y. Wang, T. Qi, Y. Lei, C. M. Li, *J. Power Sources*, **2018**, 401, 213.
- [13] S. C. Sekhar, G. Nagaraju, J. S. Yu, *Nano Energy*, **2018**, 48, 81.
- [14] M. A. Garakani, S. Abouali, Z. -L. Xu, J. Huang, J. -Q. Huang, J. -K. Kim, *J. Mater. Chem. A*, **2017**, 5, 3547.
- [15] R. Jia, F. Zhu, S. Sun, T. Zhai, H. Xia, *J. Power Sources*, **2017**, 341, 427.
- [16] A. Ramadoss, K. -Y. Yoon, M. -J. Kwak, S. -I. Kim, S. -T. Ryu, J. -H. Jang, *J. Power Sources* **2017**, 337, 159.

- [17] X. Yu, S. Yun, J. S. Yeon, P. Bhattacharya, L. Wang, S. W. Lee, X. Hu, H. S. Park, *Adv. Energy Mater.*, **2018**, 8, 1702930.
- [18] Y. Zhu, S. Murali, M. D. Stoller, K. J. Ganesh, W. Cai, P. J. Ferreira, A. Pirkle, R. M. Wallace, K. A. Cychoz, M. Thommes, D. Su, E. A. Stach, R. S. Ruoff, *Science*, **2011**, 332, 1537.
- [19] L. J. Wang, M. F. El-Kady, S. Dubin, J. Y. Hwang, Y. Shao, K. Marsh, B. McVerry, M. D. Kowal, M. F. Mousavi, R. B. Kaner, *Adv. Energy Mater.*, **2015**, 5, 1500786.
- [20] G. Lee, C. Lee, C. -M. Yoon, M. Kim, J. Jang, *ACS Appl. Mater. Interfaces*, **2017**, 9, 5222.
- [21] B. Liu, M. Yang, H. Chen, Y. Liu, D. Yang, H. Li, *J. Power Sources*, **2018**, 397, 1.
- [22] K. S. Novoselov, V. I. Fal'ko, L. Colombo, P. R. Gellert, M. G. Schwab, K. Kim, *Nature*, **2012**, 490, 192.
- [23] S. Stankovich, D. A. Dikin, G. H. B. Dommett, K. M. Kohlhaas, E. J. Zimney, E. A. Stach, R. D. Piner, S. T. Nguyen, R. S. Ruoff, *Nature*, **2006**, 442, 282.
- [24] I. K. Moon, J. Lee, R. S. Ruoff, H. Lee, *Nat. Commun.*, **2010**, 1, 73.
- [25] M. D. Stoller, S. Park, Y. Zhu, J. An, R. S. Ruoff, *Nano Lett.*, **2008**, 8, 3498.
- [26] V. Augustyn, P. Simon, B. Dunn, *Energy Environ. Sci.*, **2014**, 7, 1597.
- [27] Q. Jiang, N. Kurra, M. Alhabeb, Y. Gogotsi, H. N. Alshareef, *Adv. Energy Mater.*, **2018**, 8, 1703043.
- [28] J. Jun, J. S. Lee, D. H. Shin, S. G. Kim, J. Jang, *Nanoscale*, **2015**, 7, 16026.
- [29] X. -Y. Zhang, L. -Q. Han, C. -Y. Wang, M. -M. Chen, *Mater. Lett.*, **2014**, 136, 78.
- [30] G. Xiong, P. He, D. Wang, Q. Zhang, T. Chen, T. S. Fisher, *Adv.*

- Funct. Mater.*, **2016**, 26, 5460.
- [31] J. Zhao, Z. Li, X. Yuan, Z. Yang, M. Zhang, A. Meng, Q. Li, *Adv. Energy Mater.*, **2018**, 8, 1702787.
- [32] Y. Lu, L. Li, D. Chen, G. Shen, *J. Mater. Chem. A*, **2017**, 5, 24981.
- [33] G. Lee, J. Jang, *J. Power Sources* **2019**, 423, 115.
- [34] J. Mei, W. Fu, Z. Zhang, X. Jiang, H. Bu, C. Jiang, E. Xie, W. Han, *Energy*, **2017**, 139, 1153.
- [35] W. Wang, W. Wang, M. Wang, X. Guo, *Chem. Asian J.*, **2014**, 9, 2590.
- [36] P. Simon, Y. Gogotsi, B. Dunn, *Science*, **2014**, 343, 1210.
- [37] T. Brousse, D. Bélanger, J. W. Long, *J. Electrochem. Soc.*, **2015**, 162, A5185.
- [38] E. Frackowiak, *Phys. Chem. Chem. Phys.*, **2007**, 9, 1774.
- [39] H. Zhou, S. Zhu, M. Hibino, I. Honma, *J. Power Sources*, **2003**, 122, 219.
- [40] H. -J. Liu, J. Wang, C. -X. Wang, Y. -Y. Xia, *Adv. Energy Mater.*, **2011**, 1, 1101.
- [41] A. Chen, Y. Li, L. Liu, Y. Yu, K. Xia, Y. Wang, S. Li, *Appl. Surf. Sci.*, **2017**, 393, 151.
- [42] L. Li, R. Li, S. Gai, S. Ding, F. He, M. Zhang, P. Yang, *Chem. Eur. J.*, **2015**, 21, 7119.
- [43] T. Liu, L. Zhang, B. Cheng, W. You, J. Yu, *Chem. Commun.*, **2018**, 54, 3731.
- [44] J. Tian, H. Zhang, Z. Li, *ACS Appl. Mater. Interfaces*, **2018**, 10, 29511.
- [45] J. Yun, J. Jun, J. Lee, J. Ryu, K. Lee, H. Yu, J. Jang, *RSC Adv.*, **2017**, 7, 20694.
- [46] R. Liu, S. M. Mahurin, C. Li, R. R. Unocic, J. C. Idrobo, H. Gao, S. J. Pennycook, S. Dai, *Angew. Chem. Int. Ed.*, **2011**, 50, 6799.

- [47] M. Kim, C. Lee, J. Jang, *Adv. Funct. Mater.*, **2014**, 24, 2489.
- [48] H. -G. Wang, S. Yuan, D. -L. Ma, X. -B. Zhang, J. -M. Yan, *Energy Environ. Sci.*, **2015**, 8, 1660.
- [49] Y. Zhang, B. Lin, J. Wang, J. Tian, Y. Sun, X. Zhang, H. Yang, *J. Mater. Chem. A*, **2016**, 4, 10282.
- [50] W. Na, J. Jun, J. W. Park, G. Lee, J. Jang, *J. Mater. Chem. A*, **2017**, 5, 17379.
- [51] C. -L. Zhang, S. -H. Yu, *Chem. Soc. Rev.*, **2014**, 43, 4423.
- [52] J. T. McCann, M. Marquez, Y. Xia, *J. Am. Chem. Soc.*, **2006**, 128, 1436.
- [53] W. -T. Koo, S. -J. Choi, S. -J. Kim, J. -S. Jang, H. L. Tuller, I. -D. Kim, *J. Am. Chem. Soc.*, **2016**, 138, 13431.
- [54] L. Li, S. Peng, J. K. Y. Lee, D. Ji, M. Srinivasan, S. Ramakrishna, *Nano Energy*, **2017**, 39, 111.
- [55] D. Li, Y. Xia, *Adv. Mater.*, **2004**, 16, 1151.
- [56] N. Jung, S. Kwon, D. Lee, D. -M. Yoon, Y. M. Park, A. Benayad, J. -Y. Choi, J. S. Park, *Adv. Mater.*, **2013**, 25, 6854.
- [57] W. Zuo, R. Li, C. Zhou, Y. Li, J. Xia, J. Liu, *Adv. Sci.*, **2017**, 4, 1600539.
- [58] G. Nagaraju, S. M. Cha, S. C. Sekhar, J. S. Yu, *Adv. Energy Mater.*, **2017**, 7, 1601362.
- [59] L. Zhang, K. N. Hui, K. San Hui, H. Lee, *J. Power Sources*, **2016**, 318, 76.
- [60] C. -T. Hsu, C. -C. Hu, *J. Power Sources*, **2013**, 242, 662.
- [61] D. Ghosh, M. Mandal, C. K. Das, *Langmuir*, **2015**, 31, 7835.
- [62] C. Yuan, L. Zhang, L. Hou, G. Pang, W. -C. Oh, *RSC Adv.*, **2014**, 4, 14408.
- [63] H. S. Choi, C. R. Park, *J. Power Sources*, **2014**, 259, 1.
- [64] O. M. Yaghi, H. Li, *J. Am. Chem. Soc.*, **1995**, 117, 10401.
- [65] O. M. Yaghi, G. Li, H. Li, *Nature*, **1995**, 378, 703.

- [66] S. Carrasco, *Biosensors*, **2018**, 8, 92.
- [67] Z. Xie, W. Xu, X. Cui, Y. Wang, *ChemSusChem*, **2017**, 10, 1645.
- [68] Y. Chen, X. Huang, S. Zhang, S. Li, S. Cao, X. Pei, J. Zhou, X. Feng, B. Wang, *J. Am. Chem. Soc.*, **2016**, 138, 10810.
- [69] Y. Chen, S. Zhang, S. Cao, S. Li, F. Chen, S. Yuan, C. Xu, J. Zhou, X. Feng, X. Ma, B. Wang, *Adv. Mater.*, **2017**, 29, 1606221.
- [70] B. Li, H. -M. Wen, Y. Cui, W. Zhou, G. Qian, B. Chen, *Adv. Mater.*, **2016**, 28, 8819.
- [71] S. Chaemchuen, N. A. Kabir, K. Zhou, F. Verpoort, *Chem. Soc. Rev.*, **2013**, 42, 9304.
- [72] N. Stock, S. Biswas, *Chem. Rev.*, **2012**, 112, 933.
- [73] H. Hu, B. Guan, B. Xia, X. W. Lou, *J. Am. Chem. Soc.*, **2015**, 137, 5590.
- [74] S. J. Yang, S. Nam, T. Kim, J. H. Im, H. Jung, J. H. Kang, S. Wi, B. Park, C. R. Park, *J. Am. Chem. Soc.*, **2013**, 135, 7394.
- [75] W. Zhang, X. Jiang, X. Wang, Y. V. Kaneti, Y. Chen, J. Liu, J. - S. Jiang, Y. Yamauchi, M. Hu, *Angew. Chem. Int. Ed.*, **2017**, 56, 8435.
- [76] D. Liu, J. Wan, G. Pang, Z. Tang, *Adv. Mater.*, **2018**, 0, 1803291.
- [77] H. Li, J. Lang, S. Lei, J. Chen, K. Wang, L. Liu, T. Zhang, W. Liu, X. Yan, *Adv. Funct. Mater.*, **2018**, 28, 1800757.
- [78] B. Y. Guan, X. Y. Yu, H. B. Wu, X. W. Lou, *Adv. Mater.*, **2017**, 29, 1703614.
- [79] B. Liu, H. Shioyama, H. Jiang, X. Zhang, Q. Xu, *Carbon*, **2010**, 48, 456.
- [80] N. L. Torad, R. R. Salunkhe, Y. Li, H. Hamoudi, M. Imura, Y. Sakka, C. -C. Hu, Y. Yamauchi, *Chem. Eur. J.*, **2014**, 20, 7895.
- [81] R. R. Salunkhe, J. Tang, Y. Kamachi, T. Nakato, J. H. Kim, Y. Yamauchi, *ACS Nano*, **2015**, 9, 6288.
- [82] Y. Li, Y. Xu, W. Yang, W. Shen, H. Xue, H. Pang, *Small*, **2018**, 14, 1704435.

- [83] J. Shao, Z. Wan, H. Liu, H. Zheng, T. Gao, M. Shen, Q. Qu, H. Zheng, *J. Mater. Chem. A*, **2014**, 2, 12194.
- [84] F. Meng, Z. Fang, Z. Li, W. Xu, M. Wang, Y. Liu, J. Zhang, W. Wang, D. Zhao, X. Guo, *J. Mater. Chem. A*, **2013**, 1, 7235.
- [85] G. Yilmaz, K. M. Yam, C. Zhang, H. J. Fan, G. W. Ho, *Adv. Mater.*, **2017**, 29, 1606814.
- [86] Y. Zhang, H. Chen, C. Guan, Y. Wu, C. Yang, Z. Shen, Q. Zou, *ACS Appl. Mater. Interfaces*, **2018**, 10, 18440.
- [87] Z. Jiang, Z. Li, Z. Qin, H. Sun, X. Jiao, D. Chen, *Nanoscale*, **2013**, 5, 11770.
- [88] P. Wang, Y. Li, S. Li, X. Liao, S. Sun, *J. Mater. Sci. Mater. Electron.*, **2017**, 28, 9221.
- [89] L. -F. Chen, Y. Lu, L. Yu, X. W. Lou, *Energy Environ. Sci.*, **2017**, 10, 1777.
- [90] C. Wang, C. Liu, J. Li, X. Sun, J. Shen, W. Han, L. Wang, *Chem. Commun.*, **2017**, 53, 1751.
- [91] C. Guan, X. Liu, W. Ren, X. Li, C. Cheng, J. Wang, *Adv. Energy Mater.*, **2017**, 7, 1602391.
- [92] G. Lee, Y. D. Seo, J. Jang, *Chem. Commun.*, **2017**, 53, 11441.
- [93] S. -K. Park, S. H. Yang, Y. C. Kang, *Chem. Eng. J.*, **2018**, 349, 214.
- [94] Z. Lv, Q. Zhong, Y. Bu, *Adv. Mater. Interfaces*, **2018**, 5, 1800438.
- [95] B. Chen, Z. Yang, Y. Zhu, Y. Xia, *J. Mater. Chem. A*, **2014**, 2, 16811.
- [96] D. Matatagui, A. Sainz-Vidal, I. Gràcia, E. Figueras, C. Cané, J. M. Saniger, *Sens. Actuators B Chem.*, **2018**, 274, 601.
- [97] Y. Pan, Y. Liu, G. Zeng, L. Zhao, Z. Lai, *Chem. Commun.*, **2011**, 47, 2071.
- [98] J. Qian, F. Sun, L. Qin, *Mater. Lett.*, **2012**, 82, 220.

- [99] H. Pang, X. Li, Q. Zhao, H. Xue, W. -Y. Lai, Z. Hu, W. Huang, *Nano Energy*, **2017**, 35, 138.
- [100] H. Zhang, J. Wu, L. Zhou, D. Zhang, L. Qi, *Langmuir*, **2007**, 23, 1107.
- [101] R. -O. Moussodia, L. Balan, C. Merlin, C. Mustin, R. Schneider, *J. Mater. Chem.*, **2010**, 20, 1147.
- [102] J. S. Suroshe, S. S. Garje, *J. Mater. Chem. A*, **2015**, 3, 15650.
- [103] X. W. Lou, D. Deng, J. Y. Lee, J. Feng, L. A. Archer, *Adv. Mater.*, **2008**, 20, 258.
- [104] Y. Li, B. Tan, Y. Wu, *J. Am. Chem. Soc.*, **2006**, 128, 14258.
- [105] D. Ghosh, S. Giri, C. K. Das, *Environ. Prog. Sustain. Energy*, **2014**, 33, 1059.
- [106] Z. Liu, R. Ma, M. Osada, K. Takada, T. Sasaki, *J. Am. Chem. Soc.*, **2005**, 127, 13869.
- [107] C. Mondal, M. Ganguly, P. K. Manna, S. M. Yusuf, T. Pal, *Langmuir*, **2013**, 29, 9179.
- [108] G. X. Pan, X. Xia, F. Cao, P. S. Tang, H. F. Chen, *Electrochim. Acta*, **2012**, 63, 335.
- [109] M. C. Biesinger, B. P. Payne, A. P. Grosvenor, L. W. M. Lau, A. R. Gerson, R. S. C. Smart, *Appl. Surf. Sci.*, **2011**, 257, 2717.
- [110] S. Xie, Y. Liu, J. Deng, J. Yang, X. Zhao, Z. Han, K. Zhang, H. Dai, *J. Catal.*, **2017**, 352, 282.
- [111] J. -M. Syu, M. -L. Hsiao, C. -T. Lo, *J. Phys. Chem. C*, **2017**, 121, 23287.
- [112] Y. Liu, N. Fu, G. Zhang, M. Xu, W. Lu, L. Zhou, H. Huang, *Adv. Funct. Mater.*, **2017**, 27, 1605307.
- [113] T. Li, G. H. Li, L. H. Li, L. Liu, Y. Xu, H. Y. Ding, T. Zhang, *ACS Appl. Mater. Interfaces*, **2016**, 8, 2562.
- [114] J. Xu, F. He, S. Gai, S. Zhang, L. Li, P. Yang, *Nanoscale*, **2014**, 6, 10887.

국문초록

슈퍼커패시터는 연료 전지 및 배터리와 함께 현대 산업에서 가장 각광 받는 에너지 장치 중 하나이다. 높은 출력 밀도 및 긴 수명을 가지는 특성으로 인해, 슈퍼커패시터는 에너지의 빠른 저장 및 회수가 필요한 많은 분야에서 활용되어 왔다. 하지만, 다른 에너지 장치들에 비해 상대적으로 낮은 에너지 밀도는 슈퍼커패시터의 다양한 산업 분야에서의 포괄적인 사용을 제한하였다. 따라서, 슈퍼커패시터의 유리한 특성은 그대로 유지하면서 에너지 밀도를 향상시키기 위해, 최근 슈퍼커패시터에 대한 연구 동향은 전하 저장 능력, 속도 성능, 그리고 주기 안정성 면에서 모두 우수한 새로운 전극 물질을 개발하는 데에 초점이 맞추어져 왔다. 위 목적을 달성하기 위해서는, 각 유형의 슈퍼커패시터 전극 재료 (즉, 전기 이중층 커패시터, 슈도커패시터, 그리고 배터리 유형의 재료)의 장단점을 고려하여, 적용되는 재료가 적절하게 선택되고 조합되어야 한다. 이러한 전극 재료의 본질적인 특성 외에도, 전극 재료와 주변 전해질 간의 상호 작용을 촉진하기 위한 구조의 합리적인 설계는 고성능 슈퍼커패시터

전극 재료를 얻기 위해 고려되어야 하는 또 하나의 중요한 요소이다.

금속-유기 골격체의 일종인 제올라이트형 이미다졸레이트 골격체는 특정 금속 이온과 이미다졸레이트 리간드의 배열에 의해 만들어진 넓은 표면적을 가진 결정질 다공성 물질이다. 흥미롭게도, 최근 고성능 슈퍼커패시터 전극 재료를 합성하기 위한 전구 물질로써 제올라이트형 이미다졸레이트 골격체를 사용하는 시도가 증가하고 있다. 적절한 열 처리나 화학 반응을 가해줌으로써, 제올라이트형 이미다졸레이트 골격체는 탄소, 금속 산화물, 금속 수산화물을 비롯한 다양한 전기 활성 물질로 변환될 수 있다. 게다가, 제올라이트형 이미다졸레이트 골격체를 전구 물질로 사용함으로써 다공성/중공 구조 등의 독특한 구조를 가지는 전기 활성 물질을 쉽게 얻을 수 있다. 따라서, 제올라이트형 이미다졸레이트 골격 유도체의 구조 및 화학 조성에서의 다양성은 차세대 슈퍼커패시터 전극 재료 설계에 유용하게 이용될 수 있다.

본 논문에서는 다양한 제올라이트형 이미다졸레이트 골격 유도체/탄소 구조체의 제조 방법과 이들의 슈퍼커패시터 전극 재료에 대한 응용에 대하여 제시한다. 제올라이트형 이미다졸레이트 골격 유도체 및 탄소 구조체를 사용하여 전하

저장에 유리한 구조를 설계하기 위한 효과적인 방법들이 논의되었다. 첫 번째로, 다공성 탄소, 산화 아연 양자점, 그리고 탄소 나노 섬유로 구성된 하이브리드 구조가 전기 방사 된 제올라이트형 이미다졸레이트 골격체-8/폴리비닐알코올 나노 섬유의 탄화를 통해 제조되었다. 이 구조체는 주축 상에 1차원의 전도성 경로와 표면 상에 다공성 구조 및 슈도커패시터형 산화 아연 양자점을 가졌다. 두 번째로, 수산화 코발트 상에 균일하게 분포 된 산화 코발트 나노 입자의 하이브리드 구조가 제올라이트형 이미다졸레이트 골격체-67의 수열 반응에 의해 제조되었다. 이 구조에서, 수산화 코발트는 다수의 산화 코발트 나노 입자의 지지체로 작용하여 활성 물질 사이의 응집을 완화시켰다. 마지막으로, 제올라이트형 이미다졸레이트 골격체-67과 중공 탄소 구체의 복합체가 중공 니켈-코발트 층상 이중수산화물과 중공 탄소 구체의 하이브리드 구조를 합성하기 위한 전구 물질로 활용되었다. 이 구조체는 독특한 중공-내-중공 구조를 가졌다. 위에서 제조된 제올라이트형 이미다졸레이트 골격체/탄소 구조체들은 합리적으로 설계된 구조 덕분에 높은 전기 화학적 성능을 나타내었다. 따라서, 본 논문은 고성능 슈퍼커패시터 전극 물질의 제조, 특히 구조 설계에 대한 접근법을 제시한다.

주요어: 슈퍼커패시터, 금속-유기 골격체, 제올라이트형
이미다졸레이트 골격체, 탄소 물질, 하이브리드 구조

학 번: 2014-22597